Electric Preheating of Combustion Air

B. M. van Veen

Msc. Thesis

Design of a cost-effective and compact electric combustion air preheater for the LSV® burner.

by

B. M. van Veen

In fulfillments of the requirements for the degree of

Master of Science

in Mechanical Engineering
at the Delft University of Technology

To be publicly defended on July the 9th, 2021.

Student number:	4344804	
Supervisors:	Prof. Dr. Dirk Roekaerts	Delft University of Technology
	Ir. Iek Risseeuw	Technip Benelux B.V.
Thesis Committee:	Dr. ir. Mark Tummers	Delft University of Technology
	Dr. Dominico Lahaye	Delft University of Technology

P&E report number 3043

An electronic version of this thesis is available at http://repository.tudelft.nl/.

Abstract

This thesis report discusses the design of a cost-effective and compact electric combustion air preheating for the LSV® burner. The industry has a complex problem to solve and an important role to play during the energy transition, that is needed because of global warming. Many industrial processes use heat generated by the combustion of fossil fuels. An alternative sustainable solution needs to be chosen in the future. Fossil fuels can be replaced by biofuels, hydrogen, electric power or a hybrid solution.

For this study a solution using electric power is investigated, which could also be used in a hybrid solution. Electric combustion air preheating can be used to shift the energy input from fuel energy to electrical energy. This is new since normally combustion air preheating is accomplished in the convective part of the fired heater. A system to heat up the combustion air to a temperature of 300°C is designed using correlations for tube banks and CFD modelling. An experiment is also conducted to investigate the impact of the combustion air preheater on the burner and fired heater performance. It is important that the burner and fired heater performance remain almost unchanged since the whole fired heater is designed around specific performance parameters.

The design includes a staggered and finned tube bank that can reduce CO_2 emissions with 3.2 % by using green electricity when operating 3000 hours per year. This method for combustion air preheating will also result in an operating cost reduction and a payback time of less than five years. A drawback of this system is that the NO_x emissions will increase by a factor of 2, which is bad for the environment since it is responsible for the formation of smog and the general acidification of soil and water. This could be avoided by improving the burner design or applying other combustion control mechanisms.

The outcome shows that electric combustion air preheater is suitable technology for CO_2 emissions reduction in the short term for fired heaters. With the increasing CO_2 emissions cost and increasing volatility of the electricity market, this is an attractive grid balancing equipment.

Acknowledgement

Hereby I would like to express my sincere gratitude to all who have been contributing to this study. Without the help of everyone I would not have been able to deliver this thesis in the form as it is.

Firstly, I would like to thank my supervisor Iek Risseeuw from Technip Energies and Dirk Roekaerts from the Delft University of Technology. Their expertise and constructive criticism helped me a lot, while learning about fired heaters, heat exchangers and CFD modelling. Secondly also thanks to other colleagues from Technip Energies, for helping with the experiments, CFD modelling and feedback during the presentations.

Furthermore I would like to thank my friends, family, and colleague students, whom I could reach out to when having difficulties and for the distraction from the reading and studying the past few months. Lastly also a big thankyou to Randi for her understanding and endless support during the past eight months.

Table of Contents

Symbols

Convective heat transfer

A	Heat transfer area
A/A_{t0}	ratio finned surface to surface of base tube
A_m	Minimum crossflow area
C_D	Drag coefficient
D	Diameter
d_f	Fin tip diameter
d_o	Reference length
d_r	Fin root diameter
f_s	Fin spacing
h_c	Heat transfer coefficient
h_f	Fin height
K	Thermal conductivity
L	Characteristic length
$\dot{m}$	Mass flow rate
Nu	Nusselt number
Pr	Prandtl number
q	Heat transfer rate
Re	Reynolds number
R_x	Tube pitch ratio in transverse direction
R_y	Tube pitch ratio in longitudinal direction
s	Fin pitch
S_x	Tube pitch in transverse direction
S_y	Tube pitch in longitudinal direction
T_b	Bulk temperature
T_{in}	Inlet temperature air
T_m	Mean temperature
T_{out}	Outlet temperature air
T_s	Surface temperature
V	Velocity
w_0	Mean velocity
δ	Fin width
η_b	Dynamic bulk viscosity
θ	Angle
ν	Kinematic viscosity

Pressure drop

D	Diameter
C	Loss coefficient (HTFS)
L	Tube bank length
f	Correction factor (different for each method)
$\dot{M}_c$	Mass flow rate
N_R	Number of rows
ΔP	Pressure drop
S_m	Smallest cross-sectional area
w_{max}	Maximum velocity
ξ	Drag coefficient
ρ_b	Bulk density

Radiative heat transfer

A	Radiative heat transfer area
E_b	Blackbody emissive power
F	Shape factor
G	Irradiation
J	Radiosity
$\dot{Q}$	Heat transfer rate
T	Absolute temperature
α	Absorptance
ε	Emissivity
ρ	Reflectance
σ	Stefan-Boltzmann constant

CFD Modelling

e	Internal energy
f_μ	Turbulent viscosity factor
g_i	Gravitational acceleration in direction x_i
h	Thermal enthalpy
h_m^0	Individual thermal enthalpy of the m-th mixture component
k	Turbulent kinetic energy
P, p	Pressure
P_c	Critical pressure
Q_H	Heat source or sink per unit volume
q_i	Diffusive heat flux
r	The distance from a point to rotation axis in reference frame
S_i	Mass-distributed external force per unit due to a porous media, buoyancy and/or coordinate system's rotation.
T_c	Critical temperature
u	Fluid velocity
V_c	Critical specific volume
y	Distance to wall
y_m	Concentration of the m-th mixture component
δ_{ij}	Kronecker delta function
ε	Turbulent dissipation
μ	Dynamic viscosity coefficient
μ_t	Turbulent eddy viscosity coefficient
ρ	Fluid density
τ_{ij}	Viscous shear stress tensor
τ_{ij}^k	Reynolds stress tensor
Ω	Angular velocity of the rotating coordinate system

Abbreviations

AFT	Adiabatic Flame Temperature
CAPEX	Capital Expenditures
CFD	Computational Fluid Dynamics
ECAP(S)	Electric Combustion Air Preheater / Preheating System
EU-ETS	European Union Emissions Trading System
FV	Finite Volume method
GHG	Green House Gas
GWP	Global Warming Potential
HHV	Higher Heating Value
lam	Laminar
LCA	Life Cycle Assessment
LHV	Lower Heating Value
LN	Low NO_x modus
LSV	Large Scale Vortex
MILD	Moderate or Intense Low-oxygen Dilution combustion
NG	Natural Gas
NMVOC	Non-Methane Volatile Organic Compounds
OPEX	Operational Expenditures
PG	Petroleum Gas
ppmv	Parts per million volume
rdg	read value or displayed value
SU	Start-Up modus
turb	Turbulent
vol%	Volume percentage
WC	Water Column (pressure)

Species

CO	Carbon Monoxide
CO_2	Carbon Dioxide
NO_x	Nitrogen Oxides
T-NO_x	Thermal NO_x
P-NO_x	Prompt NO_x
F-NO_x	Fuel NO_x
NO	Nitrogen Oxide
NO_2	Nitrogen Dioxide
N_2O	Nitrous Oxide
O_2	Oxygen
SO_2	Sulphur Dioxide

Figures

Tables

1
Introduction

Since the beginning of the petrochemical industry, fired heaters have been widely used to provide the required process energy and are accountable for a significant part of the energy demand of the petrochemical industry. Fired heaters provide the required energy by fuel combustion, and reducing their fuel consumption and CO_2 emissions is one of the biggest challenges for the industry in the energy transition. Switching to renewable electricity for some high temperature processes is part of the solution. Eventually, the fossil resources will be phased out as a resource for high temperature processes and shall most likely be replaced by biofuels, hydrogen and electric power. But this cannot be accomplished overnight, so innovative technologies are needed to guide the fired heaters through this transition.

Fuel consumption and CO_2 emissions can be reduced by using renewable electricity for combustion air preheating within the fired heaters. The concept of combustion air preheating has already been applied for a long time, and is generally realized by preheating of the combustion air in the convective part of the fired heater. In the Netherlands, approximately half of the fired heaters use this type of combustion air preheating and that number is somewhat less for the fired heaters worldwide.

Combustion air preheating using grid power, instead of using the heat from the flue gases, is new. On top of the CO_2 emissions reduction accomplished over the conventional method this could also allow other processes to use the heat from the flue gases in the convective part. This new electric combustion air preheat system could also be easily switched on and off and be used as electricity grid balancing equipment.

During this study, the impact of using combustion air preheating with electrical power on the heat flux profile and emissions of the burner and fired heater will be analysed. Based on the LSV® burner from Technip Energies, a cost-effective and compact electric combustion air preheater (ECAP) will be designed.

1.1. Research questions

The purpose of this study is to design a cost-effective and compact electric combustion air preheater (ECAP) for the LSV® burner from Technip Energies. Further, the impact on the burner and fired heater performance is analysed.

Main questions and sub-questions:

What is the design of a cost-effective and compact ECAP for the LSV® burner from Technip Energies?

- What's the most suitable method to heat combustion air using electric power?
- What is the operating temperature range of such a system? And to what temperature can the combustion air be heated?
- What is the extra pressure drop of such a system?

How will the ECAP influence the LSV® burner and fired heater performance?

- What is the effect on heat flux distribution within the fired heater?
- What is the effect on the CO_2 and NO_x emissions?
- How much fuel and costs can be saved?

1.2. Research approach and planning

An answer to the above research questions defined above will be explored by the following subprojects:

- Design of the ECAP using correlations and detailed CFD modelling.
- Burner testing at the test facility for different combustion air preheating temperatures.

This study starts with a literature study, followed by designing the ECAP using several heat transfer correlations. The heat transfer is also calculated by CFD simulations. Based on the literature and the CFD check a suitable heat transfer correlation is selected for the design of the ECAP. The influence of this system on the burner and fired heater heat flux profile and emissions is analysed using experimental results. In the end, conclusions are drawn with recommendations for further research. This is illustrated in the timeline given in Figure 1.2.1.

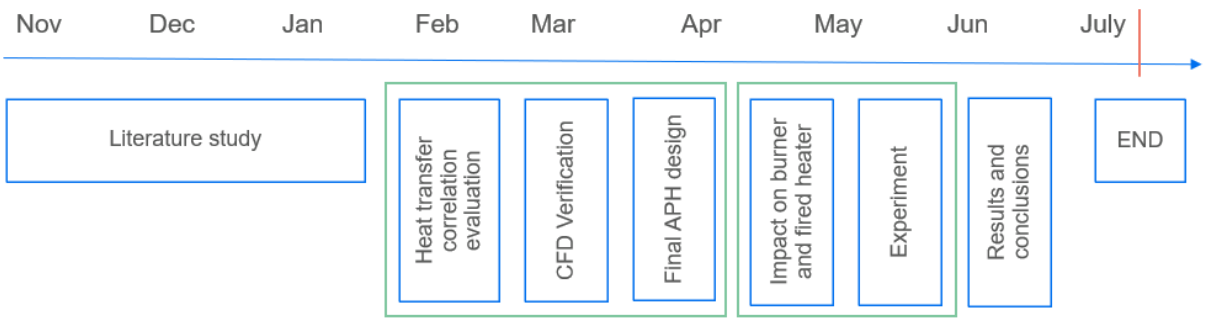

Figure 1.2.1 – Timeline of the thesis.

2
Literature review

2.1. Energy transition

The extensive usage of fossil fuel-based energy has led to a rapid increase of greenhouse gas (GHG) concentrations in the atmosphere, resulting in global warming and the climate change that we are facing now. The GHG effect is defined as the warming up of the earth due to the re-radiation of energy by the GHG in the atmosphere. Examples of greenhouse gasses are CO_2, CH_4 and NO_x, but there are many more.

The world faces a huge challenge since there is an increasing demand for energy, but at the same time the GHG emissions need to be reduced. In 2016 a landmark was set in the multilateral climate change process by the Paris Agreement. The Paris Agreement sets out a global framework to avoid dangerous climate change by limiting global warming to below 2°C and pursuing efforts to limit it to 1.5°C. It also aims at strengthening countries' ability to deal with the impact of climate change and support them in their efforts [1].

The energy transition is one of the most important actions to avoid climate change. With the energy transition, the world wants to change the way we produce and use energy so that GHG emissions can be reduced and eventually prevented. Multiple countries have set up and published their own climate plans conform The Paris Agreement like The Netherlands [2] and also multiple key players in the energy industry, for instance, Royal Dutch Shell (Shell) [3] and British Petroleum (BP) [4], have published their roadmap towards a net-zero carbon emission. Most of the countries and companies aim to reduce their carbon emission with 30-60% by 2030 and to have net-zero carbon emission by 2050. In 2021 the District court in The Hague ruled that by 2030 Shell must reduce its net carbon emissions by 45% compared to its 2019 level [5]. Not only for its business in The Netherlands, but for its business worldwide. That was the first time in history that an energy company was ordered by the court to reduce their carbon emissions, but more cases are likely to follow.

The energy resource profile is changing from fossil-based energy to more sustainable energy and renewable energy resources to reduce GHG emissions and address the climate challenges. Unfortunately, there is no singly storyline about the future, and the policy responses about the energy transition opened up a wide range of possible energy futures. By considering different assumptions about key unknowns, multiple scenarios can be made.

The report from the International Energy Agency (IEA) [6] describes multiple scenarios and is discussed below. The scenario that will help the world to reach the targets of The Paris Agreement is presented in this report, namely the "Sustainable Development Scenario (SDS)". These expected trends from the IEA are also the expectation of multiple other agencies like IRENA [7], DNV-GL [8], and Bloomberg [9]. There is only a quantitative difference between the scenarios discussed in the reports. The Netherlands has on a national scale the same vision and ambition [10].

According to the IEA will the energy sector in advanced economies and developing economies must transform significantly towards renewable energy sources from 2019 to 2030. The share of fossil-based energy in the primary energy mix will decrease from 80% to 70%, and the share of electricity in the final energy consumption will rise from 19% to 24% over the 2019-2030 period. The demand for electricity will mostly increase due to processes shifting from fossil fuel energy to electric energy. It is also expected that renewables will grow from 25% to more than 50% in global electricity generation over the 2019-2030 period. So, electricity will have an increasing share of the energy mix due to the shift to renewable energies like solar PV and wind and the phasing out of fossil resources.

The increase of capacity of fluctuating electricity resources (wind, solar) and the decrease of the scalable electricity load resources (coal, gas) has a big impact on the size of the installed electricity grid. Grid balancing has become an important aspect of the electricity grid because it helps with matching the supply to the demand for electricity. But with less scalable and more fluctuating electricity resources, it will be more difficult to balance the grid load. On top of that, will it be difficult for most of the TSO's to scale up parallel to the increase of installed capacity since these projects have a timeframe of 3-10 years at least. As a result of this, a more volatile electricity price is expected with a higher average electricity price [11], [12], [13]. The average electricity price per yearly operating hours in The Netherlands is given in Figure 2.1.2 from [14]. According to this figure could a lower average electricity price be expected in the future, when operating only a part of the year [15]. For example, the average electricity price was in 2020 32 euro/MWh, but when only operating during the cheapest 4000 hours, the average electricity price became 20 euro/MWh. The price for operating 3000 hours per year is kept constant for this thesis at 20 euro/MWh for the coming decade, which is a more conservative number.

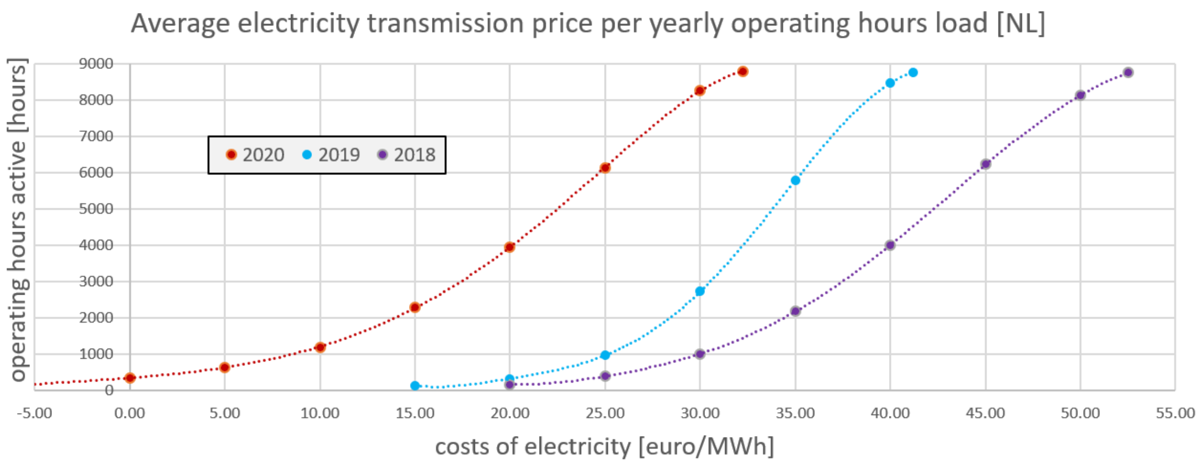

Figure 2.1.2 - Average electricity price per yearly operating hours in The Netherlands.

The natural gas prices are kept constant in this thesis, since this is difficult to predict and argue what these prices will do in the coming decade. It has also remained fairly the same over the last decades, with some fluctuations due to the financial market and the production in the petrochemical industry [16].

Another factor to keep in mind is the carbon emission taxes. In Figure 2.1.3 the development of the price for the emission of one ton CO_2 is given from [17]. These emissions taxes are introduced in 2005 in the European Union. The Cap of the CO_2 emissions reduces over time so that the total emissions will fall. Within the cap, companies can buy emission allowances, which they can trade with one another. Technip Energies expect an increase to at least 125-150 euro within the coming decade [18]. A forecast has also been made by PwC from the Dutch national CO_2 emissions tax and the EU-ETS price projections from PBL [19], see Figure 2.1.4. One should note that the EU intends to increase their CO_2 emissions reduction ambitions, what will result in a higher carbon market price development. The Technip expectation curve takes this into account, see Figure 2.1.4.

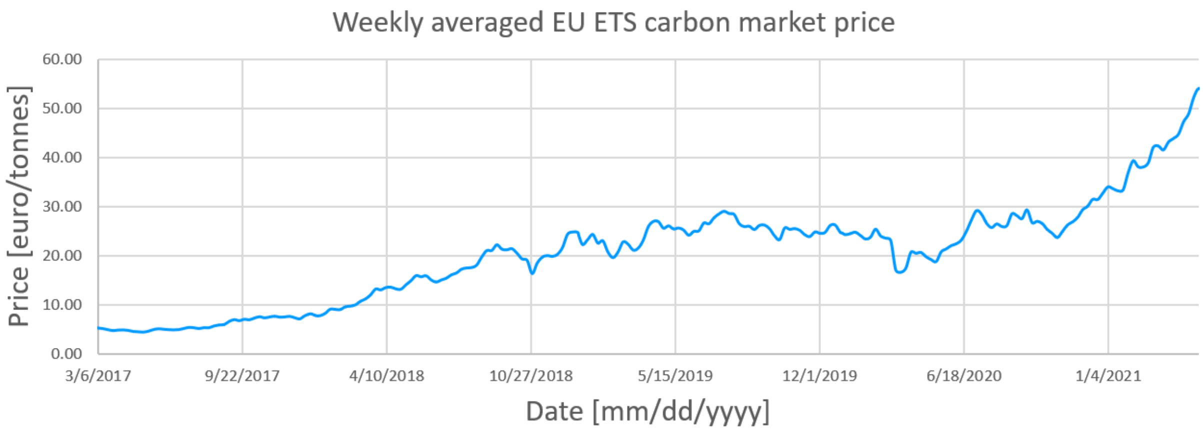

Figure 2.1.3 - Weekly averaged EU ETS carbon market price [euro/tonnes CO_2].

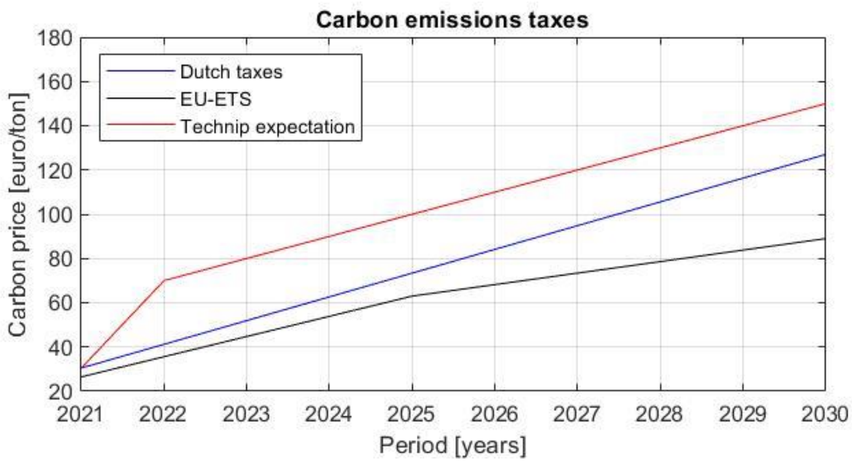

Figure 2.1.4 – Expected price development for the carbon emissions in the Netherlands (Dutch taxes and Technip expectation) and the EU (EU-ETS) in [euro/ton CO_2].

2.2. Fired heaters

For this master thesis, we limit ourselves to the continuous oil refining and petrochemical fired heaters. The monograph of P. Mullinger and B. Jenkins [20] is used to describe the working principle of the fired heaters, burners and the emissions from burning fossil fuels. These fired heaters achieve the required temperature in the product, often a hydrocarbon, either by steam or direct heating. In the latter case, the fluid is contained in tubes under pressure which are heated from the outside by direct composure to the flames. The heat is transferred by radiation and convection and needs to be carefully controlled, otherwise output is lost or hot spots are created. These hot spots can lead to carbon formation on the inside of the tubes, also known as coking. This will eventually lead to dangerous situations and can lead to the failing of the heater and in worst cases to destruction of the plant.

Fired heaters consist of the radiative area, the convective area, the process fluid tubes, the stack and the fuel/air supply (Figure 2.2.6). In this master thesis, we limit ourselves to the burner and the design of the combustion air supply system. The combustion air supply system is an important part of the fired heater since the air flow has a significant effect on the fuel-air mixing and the combustion process. The combustion air supply can be divided in four types, namely [20]:

- Natural draught
- Induced draught
- Forced draught
- Balanced draught

Natural draught utilizes the buoyancy of the hot flue gas in the fired heater and stack to provide air flow through the fired heater. No fans are needed, but the suction is small, typically 100-500 Pa. Relative high flue gas temperatures are needed to create the draught, so heat exchangers could not be used to recover all surplus heat from the flue gases.

Induced draught uses a fan in the flue gas system to increase the suction, typically installed in the stack. These fans should be able to deal with the hot flue gases making the material more expensive. Forced draught uses a fan in front of the burner to blow air through the burner and fired heater. High pressures can be achieved with high flue gas velocities, increasing the convective heat transfer and reducing the equipment size. A balanced draught system combines both types of draught to get the best of both worlds. This system requires an advanced control system to maintain stable operation.

Traditional fired heaters were very inefficient, using natural draft with high excess combustion air, high flue gas temperatures and no heat recovery. They often had an energy efficiency of less than 50%. Modern fired heaters utilize convective preheating of the liquid and heat recovery of the flue gas to preheat the combustion air. They also utilize a balanced draught system to control the excess air. They now achieve much higher energy efficiencies. A schematic overview of a modern fired heater is given in Figure 2.2.6 with its efficiency illustrated in the energy flow diagram in Figure 2.2.5.

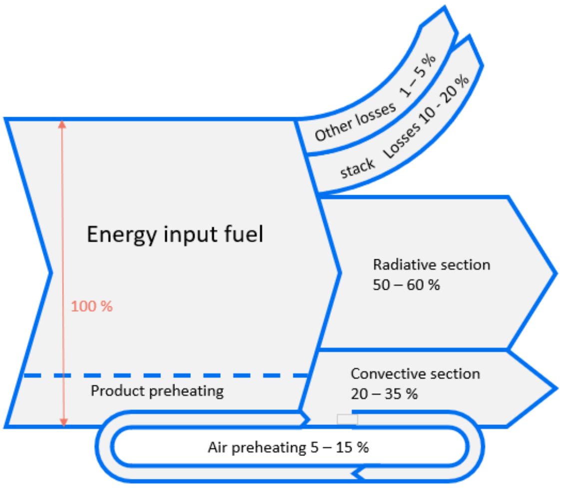

Figure 2.2.5 - Sankey diagram of the energy flow in a state-of-the-art fired heater based on XX. The sum of the radiative and convective section is the useful energy.

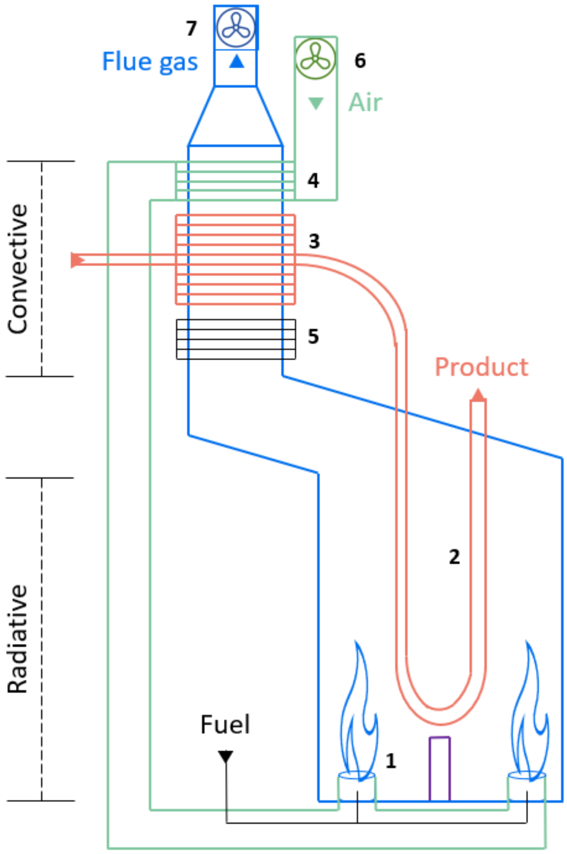

Figure 2.2.6 - Schematic overview of a state-of-the-art fired heater. With (1) burners (2) radiative product heating (3) convective product preheating (4) convective combustion air preheating (5) other products heating (6) forced draught fan (7) induced draught fan.

The thermal efficiency of fired heaters is defined as the useful energy derived from the fired heater relative to the energy input. Since fired heaters involve combustion, the primary energy input is ultimately derived from the fuel, but it can also include the energy required to preheat the combustion air, if applied. The useful energy may also include waste heat recovery by other products or fluid flows in addition to the primary product. Most fired heaters make use of heat recovery from the flue gases and/or the product to improve the thermal efficiency. These heat recovery systems usually involve heat exchangers to preheat combustion air and/or other products products. So, the efficiency of the fired heater depends on the energy transferred from the chemical fuel energy and electrical energy to the process energy contained in product streams. The total efficiency depends on the efficiency of each operation in the process, so for the total efficiency, we should also include the energy needed to drive the air fans and fired heater drive motors.

The primary driving force for making fired heaters much more efficient is the overall cost of operation so that a product can be sold at a competitive price. These costs are based on capital costs, fuel and electricity costs, maintenance costs and environmental costs and charges. The latter was not that relevant in the 19th century, but because of climate change and its relationship with carbon dioxide concentrations, it has an increasing impact on the costs and efficiency development.

2.3. Burners

Burners are transducers since they transform one form of energy into another form of energy. In this case, chemical energy of the fuel into heat energy within the fired heater. The effectiveness of this process is a measure of its performance. Burners designed for fired heaters have to burn the fuel as efficiently as possible and produce the best heat flux for the product to be heated. Different processes require different heat flux profiles, so the design of a burner can be different for different applications.

When fuel and oxygen are brought together at sufficiently high temperatures a chemical reaction, i.e. combustion, takes place, resulting in heat and combustion products. The fuel can be a gas, liquid or solid, and the rate at which the combustion occurs can vary from slow decay to instantaneous explosions. When using combustion as a heat source for fired heaters, it is important to obtain a steady heat release at the required rate to suit the process.

Most of the fuels used are fossil fuels (hydrocarbons), having the elements carbon and hydrogen, and these are oxidized by the oxygen in the air to release heat during combustion. The chemistry of this oxidation process involves complex chain reactions, but for most engineering design purposes, this can be simplified to four basic reactions [20].

- The complete oxidation of carbon
- The complete oxidation of hydrogen
- The incomplete oxidation of carbon
- The incomplete oxidation of carbon monoxide

Incomplete combustion of fuels containing carbon refers to the formation of carbon monoxide or even carbon (coke). The combustion is said to be complete when the only carbon oxide present is CO_2 and no elemental carbon remains. The products of combustion which leave the fired heater are usually referred to as flue gases. To achieve complete combustion in is almost always necessary to provide excess oxygen by excess combustion air. It is the percentage of air over and above the minimum required for complete combustion, i.e. the stoichiometric air requirement.

All combustion processes take place in the following order: mixing, ignition, chemical reaction and dispersal of products. The rate of combustion depends on the slowest process, which is often the mixing. Therefore, the rate of completeness of the combustion process is controlled by the rate of fuel-air mixing. Insufficient mixing produces unburnt CO in the flue gas, wasting potential fuel energy.

The burner needs to be designed in a way that the mixing of the fuel and air streams is optimized and that enough air can be supplied to the combustion process [20]. Some burners are designed to premix the fuel and air prior to ignition, but most industrial burners are non-premixed and designed for diffusion mixing of the combustion air and fuel inside the fired heaters. For this master thesis, we limit ourselves to the burners without premixing. The amount of air required for complete combustion is in most combustion systems at least ten times that of the fuel. Meaning that air dominates the mixing process between fuel and air since it provides a greater momentum than fuel. The mixing of air and fuel influences the flame stability, emissions and the thermal release profile.

The choice of fuel is critical in the fired heater and burner design process, especially since fuel is one of the larger contributors to the costs of fired heater operation. Factor affecting the costs of the fuel are abundance or scarcity, ease of extraction or manufacturing, ease of use, political policy and ease of transportation. The relative importance of these changes with time. The properties of a fuel that influence its use are availability and cost, calorific value, flammability limits, density of fuel, chemical composition and the products of the combustion process. It is conventional to classify fuels by their physical state, i.e. gases, liquids and solids. For this master thesis, we limit ourselves to the gaseous fuels natural gas and hydrogen, although in reality the burners are also used with for example reformer gas or other standard refinery fuel gasses (petroleum gasses).

In this study only natural gas is considered as a fuel for the burner. Current developments show that burning hydrogen or mixing hydrogen with natural as a fuel for fired heaters to reduce the CO_2 emissions is also a solution that most probably will be applied in the coming decades. Therefore hydrogen fuel is discussed shortly. One of the most important parameters for any combustion system is the heat release, i.e. lower heating value (LHV) or higher heating value (HHV). The LHV is usually used in the industry, since it is representative for combustion to hot products without condensation taking place.

Fuels - Natural Gas

Natural gas contains, apart from its basis molecule methane, multiple other hydrocarbons, as well as carbon dioxide, nitrogen and some other molecules in small concentration. Typical compositions for North Sea NG, Groningen NG, and for the natural gas used during testing (called test fuel) are shown below in Table 2.3.1. Natural gas specifications are normally available from the supplier and should always be obtained prior to the development of a fired heater and burner.

Table 2.3.1 - Natural gas compositions of different sources from [21].

Property	**Canadian Gas**	**Groningen**	**Test fuel**
CH_4 (mol%)	95.2	81.6	93.1
C_2H_6 (mol%)	2.5	2.9	4.6
C_3H_8 (mol%)	0.2	0.4	0.8
Higher C_xH_y (mol%)	0.1	0.2	0.4
N_2 (mol%)	1.3	14.0	0.5
CO_2 (mol%)	0.7	0.9	0.5
Molecular weight (g/mol)	16.8	18.6	17.3
Relative density (to air)	0.58	0.68	0.598
LHV (MJ/kg)	50.6	42.2	48.7

Fuels - Hydrogen

Hydrogen could also be used as fuel and will most probably play a key role in the future for high temperature processes because it combust without carbon dioxide emissions [6]–[9]. At some plants, mostly steam methane reformers, hydrogen is already mixed in the fuel to a certain percentage. Hydrogen has a LHV of 120 MJ/kg and a much lower density than natural gas. Using hydrogen as a fuel has been explored already [22], [23], [24]. The burners operate almost the same, with a modest reduction in flame length [25]. The NO_x emissions were slightly increasing with increasing hydrogen percentage according to [22], [25]. Another paper suggests that first the NO_x emissions slightly increase, with a peak around 70% H_2. After this peak, the NO_x emissions start to decrease [26]. The latter case is with MILD flameless combustion of methane and hydrogen mixture. There is a difference between staged combustion and MILD combustion as will be further explained in [3.2 Burner NO_x formation].

Hydrogen combustion is in general characterized by high flame speed, short ignition delay time and wide flammability limits compared to natural gas [27]. The heat transferred to the product flow inside the tubes should be as uniform as possible to avoid coke formation on the inside of tubes [28]. In air-fired heaters grows the NO_x formation exponentially with the flame temperature. Adding hydrogen, which burns at higher adiabatic flame temperatures and flame speed than natural gas, would potentially increase the NO_x emissions [23], although it could also be reduced according to [24]. Preventing the increase in NO_x formation is one of the biggest challenges when using hydrogen has a fuel instead of natural gas. Another important finding from [22] was that switching from natural gas to hydrogen generally produced a decrease in convection section duty and a small increase in radiant section duty. The fuel/air ratio of the combustion of hydrogen is lower compared to natural gas resulting in a lower air flow rate, i.e. flue gas flow rate and stack velocity.

2.4. Burner emissions

The importance of the environmental impact of industrial operations increased significantly in the latter part of the twentieth century and even more now in the twenty-first century. fired heaters have a large footprint on the total emissions of the industry because most of the emissions are derived from the combustion of fuels. Most fuels consist of hydrocarbons with small quantities of sulphur, chlorine, phosphorous and nitrogen, together with traces of metals. We have discussed the complexity of the combustion of fuels, but when talking about emissions that are of interest for this master thesis, these principal pollutant compounds can be reduced to oxides of carbon and nitrogen as listed below [20].

$$C + O_2 \rightarrow CO_2$$
$$CO_2 + C \rightarrow 2CO$$
$$2C + O_2 \rightarrow 2CO$$
$$N_2 + O_2 \rightarrow 2NO$$
$$2NO + O_2 \rightarrow 2NO_2$$

High temperatures and the presence of oxygen drive most of these reactions to the right. CO_2 and NO_x has been identified as a primary cause of climate change. The oxides of nitrogen are precursors in the formation of atmospheric smog and give rise to acid rain, while CO_2 is most probably the most well-known Green House Gas (GHG) contributing to global warming.

Carbon monoxide (CO) is highly toxic and is the result of incomplete combustion. The concentration of CO present in the final flue gas is a very good indicator of the combustion performance. There is always some residual CO in the fired heater flue gases because mixing processes are not perfect, and the reaction between CO and O2 to produce CO_2 is reversible. In good combustion systems, CO formation should be limited to a few parts per million (ppm), normally in the range of 0-50 ppm. Unfortunately, CO tends often to increase when NO_x reduction techniques are applied since these reduction techniques generally achieve their objectives by delays in the mixing of fuel with air.

Nitrogen oxides (NO_x) are also formed during combustion and are designated as NO_x emissions. Initially, NO is formed and most of this is further oxidized to NO2, within the fired heater or after discharging in the flue gases into the atmosphere.

As discussed in [2.1 Energy transition] are the increasing concentrations of the molecules CO_2 and NO_x, which are increasing due to the usage of fossil fuels, responsible for global warming and the climate change that we are facing now. But they both contribute in their own way to these matters. All the different GHG trapped in the atmosphere, like CO_2, contribute with a certain factor to global warming due to re-radiation of energy. This factor is called the Global Warming Potential (GWP) and is the total heat absorbed by any other GHG in the atmosphere, as a multiple of the heat that would be absorbed by the same mass of CO_2 [29].

Although NO_x is often referred to as a GHG since it does not re-radiate energy. But it is responsible for the formation of ozone via secondary reactions with other gases, which is a greenhouse gas with a GWP of 65 [30]. It is also responsible for smog and the typical brown sky that often covers larger cities and reduces the air quality. NO_x is not only a source of atmospheric pollution but also contributes to the general acidification of soil and water since they are also the most important sources for acid rain. Sometimes Nitrous oxide (N_2O) is also included in NO_x emissions. Nitrous oxide reduces stratospheric ozone, also known as 'good' ozone and has a GWP of 300 [29]. It is sometimes produced during the combustion of biomass and coal and is the most important source of emissions in the use of artificial fertilizers.

At this moment, there is no generally accepted approach to compare NO_x emissions with CO_2 emissions, but one could do an ecological based Life Cycle Assessment (LCA), look into the regulations in an area and do a cost-based analysis. Any operation with significant emissions will be subject to either regulatory or environmental control by local, national and sometimes international agencies. The fired heaters are part of a wider industrial plant operation, and regulations are based on the total emissions of that plant. Sometimes these regulations, nationally or internationally, are even covering whole industry sectors. Within these regulations are often factors such as energy efficiency, noise, health & safety and emissions.

Some of the emissions considered may be controlled by adjusting equipment design and operation to avoid their formation, called pre-flame and in-flame control. Pre-flame controls are processes that improve the quality of the fuel and often reduce emissions by removing potential pollutants and improving the thermal efficiency. In-flame controls are focusing on optimizing the mixing and turbulence in the combustion process. These include gas recirculation, combustion staging and re-burn [31]. The theory behind the formation of NO_x during the combustion process needs to be analysed, so that the increase in NO_x emissions can be minimized while using the ECAP. This is discussed further in [3.2 Burner NO_x formation].

The EU have published a directive in 2016 on the reduction of national emissions of certain atmospheric pollutants in which a limit for these emissions is stated for the EU member states [32]. The emissions reduction commitments are based on the emissions in 2005 and set for the period of 2020-2029, and 2030 and onwards. The Netherlands have for instance their own emission reduction targets for sulphur dioxide (SO2), Nitrogen oxides (NO_x) and non-methane volatile organic compounds (NMVOC). These are given in Table 2.4.1. These emission reduction targets are likely to be realized by the Netherlands according to PBL [33], [34].

Table 2.4.1 – Emissions reduction targets for The Netherlands from the EU [32].

	SO_2		**NO_x**		**NMVOC**	
The Netherlands	**2020**	**2030**	**2020**	**2030**	**2020**	**2030**
Reduction target (%)	28	53	45	61	8	15

2.5. Combustion air preheating

Combustion air preheating can be used to increase the efficiency of the fired heaters and reduce emissions. Combustion air preheating is a specific process that is a form of heat recovery. Heat recovery equipment is generally classified by the term heat exchangers. There is a considerable variation in the design of such heat exchangers, governed by the physical and chemical properties of the hot and cold fluids. In most industrial heating devices, the sensible heat of the flue gas or outflow is circulated back in the system using heat exchangers.

There are two major groups of heat exchangers. These are recuperative and regenerative heat exchangers. Recuperative heat exchangers transfer heat continuously between the fluids, either by direct contact or through a thermally thin divided medium. Regenerative heat exchangers use a thermally absorbent sink to store the heat from the hot fluid and then release the heat to the cold fluid in a cyclic operation mode.

There are multiple heat recovery equipment to recover waste heat commercially available for different process heating systems in the industrial section. Combustion air preheating takes place in the convective part of the fired heater, as is shown in Figure 8. In this chapter, the heat recovery systems that are applicable for combustion air preheating are described [20], [35]. These are:

- Stack recuperator; Metallic radiator recuperator, Convective recuperator
- Stack Regenerator; Heat (Thermal) wheels, Brick checker work

Within the stack recuperators, heat is transferred via a metallic wall from the flue gas to the combustion air. Ducts are used to carry the fluids through the recuperator. The stack regenerator, i.e. heat wheel, is a porous disk fabricated from a high heat capacity material that is rotating between two ducts, within each duct a flowing gas (cold or hot). The sensible heat is transferred via the material thermal capacity from the hot flue gases to the cold combustion air. The stack regenerator can normally achieve higher combustion air temperatures compared to recuperative burners (not larger than 600°C) as can be seen in Figure 2.5.7 [36].

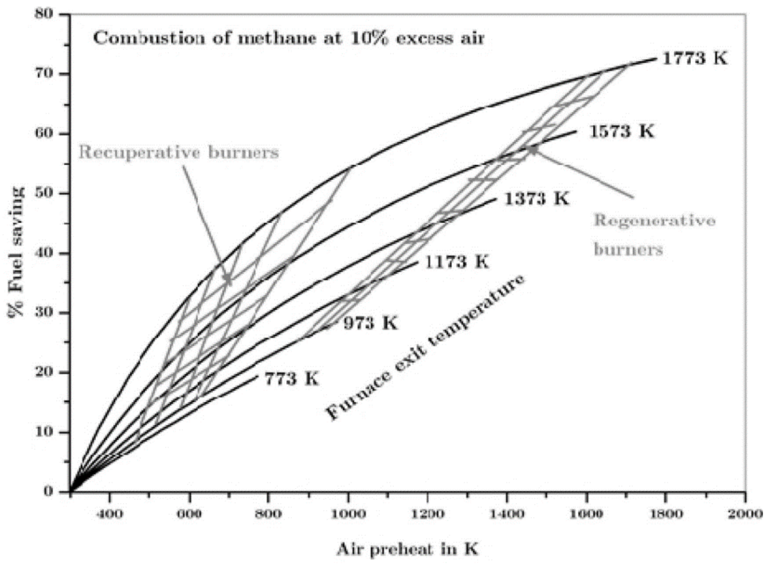

Figure 2.5.7 – The working range of recuperative and regenerative burners from [36].

With these high combustion air temperatures, NO_x emissions also increase significantly. Applying a linear increase in combustion air preheating will most probably also result in a linear increase in heat flux and firebox wall temperature [36], [37]. This will be tested using the test fired heater described in [Burner test methodology].

The ECAP that will be designed during this study should be able to heat up the combustion air to a temperature in the same range as used with the recuperative burners, to have a significant impact on the emissions and savings. That would be between 200-600°C. So preferably the system should be able to heat up the combustion air to at least a temperature of 300°C, according to Technip Energies.

2.6. Electric heating elements

To transfer the electrical energy to the air, heating elements are needed. These elements heat up due to their electrical resistance, called resistance heating. Resistance heating uses the heat generated by the Joule effect in a conductive material in which an electrical current flows. These heating systems comprise the following parts: heating elements, temperature control system and electric power supply. In the heating elements, i.e. resistors, the electrical energy is converted into heat, and they must have the following properties [38], [39].

- High operating temperature
- High electrical resistivity
- Temperature coefficient of resistivity low and positive
- Electrical properties and size constant in time
- High mechanical strength
- Ease of machining and welding
- Low chemical reactivity

The main requirement for the heating elements is the maximum operating temperature, which is based on the power and laws of heat transfer by radiation and convection. Calculations based on these provide useful information for the selection of heating elements and the capacity and dimensions of the system. The most common materials listed from lowest operating temperature to highest are metal alloys, silicon, and graphite. Indirect heating of the air via resistance heating can be accomplished with different types of heating elements [40], [41]. Namely:

- Open-coil heating elements
- Tubular heating elements
- Finned tubular heating elements

They are illustrated and compared in Figure 2.6.8 and

Table 2.6.1.

Table 2.6.1 - Types of heating elements compared.

Type of elements	Heat transfer	Pressure drop	Mechanical strength	Prone to Fouling
Open coil	highest	lowest	lowest	highest
Tubular	lowest	middle	middle	lowest

Finned tubular	middle	highest	highest	middle

Figure 2.6.8 – The three types of heating elements. Finned tubular (L), tubular (M) and open-coil (R).

Open coil heating elements often consist of Nickel/Chrome alloy helical resistance wires, bushing ceramics and a steel supporting construction. They generally have a very low pressure drop, fast heat transferring, high heat capacity per area and a quick response time. They are also easy to manufacture and a cheaper solution compared to tubular or finned tubular heating elements. Drawbacks are that they are not suitable for high humidity environments due to the direct contact with air, they are prone to fouling due to dust particles that can get stuck in the coils, and they need a support frame.

Tubular heating elements often consists of hollow stainless steel tubes with a Nickel/Chrome alloy resistance wire centered in magnesium powder inserted in the tube. Compared to open coils are they are less sensitive to humidity environments and have better mechanical strength, but they have a higher pressure drop, are more expensive, and have a lower heat capacity per area. The finned tubular elements are almost the same as the tubular elements, but in addition, they have stainless steel fins at the outer of the tubes, resulting in a higher heat transfer area and mechanical strength, but also a higher pressure drop and manufacturing costs.

There are many studies available on forced convection heat transfer from straight cylinders in cross-flow [42], [43] or on forced convection heat transfer from banks of straight tubes in cross-flow [44]. But despite the extensive use of open-coil air heaters, forced convection heat transfer from helically coiled resistance wires in cross-flow has not been researched academically that much or made open-access information. There are some papers concerning natural convection across helically coiled resistance wires like [45]–[47], and some concerning the forced convection [48]–[51].

For this specific application an high as possible operating temperature with a large heat transfer area is needed, so that the heat transfer can be maximized. A fouling proof and mechanically strong design needs to be chosen so that maintenance and failing of the equipment can be minimized. The theory behind the heat transfer and pressure drop over bare tubes and finned tubes will be discussed in [3.1 Heat transfer & pressure drop in tube banks], together with the radiation of these heating elements. It is important to understand the theory behind these mechanisms, so that the right type of heating element can be chosen.

3
Theory

3.1 Heat transfer & pressure drop in tube banks

To develop a cost-effective and compact electric combustion air preheater (ECAP) for the LSV® burner [52] a calculation method for the heat transfer and pressure drop is required. Multiple available methods will be discussed and compared, and the most suitable for this application will be chosen. The most suitable method will be discussed in more detail.

To understand the working principle of heating elements, i.e. a bank of tubes, one first has to understand the basic fundamentals of conductive, convective and radiative heat transfer, the correlations of experimental data and the flow behaviour across cylinders.

Convection is a form of heat transfer from a material to a moving fluid and is the most dominant form of heat transfer in this application. The flow of the fluid may be forced, for example, by pumping or using a fan, or natural (free), driven by buoyancy forces arising from a density difference. Either type can be internal, such as a pipe flow or external, in open spaces. Either type can also be laminar or turbulent, dependent on the Reynolds number.

Heat transfer rates tend to be much higher in turbulent than laminar flows, owing to the vigorous mixing of the fluid. The rate of heat transfer is usually a complicated function of surface geometry and temperature, fluid temperature and velocity, and the fluid thermophysical properties.

$$q = h_c A (T_s - T_b) \tag{1}$$

Most engineering calculations for convective heat transfer are based on correlations from experimental data [53]. In general, these correlations express the heat transfer coefficient h_c as the dimensionless Nusselt number Nu

$$\mathrm{Nu} = \frac{h_c L}{k} \tag{2}$$

Where L represents the characteristic length and k the thermal conductivity of the fluid. This formula can be written in multiple forms. Various correlations for the Nusselt number for a flow across a tube or bank of tubes can be found. These correlations are a function of the dimensionless Reynolds and Prandtl number.

$$\mathrm{Nu} = f(Re, Pr) \tag{3}$$

The flow over a tube bank can be steady or unsteady, laminar or turbulent and boundary layers are developed along the surface of the tubes. To understand these flow characteristics, one needs to understand the flow across a single cylinder.

Flow across a cylinder

The flow pattern around a cylinder depends very much on the Reynolds number that can be determined by

$$Re_D = \frac{V d_o}{v} \tag{4}$$

With V the velocity, d_o the diameter of the cylinder and v the kinematic viscosity.

The local skin friction coefficient, i.e. drag coefficient, is another important variable that varies in a complicated fashion around the cylinder. In practice, usually the total drag force on the cylinder due to both friction, i.e. viscous drag, and pressure imbalance, i.e. form drag is required. The total drag force F can be determined from the drag coefficient. The drag coefficient is dependent on the Reynolds number and is usually gained from experimental data or a correlation formula. Above $Re_D \approx 10^3$, the flow separates at $\theta \approx 80°$, and the form drag dominates to give $C_D = 1.2$, nearly independent of Reynolds number [53].

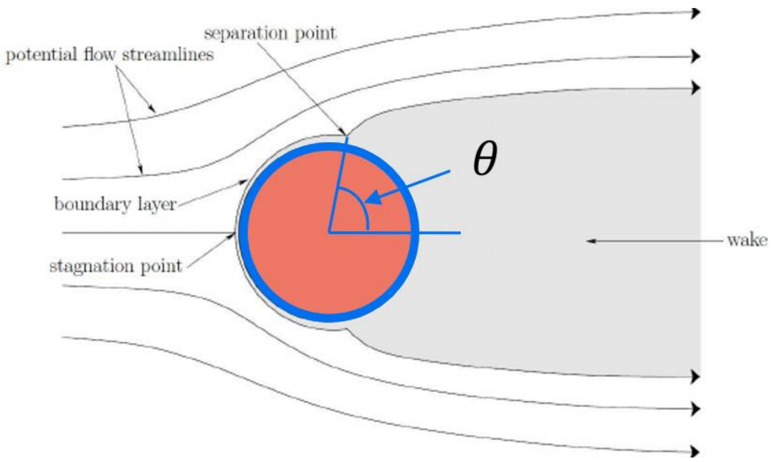

Figure 3.1.9 – The flow across a cylinder visualized with the important designations highlighted.

The corresponding variation of the local heat transfer coefficient around the cylinder is also very complicated, as might be expected. The Nusselt number is high on the front of the cylinder, where the boundary layer is thin and the Nusselt number decreases as the boundary layer grows in thickness around the cylinder. Along the cylinder where the flow does not separate, the Nusselt number decreases steadily, toward a minimum at the separation region.

There are multiple correlation formulas for the Nusselt number for a flow across a single cylinder. Four of the most well-known are, Hilpert [54], Zukauskas [44], Churchill & Bernstein [42] and Gnielinski [55]. These correlations with some adaptations are also used for the Nusselt number calculation of a flow across a bare tube bank and a finned tube bank, as discussed next.

Crossflow over a bare tube bank

Cross-flow over tube banks is widely used in the industry, for example in heat exchanger equipment. The tubes can be finned, but in this paragraph bare tubes are discussed. The finned tubes will be discussed in the next section. The configuration of the tubes inside the bank can be aligned or staggered, as shown in Figure 3.1.10. For this application, only the staggered arrangement is analyzed since a staggered arrangement often provides a better heat transfer [56].

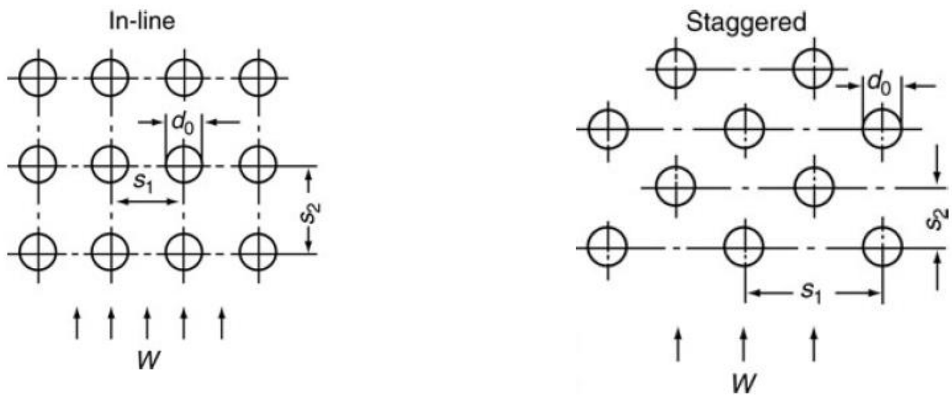

Figure 3.1.10 - Tube bank arrangement from [53].

The flow inside tube banks is complex, involving boundary layer separation on each tube and interactions of the resulting wakes with adjacent wakes and downstream tubes. Important parameters are the tube diameter, transverse and longitudinal pitch, the pitch ratios and the number of tubes transverse to the rows. The pitch ratios are the ratios between the tube diameter and the pitch in a certain direction. The heat transfer coefficient is initially larger in tube banks than for a single tube in cross-flow since the fluid must accelerate to pass through the spaces between adjacent tubes.

Three methods that are widely used to calculate the Nusselt number for a bare tube bank are described by the VDI Heat Atlas [57] from now on called VDI, the HTFS handbook [58] form now on called HTFS and the Basic Heat and Mass Transfer book [53] from now on called BHaMT. The equations for these methods are given in Table 3.1.1. The VDI and BHaMT methods use the same method to correct a correlation for a single cylinder for a bare tube bank based on the Gnielinski method [59], but they differ in the correlation used for the flow across a cylinder. The VDI method [60] uses the correlations of Gnielinski [55], while the BHaMT method [53] uses the correlations of Churchill & Bernstein [42].

The HTFS method [61] uses another method to correct the correlation for a single-cylinder so that it can be used for a bare tube bank. It uses an equation like the correlations of Zukauskas [44], with multiple correction factors to tune the correlation to the specific application. All methods are provided on the next page in Table 3.1.1.

Table 3.1.1 – The equations used for each method to calculate the Nusselt number for the bare tube banks. A more detailed explanation can be found in the Appendix.

VDI (Gnielinski single cylinder correlation)

$$\overline{Nu}_{l,0} = 0.3 + \sqrt{\overline{Nu}_{l,lam}{}^{2} + \overline{Nu}_{l,turb}{}^{2}} \qquad 10 < Re_{\psi,l} < 10^{6} \tag{5}$$

$$\overline{Nu}_{l,lam} = 0.664 \mathrm{Re}_{\psi,l}{}^{1/2} \mathrm{Pr}^{1/3} \tag{6}$$

$$\overline{Nu}_{l,turb} = \frac{0.037 \mathrm{Re}_{\psi,l}^{0.8} \mathrm{Pr}}{1 + 2.443 \mathrm{Re}_{\psi,l}^{-0.1} (\mathrm{Pr}^{2/3} - 1)} \tag{7}$$

BHaMT (Churchill & Bernstein single cylinder correlation)

$$\overline{Nu}_{l,0} = 0.3 + \frac{0.62 \mathrm{Re}_{D}^{12}\ \mathrm{Pr}^{1/3}}{\left[1 + (0.4/\mathrm{Pr})^{2/3}\right]^{1/4}} \qquad 0 < \mathrm{Re}_D < 10^4 \tag{8}$$

$$\overline{Nu}_{l,0} = 0.3 + \frac{0.62 \mathrm{Re}_{D}^{1/2} \mathrm{Pr}^{1/3}}{\left[1 + (0.4/\mathrm{Pr})^{2/3}\right]^{1/4}} \left[1 + \left(\frac{\mathrm{Re}_D}{282{,}000}\right)^{1/2}\right] \qquad 2 \times 10^4 < \mathrm{Re}_D < 4 \times 10^5 \tag{9}$$

$$\overline{Nu}_{l,0} = 0.3 + \frac{0.62 \mathrm{Re}_{D}^{1/2}\ \mathrm{Pr}^{1/3}}{\left[1 + (0.4/\mathrm{Pr})^{2/3}\right]^{1/4}} \left[1 + \left(\frac{\mathrm{Re}_D}{282{,}000}\right)^{5/8}\right]^{4/5} \qquad 4 \times 10^5 < \mathrm{Re}_D < 5 \times 10^6 \tag{10}$$

VDI and BHaMT bare tube bank calculation method

$$\overline{Nu}_{bundle} = \overline{Nu}_{0,bundle}\, K_{\mathrm{G}} \tag{11}$$

$$\overline{Nu}_{0,bundle} = f_{\mathrm{A}} \overline{Nu}_{l,0} \qquad for\ \#\ of\ rows\ n \geq 10 \tag{12}$$

$$\overline{Nu}_{0,bundle} = \frac{1 + (n-1) f_A}{n} \overline{Nu}_{l,0} \qquad for\ \#\ of\ rows\ n < 10 \tag{13}$$

With the arrangement factor f_{A} and a correction factor K_{G}.

HTFS bare tube bank calculation method

$$\mathrm{Nu}_{\mathrm{bundle}} = a\, Re_D^m Pr_b^{0.34} \phi_1 \phi_2 \phi_3 \tag{14}$$

With constants a and m and correction factors ϕ_1, ϕ_2, ϕ_3.

Comparing these methods, there are some differences in the assumed information to be known, the temperature used for physical properties and the Reynolds number calculation. The most significant difference in the information to be known is that the HTFS method uses a fixed length for the tube bank depth compared to the VDI method. The physical properties used are different for each method since the specific temperature used is also different for each method. The VDI and the HTFS method uses the mean temperature between the inlet and the outlet as given by

$$T_{\mathrm{M}} = \frac{(T_{\mathrm{in}} + T_{\mathrm{out}})}{2} \tag{15}$$

The BHaMT method states that properties are to be evaluated at the mean temperature between the inlet and the outlet for liquids and the mean film temperature for gases. (average of the mean temperature of the in- and outlet and the film temperature). Given by:

$$T_{\mathrm{M}} = \frac{1}{2}\left(T_S + \frac{(T_{\mathrm{in}} + T_{\mathrm{out}})}{2}\right) \tag{16}$$

Comparing the calculation methods for the Reynolds number, the VDI method uses the mean velocity $w = w_0/\psi$ with w_0 the velocity in the cross-section in an empty channel and $\psi = 1 - \frac{\pi}{4a}$, a streamed length of $L = \pi d/2$ and the kinematic viscosity v, resulting in the equation

$$\mathrm{Re}_{\psi,\mathrm{l}} = \frac{w_0 L}{\psi v} \tag{17}$$

The procedure similar to that of Gnielinski, but with the correlation of Churchill & Bernstein, which is recommended by the BHaMT method, uses the velocity in the cross-section in an empty channel w_0, a streamed length of d_{o} and the kinematic viscosity v, resulting in the equation

$$Re_D = \frac{w_0 d_{\mathrm{o}}}{v} \tag{18}$$

The HTFS method the same formula as the BHaMT method to calculate the Reynold number, only with different parameters. It uses a streamed length of d_{o}, the mass flow $\dot{m}$, the dynamic viscosity of the bulk η_{b} and the minimum cross-flow area A_{m}, resulting in the equation.

$$Re_D = \frac{\dot{m} d_{\mathrm{o}}}{\eta_{\mathrm{b}} A_{\mathrm{m}}} \tag{19}$$

Crossflow over a finned tube bank

The heat release and absorption from surfaces can be enhanced by adding fins [56], [62]. Normally the fins are placed on the side with the lower heat transfer within the heating tubes. The basic requirement is an ideal contact between the fin and the fin base on the tube and that the fluid flow direction corresponds to the orientation of the fins. A mean heat transfer coefficient has to be found and evaluated based on the geometry of the fins.

Two methods that are widely used to calculate the Nusselt number for a finned tube bank are again described by the VDI Heat Atlas [57] and the HTFS handbook [58]. The Nusselt number is used to calculate the heat transfer coefficient of the finned tubes. Both methods do not take the fin top area into account as well as losses due to fouling. They both use a correction on the heat transfer coefficient for the fin efficiency and geometry.

Table 3.1.2 - The equations used for the VDI and HTFS method to calculate the Nusselt number for the finned tube banks.

VDI finned tube bank calculation method

$$\overline{Nu}_D = 0.38\mathrm{Re}_\mathrm{d}^{0.6}\left(\frac{A}{A_\mathrm{t0}}\right)^{-0.15}\mathrm{Pr}^{1/3} \tag{20}$$

$$\frac{A}{A_\mathrm{t0}} = 1 + 2\frac{h_\mathrm{f}(h_\mathrm{f} + d_0 + \delta)}{s d_0} \tag{21}$$

HTFS bare tube bank calculation method

$$Nu = Nu_1 Nu_2 Nu_3 \tag{22}$$

$$Nu_1 = 0.292\mathrm{Re}_D^n \qquad \textit{with } n = \{0.585 + 0.0346\ln(d_f/f_s)\} \tag{23}$$

$$Nu_2 = \mathrm{Pr}^{0.333}\left(\frac{f_S}{d_f}\right)^{1.115}\left(\frac{f_S}{h_f}\right)^{0.257} \tag{24}$$

$$Nu_3 = \left(\frac{\delta}{f_s}\right)^{0.666}\left(\frac{d_f}{d_r}\right)^{0.473}\left(\frac{d_f}{\delta}\right)^{0.7717} \tag{25}$$

Comparing these two methods, there are again some differences in the assumed information to be known and the Reynolds number calculation. This is the same as with the crossflow over a bare tube bank.

Comparing the calculation for the Reynolds number, the VDI method uses the mean velocity $w = w_0/\psi$ with w_0 the velocity in the cross-section in an empty channel and $\psi = 1 - \frac{\pi}{4a}$, a streamed length of $L = \pi d/2$ and the kinematic viscosity v, resulting in the equation

$$\mathrm{Re}_{\psi,\mathrm{l}} = \frac{w_0 L}{\psi v} \tag{26}$$

The HTFS method uses a rather different formula to calculate the Reynold number. It uses a streamed length of d_0, the mass flow $\dot{m}$ and a minimum crossflow area for the finned tube S_m, resulting in the equations.

$$\mathrm{Re_c} = \frac{\dot{m} d_\mathrm{o}}{\eta_\mathrm{b} S_\mathrm{m}} \tag{27}$$

$$S_m = N_c \left(P_y - d_r - \frac{2 f_t f_h}{p_f} \right) L_t \tag{28}$$

Pressure drop of a tube bank

To calculate the pressure drop of a bare tube bank, multiple methods and correlations can again be used. All methods use the same equation form, but with different ways to calculate correction factors for the temperature differences, the number of rows used and tube arrangement. A method for the calculation of the pressure drop for a finned tube bank is only provided by HTFS. Again different correction factors for the friction factor and tube arrangement are calculated.

Table 3.1.3 – The equations used for the VDI, BHaMT and HTFS method to calculate the pressure drop for the bare tube bank.

VDI bare tube bank calculation method

$$\Delta P = \xi\, N_R \left(\rho_b \frac{{w_{max}}^2}{2} \right) \tag{29}$$

BHaMT bare tube bank calculation method

$$\Delta P = N_R \left(\rho_b \frac{{w_{max}}^2}{2} \right) f \tag{30}$$

HTFS bare tube bank calculation method

$$\Delta P = C \frac{L}{D} \left(\rho_b \frac{{w_{max}}^2}{2} \right) f \tag{31}$$

HTFS finned tube bank calculation method

$$\Delta P_f = 4 f N_R \frac{\dot{M}_c^2}{2 \rho_b S_m^2} \tag{32}$$

Radiation of a tube bank

Apart from convective heat transfer inside the ECAP, radiative heat transfer also occurs. Thermal radiation is a form of electromagnetic radiation which occurs in all matter and space. A particle of electromagnetic energy is a photon and the heat transfer can be viewed either in terms of electromagnetic waves or in terms of photons. The flux of radiant energy incident on a surface is called irradiation (G) and the energy flux leaving a surface due to emission and reflection of electromagnetic energy is called radiosity (J).

These two are of importance for the definition of the two types of surfaces. A black surface, i.e. blackbody, is defined as a surface that absorbs all incident radiation (irradiation) and reflects none. Hence, all radiation leaving a black surface is emitted by the surface and is given by the Stefan-Boltzmann law:

$$J = E_b = \sigma T^4 \tag{33}$$

With E_b the blackbody emissive power, T the absolute temperature (K) and σ the Stefan-Boltzmann constant ($\sim 5.67\ \times 10^{-8}$ W/m²·K⁴).

The black surface is an ideal surface. A real surface absorbs less radiation and is called a grey surface. The fraction of incident radiation that is absorbed is called the absorptance α, and the fraction reflected is the reflectance ρ. For object that are opaque, i.e. not transparent to electromagnetic radiation, the following equation is valid. Both are constants values for surfaces.

$$\rho + \alpha = 1 \tag{34}$$

Real surfaces (grey surfaces) also emit less radiation than black surfaces. The fraction of the black surface emissive power emitted by the grey surface is called the emittance ε. The emittance is equal to the absorptance, and constant and independent of its temperature.

If heat is transfer via radiation between two finite size grey surfaces, the rate of heat flow will depend on the temperatures, emittances and geometry of the surfaces. Determining the rate of heat flow is difficult, but in general the following equation is used [53].

$$\dot{Q}_{12} = \ A_1 F_{12} \sigma (T_1^4 - T_2^4) \tag{35}$$

With $\dot{Q}_{12}$ the net radiant energy heat transfer from surface 1 to 2, and F_{12} the shape factor depending on the geometry.

Considering a square box, grey surface 1 enclosed by another square box, grey surface 2. Both having a specific surface area and uniform temperature. By symmetry, the irradiation and radiosity of the surfaces are also uniform. The fraction of energy leaving surface 1 and intercepted by surface 2 is $J_1 A_1 F_{12}$, where the shape factor F_{12} is the same that is introduced for black surfaces, because of the assumption that the grey surfaces are diffuse emitters and reflectors. Likewise the energy leaving surface 2 that is intercepted by surface 1 is $J_2 A_2 F_{21}$. Using the reciprocal rule and conservation of energy, and by eliminating the radiosities the net radiant energy transfer can be written as:

$$\dot{Q}_{12} = \frac{E_{b1} - E_{b2}}{\frac{1-\varepsilon_1}{\varepsilon_1 A_1} + \frac{1}{A_1 F_{12}} + \frac{1-\varepsilon_2}{\varepsilon_2 A_2}} \tag{36}$$

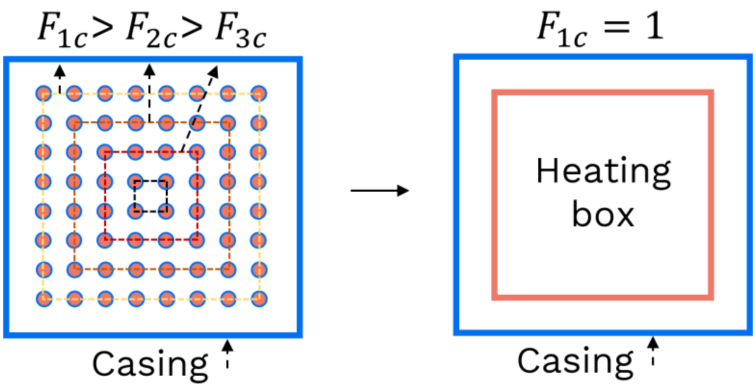

Figure 3.1.11 – simplification of the tube bank for the calculation of the radiation from the tube bank to the wall.

Considering a geometry as graphically shown in Figure 3.1.11, in which the tube bank can be simplified to a square box placed inside another square box. F_{1c} , F_{2c} and F_{3c} represent the shape factor from the nth row in the tube bank to the casing wall. By simplifying the geometry the shape factor F_{1c} becomes 1. The equation becomes:

$$\dot{Q}_{12} = \frac{\varepsilon_1 A_1}{1 + \frac{\varepsilon_1 A_1}{\varepsilon_2 A_2}(1-\varepsilon_2)}(E_{b1} - E_{b2}) \tag{37}$$

The radiation from the tube bank to the air can be neglected, since the only radiative species in air is H_2O, which is a minor component of air. They slightly absorb or reflect the radiative heat, but this is really small. CO_2 is also a radiative species, but it is in very small amounts present in air. It becomes more relevant in the combustion chamber, where CO_2 is present in larger amounts and the radiation is more important for the characteristics of the fired heater [63].

The radiative heat transfer from the tube bank to the casing will eventually also heat up the air, since the air extracts the heat out of the isolated casing by convection. For further calculations, the radiation of the tube bank is neglected, since this only account for less than 4% of the heat transferred from the tube bank to the air by convection. This is calculated using an emissivity of 0.7 for the grey surfaces (stainless steel 321) and an inside box temperature of 650°C and an outside box temperature of 200°C. The air outlet temperature calculated during this thesis using the correlations for convective heat transfer will therefore be slightly below the actual air outlet temperature achievable.

3.2. Burner NO_x formation

As discussed in [], nitrogen oxides (NO_x) are formed during combustion. NO is mostly produced in the reaction zone, and the subsequent oxidation from NO to NO_2 occurs in the post-burn process away from the combustion zone [31], [64], [65].

The formation of nitrogen oxides in flames is generally controlled by three routes:

- Thermal NO_x (T-NO_x) – formed from atmospheric nitrogen and oxygen and is a function of combustion temperature.
- Fuel NO_x (F-NO_x) – formed from nitrogen in the fuel and is a function of the fuel composition.
- Prompt NO_x (P-NO_x) – formed from atmospheric nitrogen and fuel and is a function of mixture stoichiometry.

T-NO_x is often the dominant mechanism due to the high temperatures in most combustion flames. The understanding of the formation of T-NO_x is based on the Zeldovich mechanism [66]. The rate of formation rapidly increases with increasing temperature as a result of a high activation energy. T-NO_x is also the mechanism that's most important for this master thesis, since the flame temperature will probably change due to a higher combustion air temperature.

F-NO_x formation is commonly found with nitrogen-bearing fuels, but it is almost absent in natural gas-fired flames since natural gas contains almost no nitrogen compared to coal/oil. However, that does not imply that natural gas fuel has lower NO_x emissions because their flame temperatures are often higher. The F-NO_x is formed through oxidation of the nitrogen contained in the fuel and is created once the nitrogen is bound to the fuel by excess oxygen during combustion. The production of F-NO_x is dependent on the stoichiometric ratio between air and fuel.

P-NO_x occurs mostly in fuel-rich systems and is based on the Fenimore mechanism [67]. The formation mechanism involving hydrocarbon radicals and atmospheric nitrogen depends on the mixing rate of fuel and air. P-NO_x is more prominent at lower temperatures, and it is called prompt NO_x because of the very early appearance at the flame front, i.e. fuel-rich regions.

Applying the NO_x emissions reduction techniques that will be discussed on the next page controls the flame core stoichiometry and peak flame temperature, which decrease mostly the T-NO_x formation. This makes the P-NO_x the more important mechanism, when the others are suppressed [68].

Dependency of NO_x formation on different parameters

NO_x control requires control of one or more parameters that affect NO_x generation in a flame, which are flame temperature [69], residence time of hot gases in the flame [70], oxygen availability (especially in the hottest part), fuel-air equivalence ratio and type of fuel. Each of these parameters is interdependent, fluctuating and plant-specific. There is often a dilemma between reducing NO_x formation and reducing CO formation. If all three parameters are reduced, the formation of both NO and CO_2 will be reduced, resulting in an increase in CO formation [71].

Reducing the NO_x emissions can be achieved by [72], [73], [37]:

- Introducing an inert species – most commonly achieved by adding flue gas recirculation (FGR) to the combustion air. (reburning)
- Combustion control – by changing the fuel or modifying the mixing. For instance by staging and swirling.
- Reduce or increase the amount of air preheat – depends on the fired heater design.
- Post-combustion exhaust treatment - A catalyst can be used to filter the flue gases.

The combustion control includes reducing the oxygen and/or nitrogen in the flame zone, reducing the peak temperature, and reducing the residence time at elevated temperatures. Another combustion control method applied commercially, like at the LSV® burner, is the use of combustion staging. The mixing of the fuel and air in the flame is delayed to create zones with a typical air/fuel ratio [20], [74]. Combustion staging may affect the heat transfer and flame volume. The reaction rates are lower in the secondary burnout zone than those operating under conventional conditions, resulting in a larger flame volume.

A specific type of staged combustion is flameless combustion, which is combustion with an almost non-visible flame. This can be achieved when both the firebox temperature and recirculation ratio of the flue gases are high enough. The firebox temperature should be above the auto-ignition temperature, and the recirculation ratio of the flue gases should be higher than 3 and lower than 20 for flameless combustion. If the firebox temperature requirement is not met, the flame becomes unstable and could blow out, as is graphically shown in Figure 1.2.1. For natural gas-fired burners, the firebox temperature should be above 750°C [64].

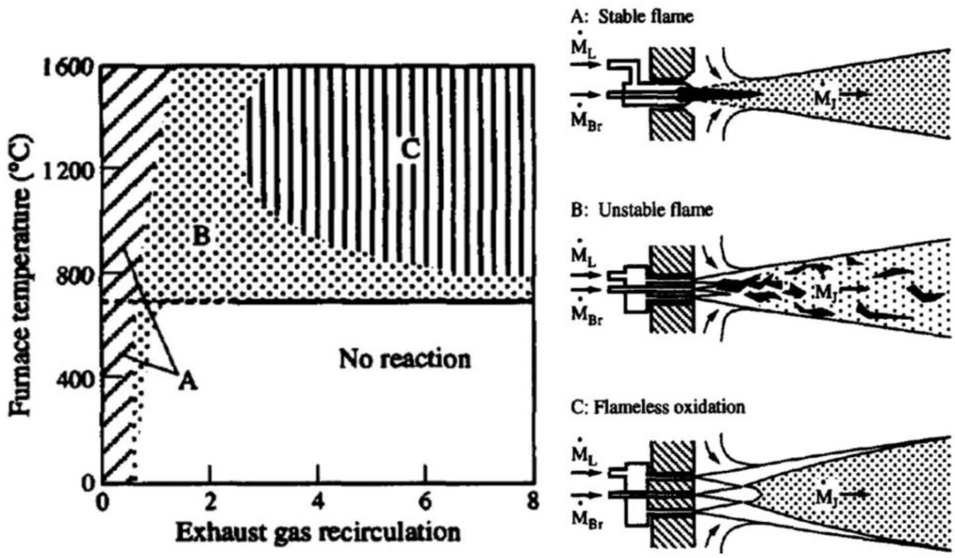

Figure 3.2.12 – The required firebox (fired heater) temperature when firing with NG for flameless combustion from [64].

MILD combustion (Moderate or Intense Low-oxygen Dilution combustion) is another combustion control method which is investigated extensively. It is characterized by low-oxygen concentrations due to intensely burned gas recirculation and high inlet temperatures. The characteristics of the oxidation process are a homogeneous temperature, distributed ignition, the absence of a visible flame and low CO, NO_x and soot emissions [63]. MILD combustion is often called flameless combustion and the understanding of staged combustion and flameless combustion is important for the understanding of literature regarding NO_x formation.

During flameless combustion, the temperature profile is almost uniform within the flame, avoiding hot spots, which results in a significant reduction of thermal NO_x formation. This is the result of the dilution of the combustion air and/or fuel with flue gases inside the fired heater. The temperature fluctuation inside the flame decrease because of the low O2 concentrations. The colour and size of the flame also depend on the natural gas composition, fuel chemical property, oxygen concentration and combustion air preheat temperature.

So NO_x formation is dependent on the oxygen percentage in the combustion products, therefore also dependent on the amount of excess air. A graph showing this phenomenon is given in Figure 3.2.13 from [75]. It should be noted that the rate of increase of NO_x formation is also dependent on the burner design, fuel and combustion air characteristics and burner and fired heater layout. So, this graph shows a generic curve and is not applicable to individual low NO_x burner designs. This trend in NO_x formation is confirmed in multiple other sources, in which burner tests are conducted at different oxygen concentrations in the combustion products [76]–[78]. The oxygen percentage in the combustion products in typical process heaters is normally maintained at 2% during operation [18].

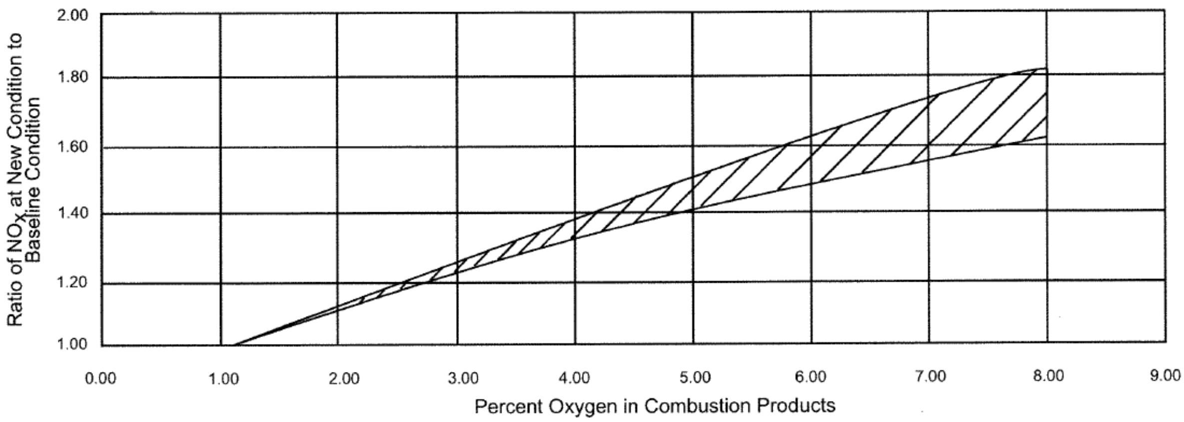

Figure 3.2.13 - Effect of percent oxygen in combustion products on NO_x formation from [75].

The NO_x formation will also increase as the firebox temperature increases, since in certain cases this results in an increase in local gas temperature. The firebox temperature is dependent on the choice of burner configuration and burner heat flux variations within the fired heater. A graph showing this dependency of NO_x formation on the firebox temperature is given in Figure 3.2.14 from [75]. Again, it should be noted that this is also dependent on multiple other factors affecting the NO_x formation during operation, so this graph shows a generic curve and is not applicable to individual low NO_x burner designs. This trend in NO_x formation is also confirmed in multiple other sources [36], [79] and is applicable for well-mixed fired heaters with a uniform temperature.

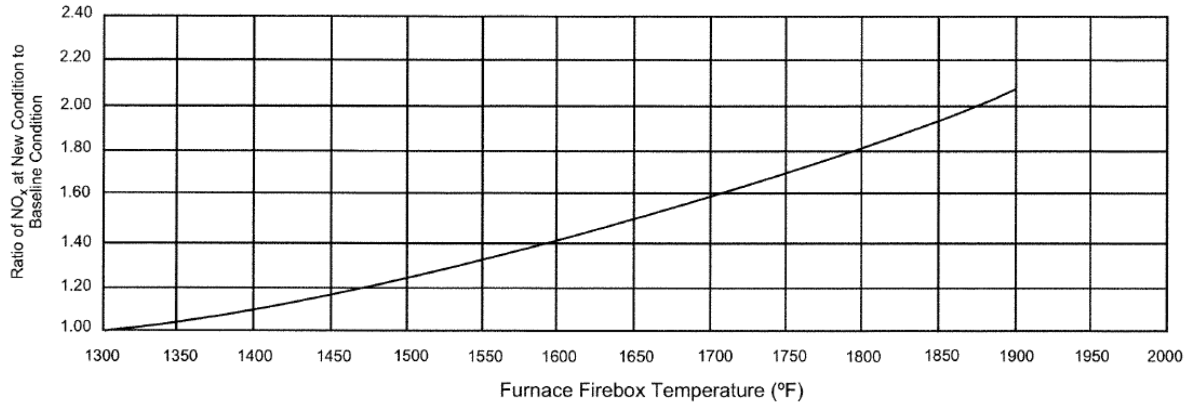

Figure 3.2.14 - Effect of the firebox temperature on NO_x formation from [75].

The use of preheated combustion air results in an increase in NO_x emissions, especially in traditional combustion. It is generally accepted that the increase in NO_x formation is dependent on the flame temperature, which increases with increasing combustion air temperature. A graph showing this phenomenon is given in Figure 3.2.15 from [75]. It should be noted that the rate of increase of NO_x formation is also dependent on the burner design, fuel and combustion air characteristics and burner and fired heater layout. So, this graph shows a generic curve and is not applicable to individual low NO_x burner designs. This trend in NO_x formation is confirmed in multiple other sources, in which burner tests are conducted at high combustion air temperatures [76], [77], [36], [64], [80].

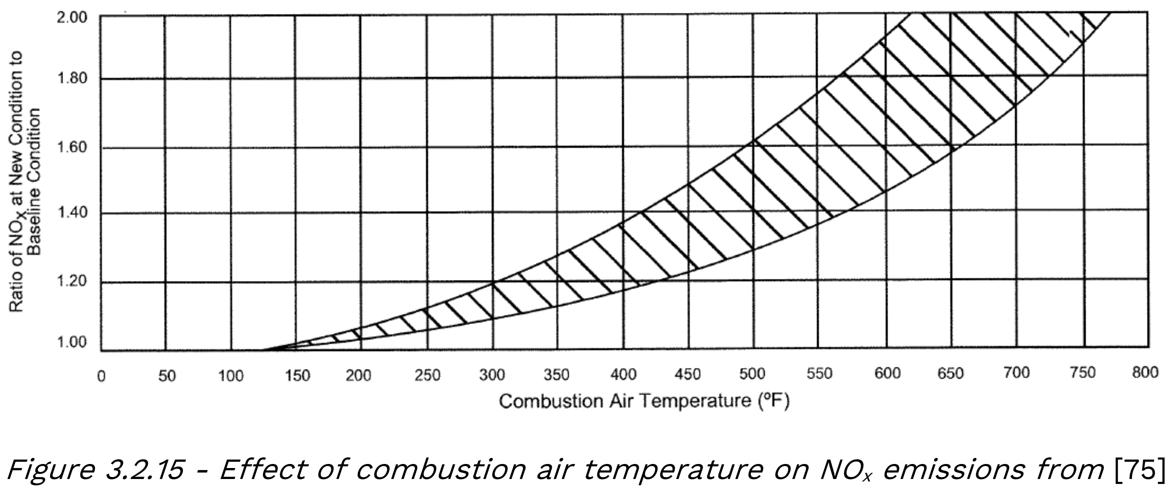

Figure 3.2.15 - Effect of combustion air temperature on NO_x emissions from [75].

Correlations for determining NO_x emissions

Finding correlations for the formation of NO_x during combustion in fired heaters could be valuable for predicting the NO_x increase for this specific application. Finding a reliable correlation is difficult due to the number of parameters that affect NO_x formation. Despite the difficulty, some researchers have tried to derive a correlation for the scaling of NO_x emissions [81], [65], [82].

The adiabatic flame temperature (AFT) is an important parameter for the formation of Thermal NO_x, because it is the highest attainable temperature and it provides information on maximal thermal-NO_x formation. It can be theoretically calculated by assuming complete combustion of the fuel gas. A correlation based on the AFT is derived by [81] for hydrogen reforming fired heaters with about 2% excess O2. This is not validated for higher temperatures, other percentages of excess air and using ethylene fired heaters. This correlation may require adjustments for this specific application.

The study on MILD combustion [65] found that although firing rate, dilution, heat extraction, air preheating, excess air and fuel type all affect the NO_x emissions, but none of them is the dominant factor. A correlation based on the global residence time and characteristic fired heater temperature provided the best correlation compared to the other methods but was considered not good enough. The dependence of temperature was found to be much weaker than expected based on the Thermal NO_x mechanism alone. This would suggest that no single NO_x mechanism is dominant in MILD combustion, meaning that the Prompt NO_x mechanism is of significance comparable to that of Thermal NO_x [68].

According to Technip Energies [18], most engineering companies use in-house information to derive a correlation for NO_x formation in hydrogen and ethylene fired heaters. Preferably this is done by finding a correlation based on the NO_x emissions from similar application and burners. If that’s not possible, a data fit correlation is used from standard burner emissions. Technip uses a correlation based on the adiabatic flame temperature with correction factors for the specific firebox temperature and burner type based on [81].

3.3. Heat flux within the fired heater

The heat flux is in the context of fired heaters, the amount of heat transfer through the heater tubes per unit of outer surface area. When talking about the heat flux within a fired heater, it is usual to provide the specific section of the fired heater in which this heat flux is found, since the heat flux is different per section. For instance the radiant section average heat flux. It is also important to know the maximum heat flux, i.e. peak heat flux, in a fired heater. Most fired heaters are specified with a maximum allowable radiant section average heat flux. A high heat flux results in a high radiant tube wall temperature and coking of hydrocarbon in the heating tubes.

The heat flux profile of the fired heater tells something about the reliability and performance of the fired heater. A well designed fired heater has a evenly spread heat flux. The amount of heat flux and how the heat flux is distributed is dependent on the amount of fuel that is burned and the fuel type, the temperature of the combustion air and firebox, and the recirculation of the burned gas.

3.4. FloEFD CFD Solver

For this study a CFD model is build and analyzed using FloEFD (version 2020.2). FloEFD is a commercial CFD software package that can be embedded as an add-in in existing CAD software programs like SolidWorks. The solver used on FLoEFD uses certain equations to predict the laminar and turbulent flow and uses a numerical method to solve these equations in a certain mesh. This section provides the governing equations and numerical method used in FLoEFD.

Governing equations

It solves the Navier-Stokes equations, which are equations of mass, momentum, and additional to that it solves energy conservation laws for fluid flows. These are supplemented by fluid state equations defining the nature of the fluid, and by empirical dependencies of fluid density, viscosity and thermal conductivity, on temperature. A particular problem is finally specified by the definition of its geometry, boundary and initial conditions.

To predict turbulent flows, the *Favre-averaged Navier-Stokes* equations are used to calculate time-averaged properties of the flow. To close the system of equations, FloEFD employs the so-called *k-ε model* for transport equations for the turbulent kinetic energy and its dissipation rate. This model is considered to be one of the most popular turbulence models, since it has a good numerical stability and convergence. The *k-ε model* also has a well-defined region of capability, meaning that is relative easy to investigate whether the model can be used for a specific engineering problem [83].

The following equations are used to solve the CFD model. Formally, these equations describe both laminar and turbulent flow, and the transition, but different sub models are needed in each case. More information can be found in the technical reference of FloEFD [84].

The conservation laws for mass, linear momentum and energy in the cartesian coordinate system can be written in the conservation forms as follows:

$$\frac{\partial \rho}{\partial t} + \frac{\partial}{\partial x_i}(\rho u_i) = 0 \tag{38}$$

$$\frac{\partial \rho u_i}{\partial t} + \frac{\partial}{\partial x_j}(\rho u_i u_j) + \frac{\partial p}{\partial x_i} = \frac{\partial}{\partial x_j}\left(\tau_{ij} + \tau_{ij}^R\right) + S_i \qquad i = 1,2,3 \tag{39}$$

$$\frac{\partial \rho H}{\partial t} + \frac{\partial \rho u_i H}{\partial x_i} = \frac{\partial}{\partial x_i}\left(u_j\left(\tau_{ij} + \tau_{ij}^R\right) + q_i\right) + \frac{\partial p}{\partial t} - \tau_{ij}^R \frac{\partial u_i}{\partial x_j} + \rho\varepsilon + S_i u_i + Q_H \tag{40}$$

$$H = h + \frac{u^2}{2} + \frac{5}{3}k - \sum_m h_m^0 y_m \tag{41}$$

For Newtonian fluids the viscous shear stress tensor is defined as:

$$\tau_{ij} = \mu\left(\frac{\partial u_i}{\partial x_j} + \frac{\partial u_j}{\partial x_i} - \frac{2}{3}\delta_{ij}\frac{\partial u_k}{\partial x_k}\right) \tag{42}$$

Following Boussinesq assumption, the Reynolds-stress tensor has the following form:

$$\tau_{ij}^{R} = \mu_t\left(\frac{\partial u_i}{\partial x_j} + \frac{\partial u_j}{\partial x_i} - \frac{2}{3}\delta_{ij}\frac{\partial u_k}{\partial x_k}\right) - \frac{2}{3}\rho k\delta_{ij} \tag{43}$$

μ_t and k are zero for laminar flows. The *k-ε model* defines the turbulent viscosity μ_t using two basic turbulence properties, namely, the turbulent kinetic energy k and the turbulent dissipation rate ε.

$$\mu_t = f_\mu \frac{C_\mu \rho k^2}{\varepsilon} \tag{44}$$

Here f_μ is a turbulent viscosity factor and is defined by following the expression with y (the distance to the wall).

$$f_\mu = \left[1 - \exp\left(-0.0165 R_y\right)\right]^2 \cdot \left(1 + \frac{20{,}5}{R_T}\right) \tag{45}$$

$$R_T = \frac{\rho k^2}{\mu\varepsilon} \tag{46}$$

$$R_y = \frac{\rho\sqrt{k}y}{\mu} \tag{47}$$

Two additional transport equations are used to describe the turbulent kinetic energy and dissipation:

$$\frac{\partial \rho k}{\partial t} + \frac{\partial}{\partial x_i}(\rho u_i k) = \frac{\partial}{\partial x_i}\left(\left(\mu + \frac{\mu_t}{\sigma_k}\right)\frac{\partial k}{\partial x_i}\right) + S_k \tag{48}$$

$$\frac{\partial \rho \varepsilon}{\partial t} + \frac{\partial}{\partial x_i}(\rho u_i \varepsilon) = \frac{\partial}{\partial x_i}\left(\left(\mu + \frac{\mu_t}{\sigma_\varepsilon}\right)\frac{\partial \varepsilon}{\partial x_i}\right) + S_\varepsilon \tag{49}$$

Where the source terms S_k and S_ε are defined as

$$S_k = \tau_{ij}^{R}\frac{\partial u_i}{\partial x_j} - \rho\varepsilon + \mu_t P_B \tag{50}$$

$$S_\varepsilon = C_{\varepsilon_1}\frac{\varepsilon}{k}\left(f_1 \tau_{ij}^{R}\frac{\partial u_i}{\partial x_j} + \mu_t C_B P_B\right) - C_{\varepsilon_2} f_2 \frac{\rho\varepsilon^2}{k} \tag{51}$$

Here P_B represents the turbulent generation due to buoyancy forces and can be written as:

$$P_B = -\frac{g_i}{\sigma_B}\frac{1}{\rho}\frac{\partial\rho}{\partial x_i} \tag{52}$$

The constant σ_B = 0.9, and constant C_B defined as 1 when P_B>0 and 0 otherwise. The other constants are defined empirically.

$$f_1 = 1 + \left(\frac{0.05}{f_\mu}\right)^3 \tag{53}$$

$$f_2 = 1 - \exp(-R_T^2) \tag{54}$$

And for the other constants the following typical values are normally used:

$$C_\mu = 0.09, \qquad C_{\varepsilon_1} = 1.44, \qquad C_{\varepsilon_2} = 1.92, \qquad C_\varepsilon = 1.3, \qquad \sigma_k = 1$$

To describe the flows in near-wall regions, a laminar/turbulent boundary model is used, i.e. *Two-Scales Wall Functions (2SWF) Model*, which consist of two approaches coupling the boundary layer calculation with the main flow properties. This model is employed to characterize laminar and turbulent flows near the walls and the transitions from laminar to turbulent and vice versa.

To describe the boundary layer on a fine mesh (number cells across the boundary layer is 6 or greater) the *thick-boundary-layer* approach is used. In this approach the calculation of parameters of laminar boundary layer is doing via Navier-Stokes equations and for the turbulent boundary layer is performed by the so-called *Modified Wall Function approach*. This model uses a *Van Driest's profile* instead of the classical approach where the logarithmic velocity profile is used.

If the size of the mesh cell near the wall is more than the boundary layer thickness (number of cells across the boundary layer is 4 or less), the *thin-boundary-layer* approach, is used. In this approach the Prandtl boundary layer equations already integrated along the normal to the wall (from the wall to the dynamic boundary layer thickness) are solved along a fluid streamline covering the walls. If the boundary layer is laminar these equations are solved with a method of successive approximations based on the *Shvetz Trial Functions Technology*. If the boundary layer is turbulent or transitional, a generalization of this method to such boundary layers employing the Van Driest hypothesis about the mixing length in turbulent boundary layer is used.

In intermediate cases, a compilation of the two above approaches is used, ensuring a smooth transition between the two models as the mesh is refined, or as the boundary layer thickens along the surface. In addition to the 2SWF model, the thin-channel approach is used to describe the flow through narrow slots on a coarse mesh (number of cells across a slot is 7 or less). According to this approach, the shear stress and heat flux near the wall are calculated by using approximations based on experimental data. By default, an appropriate boundary-layer approach is selected automatically according to the computational mesh.

The system of Navier-Stokes equations is supplemented by definitions of thermophysical properties and state equations for the fluids. FloEFD provides simulations of gas and liquid flows with density, viscosity, thermal conductivity, specific heats, and species mixtures, as well as equilibrium volume condensation of water from steam can be taken into account when simulating steam flows. Excluding special cases (real gases, water vapor condensation and relative humidity), gases are considered ideal, i.e. having the state equation of the form

$$\rho = \frac{P}{RT} \tag{55}$$

Where, R is the gas constant which is equal to the universal gas constant R_{univ} divided by the fluid molecular mass M_m, or, for the mixtures of ideal gases.

$$R = R_{\text{univ}} \sum_m \frac{y_m}{M_m} \tag{56}$$

Specific heat at constant pressure, as well as the thermophysical properties of the gases, i.e. viscosity and thermal conductivity, are specified as functions of temperature. The state equation of ideal gas become inaccurate at high pressure or in close vicinity of the gas-liquid phase transition curve. Taking this into account, a real gas state equation together with the related equations for thermodynamical and thermophysical properties should be employed in such conditions. At present, this option may be used only for a single gas, probably mixed with ideal gases.

Numerical method

FloEFD computational approach is based on a generated mesh grid on which the governing equations are numerically solved. It solves the governing equations with a discrete numerical technique based on the *finite volume method*.

A mesh grid can be classified in two categories based on topology, structured and unstructured grids. Compared to structured grids defined by a global arrangement, unstructured grid cells are defined by local connections and can have varying shape. In terms of accuracy and complexity, both types have their advantages and disadvantages and are widely used by CFD software packages. Both mesh grids can also be combined, forming a hybrid grid. The mesh grid can also be classified based on the cell geometry. For two dimensional problems, the triangle and quadrilateral shaped cells are often used and for three dimensional problems tetrahedron and hexahedron shaped cells. The number of edges and faces play a role in the accuracy of the calculations that can be reached. For the same amount of cells, the accuracy of solutions in hexahedral meshes is the highest.

The mesh generation used in FloEFD is an automated structured mesh generator. That means that the mesh grid is less personalized but easier and faster to generate and easier to adjust. The mesh generation of FloEFD will automatically calculate the boundary layer thickness and will include cells overlapping the solid to fluid layer. It uses the hexahedron geometry for the mesh cells.

The cells overlapping the solid to fluid layer are cut by the geometry, which makes them more complex. The curved geometry is approximated by a set of polygons which vertexes are surface's intersection points with the cells' edges. These flat polygons cut the original hexahedron cells. This is illustrated in Figure 3.4.16.

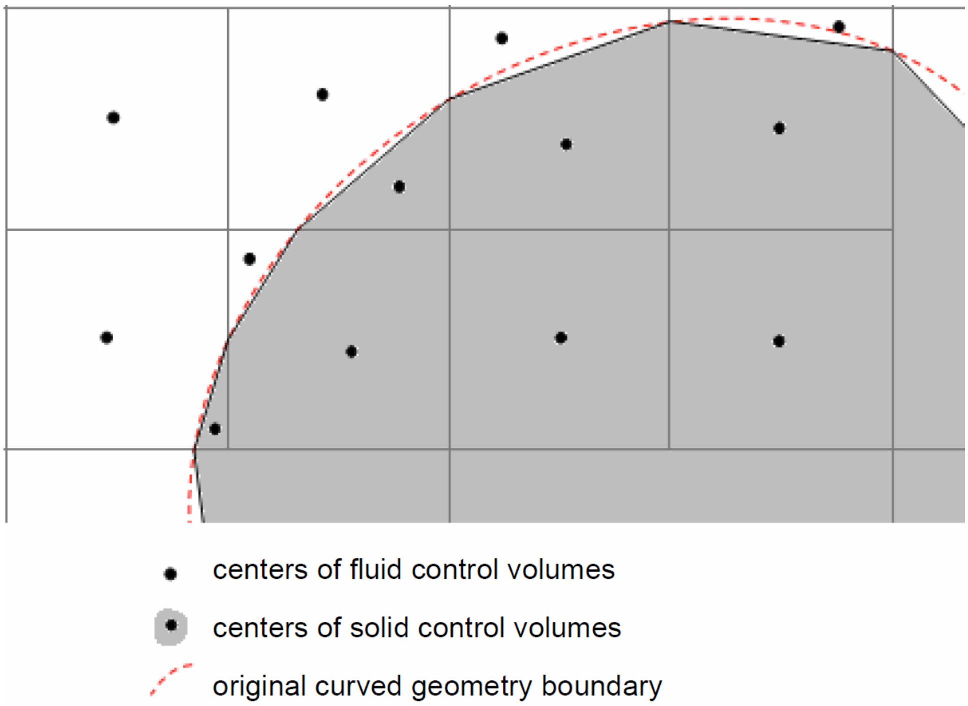

Figure 3.4.16 – Explanation of the fluid-solid interface mesh cells from [84].

First of all a basic mesh is generated, which does not depend on the fluid-solid interface. Then the basic mesh cells intersecting with the fluid-solid interface are split uniformly into smaller cells to capture the interface with mesh cells with the specified size. Next the mesh obtained is further refined in accordance with the fluid-solid interface curvature. The maximum angle between the normal to the surface inside one cell should not exceed a certain threshold, otherwise it is further refined. Finally the mesh obtained is further refined to satisfy the so-called *narrow channel criterion*. For each cell lying in the solid-fluid interface, the number of mesh cells lying in the fluid region along the normal must not be less than the criterion value. As a result of these meshing procedure steps, a locally refined rectangular computational mesh is obtained. The clarification of the mesh cell anatomy is illustrated in Figure 3.4.17.

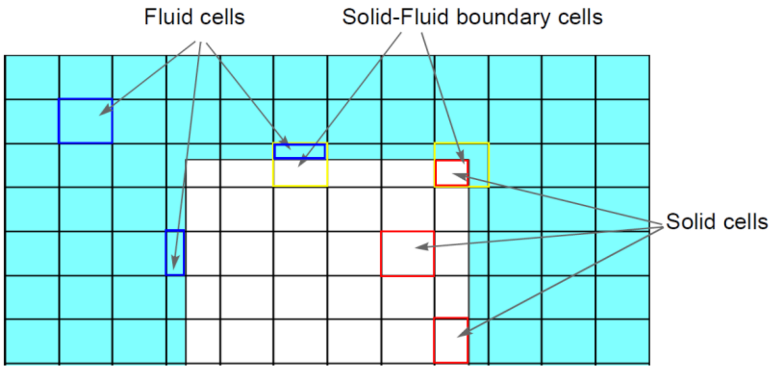

Figure 3.4.17 – Explanation of the anatomy of the mesh cells from [84].

The FloEFD solver makes use of the cell-centered finite volume (FV) method to obtain conservative approximations of the governing equations on the locally refined grid that consist of parallelepipeds and more complex polyhedrons near boundary. Following the FV method, the governing equations are integrated over a control volume, in this case the mesh cell, and then are approximated. All basic variables are referred to mass centers of control volumes. These cell-centered values are used for approximations.

The integral conservation laws may be represented in the form of the cell volume and surface integral equation.

$$\frac{\partial}{\partial t}\int \mathrm{b}U\,\mathrm{dv} + \oint \mathrm{b}F\cdot \mathrm{ds} = \int \mathrm{b}Q\,\mathrm{dv} \tag{57}$$

In discrete form

$$\frac{\partial}{\partial t}(Uv) + \sum_{\text{cell faces}} F\cdot S = Qv \tag{58}$$

The fluxes F are approximated in accordance with a type of the related faces. The faces are classified and divided into two groups in accordance with their properties: if they are axis-oriented and common for two adjacent control volumes, or they are arbitrary oriented boundary faces. Approximation are constructed in different ways for these two cases.

4

Equipment design methodology

The design of the cost-effective and compact combustion air preheating system for this application has its limitations in dimensions and should be able to meet the required performance. These limitations and the required performance can have an influence on some of the design choices and therefore exclude certain solutions to the questions; What type of shape will the casing be and what are the dimensions, what is the airflow rate and to what temperature can the air be heated, what type of heating elements can be used, what is the amount of pressure drop that is allowed? The limitations, boundary conditions and requirements will be discussed in this chapter. They will help with making the right design choices based on the calculations using the correlations. First, in the basis of design, the properties of the combustion air will be discussed, followed by the type of heating elements, casing dimensions and tube bank specifications. At the end of this chapter a working procedure for the design process will be given. The results out of the correlation calculations is discussed in [7 Equipment design].

4.1. Basis of design

This paragraph describes the principles, assumptions and the basis for the calculations required for the design of the electric combustion air preheater. As discussed in [3.1 Heat transfer & pressure drop in tube banks] the VDI method is used for the correlation calculations.

Combustion air properties

A certain amount of combustion air is needed for the combustion process, which is dependent on the size of the burner and fuel flow rate. For this study, a 2 MW burner is used. The combustion air will enter the heater at ambient temperature and pressure, and the preheater should be able to heat up the air to a temperature of at least 300°C. The physical properties of the combustion air entering the preheater can vary a bit since it is location and climate-dependent.

The combustion air preheater will also imply a pressure drop in the airflow. The pressure drop should be minimized to keep the size and electricity consumption of the fan as low as possible and also to not disturb the performance of the burner and fired heater. The operation parameters of the burner and fired heater are based on a certain pressure drop range through the whole system. For now, a maximum limit for the pressure drop implied by the preheater is set. All parameters are provided in Table 4.1.1.

Table 4.1.1 – The combustion air properties and additional parameters.

Temperature inlet	20	°C	Burner capacity	2	MW
Temperature outlet	300	°C	Air mass flow	0.691	kg/s
Max pressure drop	200	Pa	Duty ECAP	197	kW

Heating elements

A choice has to be made between the three different types of heating elements available for this application. The below limitations apply for the combustion air preheater according to Technip Energies [18], namely:

- Minimal gap spacing of 5 mm between all elements (prevent fouling)
- Minimal investments and low maintenance costs
- Compact design and easy to manufacture

Applying a minimal spacing of 5 mm between everything and preventing the system from fouling will make the open-coil heating elements a less suitable option. Therefore they are left out of consideration in the following chapters and the choice for the heating elements will therefore be between tubular and finned tubular heating elements. Both types of heating elements consist of a bare tube with the same specifications. The finned tubes have extra fins to increase the air-side heat transfer. This results in a higher price per tube meter but also reduces the bare tube surface area needed. The cost of the heating elements will depend on the length, the simplicity of the shape and the material.

The type of material used for the heating elements is of great importance. There are several types of material that are used for the sheath of the electric tubular heating elements. These materials are listed in Table 4.1.2 with its maximum operating temperature and typical watt densities given from [85], [86]. These values are confirmed by other manufacturers [40], [87]. The elements need to be corrosion resistant, applicable for high temperatures and should be able to cope with high watt densities. Therefore the preferred material would be Stainless steel 304 or 316 or Alloy 800. A tube sheath temperature of 650°C will be used for the calculations.

Table 4.1.2 – Types of material and their properties that can be used for the sheath of the tubular heating elements from [85].

Sheath material	**Max. Operating temperature [°C]**	**Typical watt density [W/cm²]**
Steel	400	6.9
Stainless steel (304 or 316)	650	9.3
Alloy 800	870	9.3
Alloy 600	982	6.9

Casing shape and dimension

The casing shape and dimension of the ECAP are of great importance for the performance and further design of the heating elements. The combustion air is supplied to the burner via an air duct that could be cylindrical or rectangular, meaning that it is not of importance of the design choice on the shape of the casing. Both option, rectangular or round have their pros and cons, but a round casing air heater can be more complex during the calculations and production of the system. The two casing options are given in Figure 4.1.18. Both shapes are compared in [6.1 Fluid properties and casing dimensions] and the optimal dimensions of the casing are also discussed.

The casing also needs to be isolated, it should be able to cope with a temperature of 300°C and it must be corrosion resistant. The more heat can be kept inside and doesn't leak to the environment, the more efficient the combustion air preheater becomes.

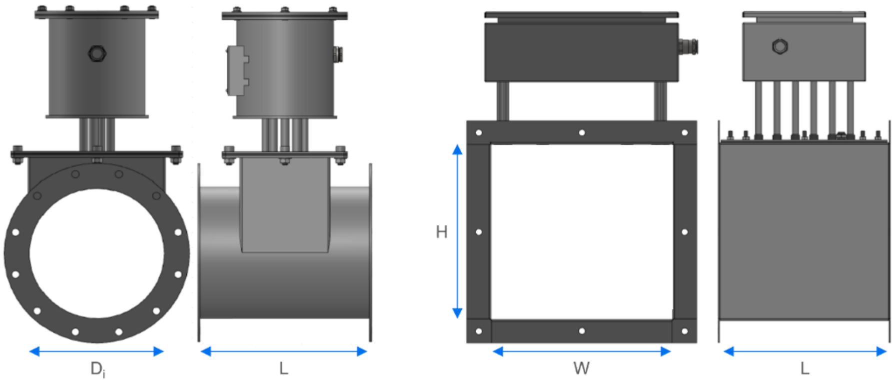

Figure 4.1.18 - Casing options for the combustion air preheater.

Comparison of calculation methods

As discussed previously, there are some differences in the calculation methods for a bare tube bank. There are differences in the input data needed, the temperature used for physical properties and the Reynolds number calculation.

Comparing these methods, the VDI method is the most suitable method for this specific calculation because of its requirements for the information to be known. The HTFS method requires a fixed-length input for the tube bank, but this is the parameter that needs to be minimized for a compact design. The BHaMT method is excluded from now on because it is an alternative to the Gnielinski method that is used in VDI method. The BHaMT book recommends using this Gnielinski method if possible, instead of the alternative provided in the book. After the initial design is determined using the VDI method, a CFD model will be made so that the outcome of the correlations can be confirmed by a different method.

Cost estimation

The capital costs of the ECAP can be estimated using the Lang factor [88], [89] at the end of the design procedure when the system parameters are determined. The Lang factor is an estimated ratio of the total cost of creating a new process within a petrochemical plant, to the costs of only the major technical components. It includes the material costs, installation, construction and engineering costs of the process. The Lang factor is usually around 5 and its accuracy is estimated to be within 35%.

The CAPEX of the ECAP is confidential information, so a fictitious number is chosen, which is 10.000 euro. The estimated costs for the engineering, material, construction and installation of the ECAP are 50.000 euro.

Summary

Burner capacity	2	MW
Fuel gas	Natural gas	-
Combustion air flow	0.691	Kg/s
Ambient pressure	1.013	bar
Ambient temperature	20	°C
Temperature inlet	20	°C
Temperature outlet	300	°C
Temperature tube sheath	650	°C
Air duct diameter	320	mm
Minimal gap spacing	5	mm
Maximum casing length	1000	mm
Duty ECAP	~ 200	kW
Maximum pressure drop	200	Pa
Heat transfer correlation	VDI method	-
Lang factor	5	-

4.2. Design procedure

This paragraph provides the design procedure that is used for the design of the electric combustion air preheater. A procedure similar to the procedure suggested by [Sinott & Towler] is used. The results out of the correlation calculations are provided and discussed in chapter [Equipment design results] and the outcome of the CFD model is provided at the end of this report in chapter [CFD modelling].

Step 1:
Define the duty, this is important for the calculation of the amount of heat that needs to be released by the heating elements. Calculate and define the fluid flow rate and in- and outlet temperatures. Define the heating elements sheath temperature and the shape and preferred dimensions of the casing.

Step 2:
Collect the fluid physical properties required: density, kinematic viscosity, specific heat coefficient and thermal conductivity. These properties are extracted out of the software “REFPROP” [90] for the given temperature and pressure.

Step 3:
Decide type of heating elements, tube diameter and pitches, tube lay-out and materials used for the heating elements. Try to limit the by-passing and extract the highest performance out of a single heating element.

Step 4:
Calculate single tube area and number of tubes needed. The wall heat flux can be calculated and should be within the limits of the material. The number of tube rows should be minimized by maximizing the performance of a single heating element and optimization of the spatial arrangement.

Step 5:
Calculate air-side heat transfer coefficient. This can be calculated using the correlations discussed in [3.1 Heat transfer & pressure drop in tube banks] by using the Nusselt number.

Step 6:
Calculate air-side pressure drop implied by the tube bank. Again using the correlations discussed in [3.1 Heat transfer & pressure drop in tube banks].

Step 7:
If the requirements are not met, start over from step 3. If they are met tune and optimize for the most suitable outcome and continue with step 8.

Step 8:
Estimate the capital (and operating) costs of the preheater

Step 9:
Carry out detailed simulation of the specific geometry to confirm that the heat transfer coefficients and pressure drops that have been assumed are realistic. This step is carried out using a commercial CFD program.

5

Burner test methodology

To investigate the influence of the combustion air preheating system on the burner and fired heater performance and the GHG emissions, an experiment has been performed. This experiment has been performed at the Technip test facility using a 2 MW LSV® burner. First a hypothesis will be formulated, followed by the equipment used during the experiment. At the end the test procedure will be discussed.

5.1. Hypothesis

In this paragraph the necessity of the experiments will be discussed and a hypothesis will be formed. Figures of merit are the heat flux profile of the fired heater and the flue gas composition. Various temperatures, pressures, flow rates and gas concentrations will be measured, and these parameters will most likely vary between the test runs.

The goal of this experiment is to provide insight into the influence of combustion air preheat temperature on the NO_x emissions and heat flux profile for this specific test fired heater. Correlations are available to calculate the NO_x emissions, but they are not valid for fired heater operations with varying combustion air temperature. This experiment should help to draw a conclusion about the added value of the combustion air preheater by providing information about the emissions and heat flux profile changes.

Hypothesis

It is expected that the increase in combustion air temperature has a minor influence on the heat flux profile. For the NO_x emissions, it is expected that this will increase, since the flame temperature will also increase due to the higher combustion air temperature.

5.2. Experimental setup

The experimental fired heater setup consists out of the firebox with radiative coils, the LSV® burner, the fuel supply skid and different types of measurement equipment. All of them will be discussed briefly in this paragraph.

The Large Scale Vortex (LSV®) burner [35] [13] used during this experiment was developed in 2003 to match the demand and expectations from clients and regulators. They wanted larger capacity, greater reliability and lower costs together with higher efficiency and lower emissions of pollutants like carbon monoxide and nitrogen oxides. Field results confirm the ultra-low NO_x emissions, uniform flame heat release profile and trouble-free plant operations.

It can be applied to different process heating applications like ethylene cracking fired heaters or steam methane reformers, and it can be used in different air supply modes (natural draft, induced draft and forced draft) with ambient or preheated combustion air. It is also suitable for a wide range of fuel gas compositions and firing configurations, and it can be placed on the floor (bottom-firing) or on the roof (top firing) of a firebox. The burner can also be applied to retrofit projects, replacing existing burners.

The LSV® burner consists of a metal burner assembly, a metal flange and a refractory tile. The burner assembly has two types of openings: one large port for the central device and eight or ten small ports for fuel staging lances. The central device stabilizes the vortex ring flame by anchoring inside the central cavity resulting in stable conditions at extremely fuel-lean firing conditions. A small part of the fuel will be used by this vortex ring flame and most of the fuel will be routed to the staging tips. This stable vortex ring flame is held in the stagnant region and is able to attach the main flame to the burner. The vortex ring flame and fuel staging tips are highlighted in figure X, which was taken during the experiments. Figure X illustrates the formation of the vortex ring flame, from which the name of the Large Scale Vortex (LSV®) burner originates from.

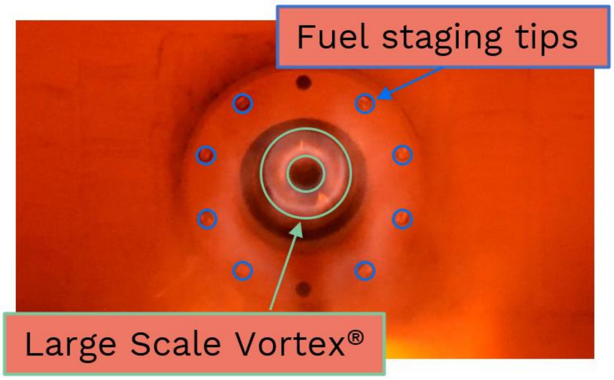

Figure 5.2.19 - A picture taken during the experiments to illustrate the vortex ring flame and staging tips.

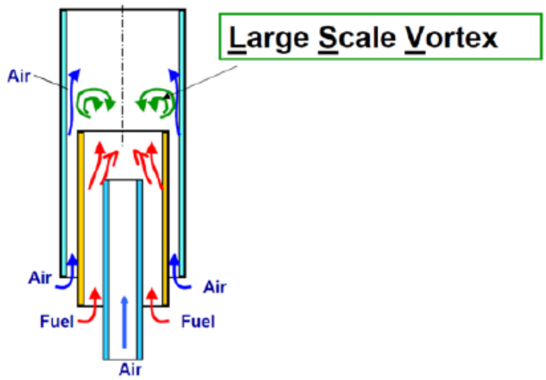

Figure 5.2.20 – The central device assembly that results in the formation of the vortex ring flame.

The location of the test fired heater is at the Technip test facility at Plant One in the Port of Rotterdam, and the test fired heater is illustrated in Figure X. A LSV® burner configured for cracking fired heaters fires inside a 40-foot container with refractory inside. The flames of a cracking fired heater configured LSV® burner has a typical flame length of 4-8 meters and uses 8 asymmetrical patterned staging tips which can have a drilling angle between 0 and 10 degrees inward. Air-cooled radiative coils are installed in the top part of the fired heater for heat flux measurements and it has a balanced draught system.

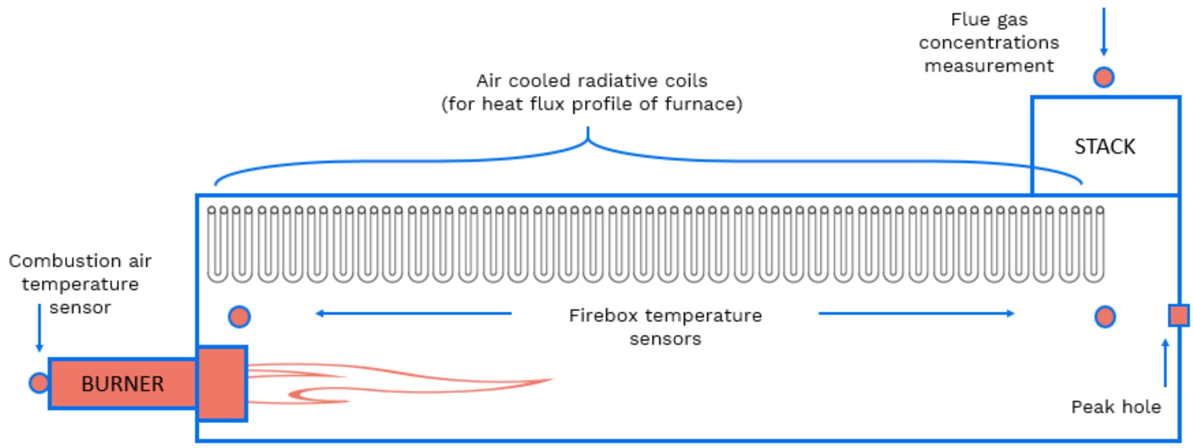

Figure 5.2.21 - Setup of the test fired heater.

Measurement equipment

Measurement equipment is available for logging the O2, CO and NO_x concentration in the flue gases, the heat flux for the 36 air-cooled tubes, the firebox temperature at fixed locations, the combustion air temperature, the fuel and airflow and the pressure. An experiment will be conducted to measure the heat flux, temperatures, mass flows, and NO_x and CO emissions for a specific range of combustion air preheat temperatures. The operating costs savings and CO_2 emissions reduction will be calculated during the aftermath.

The heat flux of the 36 air-cooled tubes inside the fired heater is measured using temperature sensors on each tube. They are also used to check whether the system has reached a steady-state. The firebox temperature is measured at 2 location, at the burner and at the stack, and the combustion air temperature is measured at the front of the burner.

The fuel flow is measured using gas flow meters, and the pressure of the fuel and air is measured at the inlet at the burner and at the stack. The gas concentrations of the flue gases of O2, CO, NO and NO2 are measured using an ECOM J2KN-PRO gas analyzer. The airflow is calculated using the fuel flow and the O2 content in the flue gasses. All measurement equipment is listed in Table 5.2.3 with its range and product number, and they are calibrated at the factory by the supplier.

Table 5.2.3 - Specifications of the measurement equipment used during the experiment.

Measurement	**Amount + Type**	**Range**	**Accuracy**
Air cooled tubes			
Firebox temperature	2x OMEGA HH-801B	-40 – 1200°C	0.1% rdg + 1°C
Combustion air temperature	OMEGA HH-801B	-40 – 1200°C	0.1% rdg + 1°C
Fuel flow	Multiple different types of BROOKS INSTRUMENT MT3809-XXX	5 – 480 Nm^3/hr	
Air pressure	2x DWYER MARK II	0 – 80 mmWC	
Flue gas concentrations	ECOM J2KN-PRO	vol% / ppmv dry	5% rdg

5.3. Test procedure

All measurements are performed on the same day without shut down of the fired heater between the runs in December 2020. The LSV® burner shown in figure X has two different valve positions, i.e. operation modus, the Start-Up modus (SU) and Low- NO_x modus (LN). The start-up modus is used during the start-up of the burner to heat up the fired heater to a temperature above 750°C, so that the Low-NO_x modus can be activated. During the test runs it is also necessary to keep the oxygen percentage at the flue gases constant since this has a significant influence on the NO_x formation in the firebox.

Since the combustion air preheater designed during this study is not yet manufactured, another air heating method is used to test the influence of the combustion air temperature on the burner and fired heater performance. The required air preheat temperature can be accomplished by using the heated air from the air-cooled radiative coils. The heated air is rerouted and inserted at the combustion air inlet. Since the heated air from the radiative coils is mixed with the ambient air entering at the air inlet, a lower temperature will be achieved for the combustion air. The combustion air temperature will range from ambient temperature to the maximum temperature possible during the tests.

Table 5.3.4 - Logging template for the test results.

Test nr.	1	2	3	4	5	6	7	8
Burner firing mode	SU	SU	SU	SU	LN	LN	LN	LN
APH temperature (°C)	0	100	200	300	0	100	200	300
Coil temperatures (in file)	.xls	.xls	.xls	.xls	.xls	.xls	.xls	.xls
Firebox temp. (°C) @ burner								
Firebox temp. (°C) @ stack								
O2 (vol% dry)								
CO (ppmv dry)								
NO (ppmv dry) NO2 (pmmv dry)								

6

Equipment design results

This result for the design of the combustion air preheater using the correlation calculations are provided and discussed in this chapter. First step 1 and 2 of the design procedure are discussed followed by the decision on casing shape and dimensions. Step 3-8 are discussed next, in which the heating element design and tube bank lay-out is chosen. At the end the air-side heat transfer coefficient and pressure drop for the final design are provided. This design will be used for a detailed simulations using CFD.

6.1. Fluid properties and casing dimensions

The first steps of the design procedure are discussed in this paragraph. For heating up the air from ambient temperature to 300°C, a duty of 200 kW is required. The air mass flow through the system is 0.697 kg/s, derived from the combustion capacity of the 2MW LSV® burner. Heating up the air changes its density, resulting in an increasing velocity throughout the system, see Figure 6.1.22. This is of great importance for the calculation of the heat transfer and pressure drop. The conductivity, kinematic viscosity and specific heat coefficient also changes with temperature. All fluid properties are implemented into the calculations using "REFPROP" [90], which is the NIST Reference Fluid Thermodynamic and Transport Properties Database.

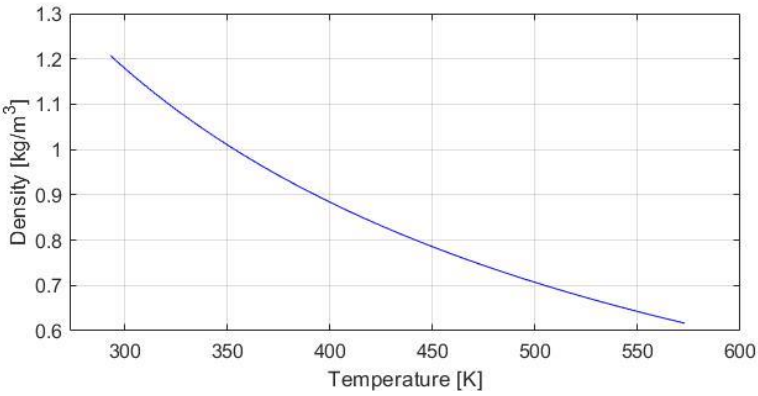

Figure 6.1.22 – Air density versus temperature.

The shape of the casing, round or rectangular, has a significant impact on the performance, costs and accuracy of the calculations. The size of the cross-sectional area is important for the flow velocity, therefore also for the heat transfer and pressure drop. A higher velocity results in a higher heat transfer, but also a higher pressure drop. By setting a maximum for the pressure drop, a cross-sectional area can be derived. Correlations used for tube banks are derived from straight tube bank experiments and will be more accurate for the square heater compared to the cylindrical heater. If a cylindrical casing is used, the shape heating elements must also become circular.

With the maximum allowable pressure drop set at 200 Pa (20 mm WC), a solution using a cylinder with the same diameter as the burner inlet is not feasible since the implied pressure drop of the bare tube bank would be above 1000 Pa according to the calculations. The significantly smaller cross-sectional area of a circle compared to a square resulted in a too high velocity. A square-shaped casing is therefore the preferred option. Using a square casing instead of a cylindrical casing is also beneficial for the cost of the heating elements, since this will depend on the length, the simplicity of the shape and the materials used.

Size of the casing

Now the shape of the casing is determined, the ideal dimensions of the casing can be derived out of the calculations. With the maximum allowable pressure drop set at 200 Pa, the minimum cross-sectional area of the square air heater can be determined using the calculation for the pressure drop for tube banks. The outcome is displayed in Figure 6.1.23, and this indicates that the ideal cross-sectional area would be around 0.16 m^2, i.e. a duct with a width (W) and height (H) of 0.4 m approximately.

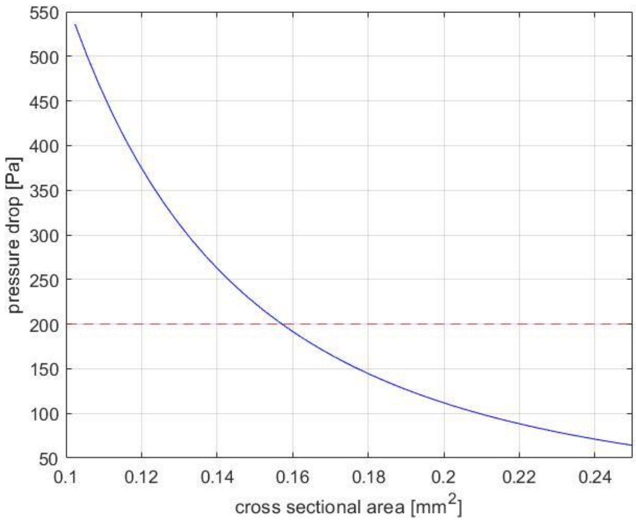

Figure 6.1.23 - Pressure drop versus cross-sectional area for a finned tube bank with square casing.

The size of the air heater using a square casing is not only dependent on the number of tube bank rows and the tube pitch in the longitudinal direction, but also on the flanges to connect the cylindrical air duct to the square casing. The minimum angles for the flanges at an inlet and outlet are 30° and 45°, respectively [18].

The minimum cross-sectional area for the casing of the combustion air preheater that can heat up the air to a temperature of 300°C with a maximum allowable pressure drop is 0.16 m^2, i.e. 0.4 width (W) and height (H) for a square. The transition flanges from the air duct to the square casing are designed in such a way that they have a maximum angle of 30° at the inlet (α) and 45° at the outlet (β). The side view of the casing with the flanges is displayed in with the lengths provided in the figure.

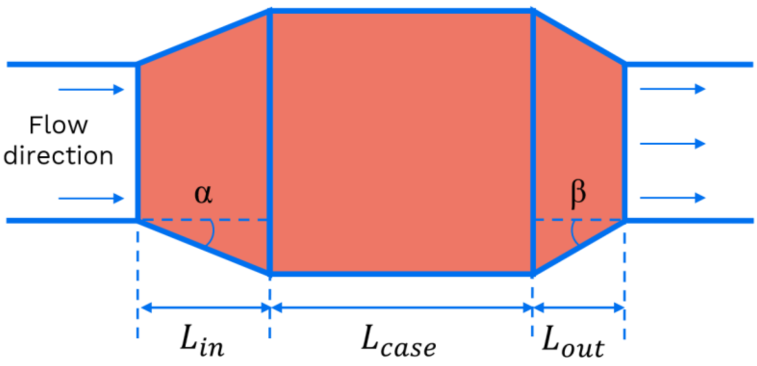

Figure 6.1.24 – The side view of the casing with flanges showing the flange angles and lengths.

6.2. Heating elements and tube bank specifications

This paragraph provides the design details for the tube bank.. This is done by executing the design steps 3 to 8 of the design procedure. The results of the calculations using the correlation provided by the VDI method are provided and discussed. First, the type of heating element will be determined, followed by the outer tube diameter, tube pitches, fin specifications and tube lay-out.

Tubular vs finned tubular

As discussed in [4.1 Basis of design] is the heat transfer performance of the bare tubular heating elements and finned tubular heating elements compared. A gap spacing of 5 mm between every component is required to prevent fouling. This requirement results in a minimum spacing of 5 mm between every fin for the finned tubular heating elements. For the comparison of the bare tube vs finned tube, a circular straight fin is used with the specifications as given in Table 6.2.1.

Table 6.2.1 - Comparison of a bare tube and a finned tube bank.

Fin spacing	5	mm
Fin height	5	mm
Fin width	1	mm

	Bare tube	Finned tube	
$\overline{Nu}_{Bundle}$	38.0	26.6	-
Required bare surface area			m^2
Heat flux	9.7	6.1	W/cm^2
Number of rows	17	9	-

As can be concluded out of the calculation results provided in Table 6.2.1, is the heat transferred per area lower for finned tubular heating elements, but the area is increased significantly. Therefore fewer rows of tubes are needed, a factor of 2 compared to the bare tubular heating elements. From these calculations and the results provided in Table 6.2.1 can be concluded that while maintaining a gap spacing of 5 mm, a finned tubular heating element is preferred over the bare tube heating element since it would result in significantly less required bare tube heat transfer surface, i.e. more compact design.

Tube bank specifications

Now that the preferred casing properties and the type of heating element are determined, an optimal configuration of the finned tubular heating elements can be derived. Two important parameters to analyse the performance are the heat flux and pressure drop. The heat flux and the pressure drop for different finned tube outer diameters are given in Figure 6.2.25. As expected from the calculations, a smaller tube diameter provides a higher heat flux. Therefore the tube diameter should be minimized within the design limitations. The tube diameter is limited by its mechanical strength, its sensitivity to vibrations, the resistance wire inside the tubular heating element and the availability at manufacturers. The latter is for this specific application the limiting factor. In practice the tube outside diameter shall be at least 8 mm.

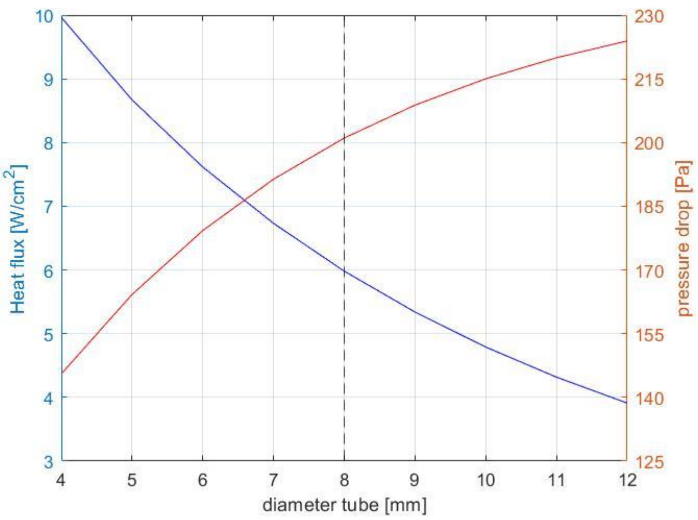

Figure 6.2.25 - The heat flux per row and pressure drop of the system for varying tube diameter with fin height 5 mm.

Besides the tube diameter, also both longitudinal and tangent tube pitches, S_y and S_x respectively, have an impact on the flow characteristics, heat transfer and pressure drop. Figure 6.2.26 provides the heat flux and pressure drop of the variable transverse tube pitch ratio with a constant tube diameter of 8 mm for a square duct heater. There seems to be an optimum in the pitch ratio tangent to the flow direction around 2.9, most probably due to an increasing velocity at lower pitch ratios. The increase at higher pitch ratios is caused by an increase in tube rows and length of the tube bank.

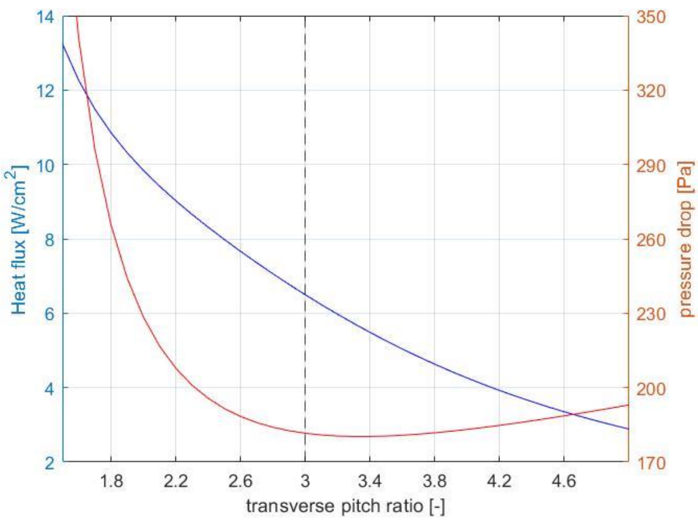

Figure 6.2.26 - Graph showing the pressure drop of the system for varying transverse pitch ratio.

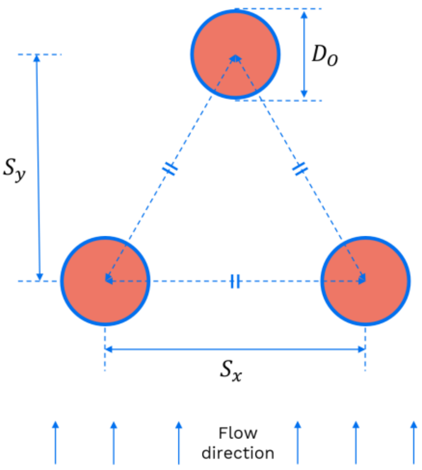

Figure 6.2.27 – A schematic overview of the tube lay-out.

Another limitation of the transverse pitch ratio (S_x/D_o) of the tubes is the manufacturing of the heating elements. The heating elements will be bend multiple times, so that one heating element can cover the whole cross sectional area, while maintaining the minimal spacing of 5 mm between each tube. This results in a lay-out of one heating element as illustrated in Figure 6.2.28 with the transverse pitch S_x and bending radius illustrated in Figure 6.2.29. The minimum bending radius (R_{bend}) of these tubes is limited due to the coiled wire and magnesium oxide powder inside these elements. From multiple heating element producers a minimum bending radius of 1.5 times the tube diameter (in factory) is accomplished, to produce tubular heating elements without failures [40], [85]. Therefore the minimum transverse tube pitch ratio R_x for this design will be 3, resulting in a transverse pitch S_x of 24 mm.

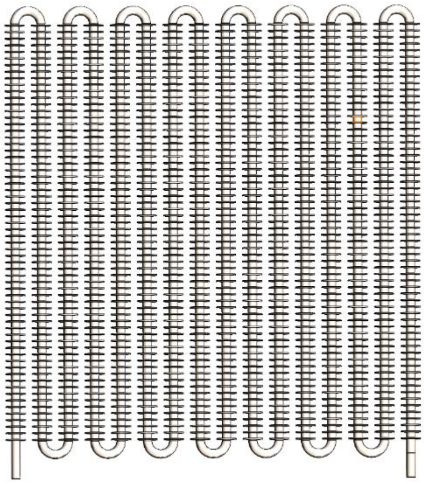

Figure 6.2.28 – single tube lay-out of one heating element.

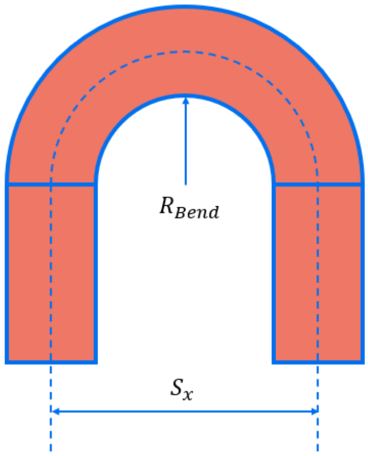

Figure 6.2.29 - The transverse tube pitch and bending radius graphically illustrated.

As expected from the calculations, a small as possible longitudinal pitch of the tubes should be used in the flow direction, minimizing the length of the bank and the pressure drop. The limitation for the longitudinal pitch ratio is the tube pitch in the transverse direction, since using a smaller tube pitch in longitudinal direction compared with the transverse direction would result in a higher velocity, i.e. pressure drop, due to a smaller gap in that direction. This results in a minimum longitudinal pitch ratio R_y of 2.6 when using a pitch ratio of 3 in the transverse direction, because that would result in an triangular pitch between the tubes, as illustrated in Figure 6.2.27. Due to practical reasons this is also beneficial, since this maintains the same bending radius is all direction.

Fin specifications

For the comparison of the tubular vs finned tubular heating elements, a guess of the actual fin specifications was used, but these specifications also have a significant influence on the performance of the combustion air preheater. As stated, does the spacing of the fins S_f needs to be at least 5 mm to prevent fouling, resulting in a fin pitch S_f of 6 mm. Using the longitudinal and tangent tube pitch ratios of 3 and 2.6 respectively, results in a maximum fin height h_f of 5 mm, to keep a minimum spacing between the tubes of 5 mm. The only variable parameters of the fins are the fin width w_f and shape. These parameters are illustrated in Figure 6.2.31. Figure 6.2.30 provides the heat flux and pressure drop of the variable fin width for a straight fin with a height of 5 mm, a fin pitch of 6 mm. The tube diameter is again kept constant at 8 mm for a square duct heater.

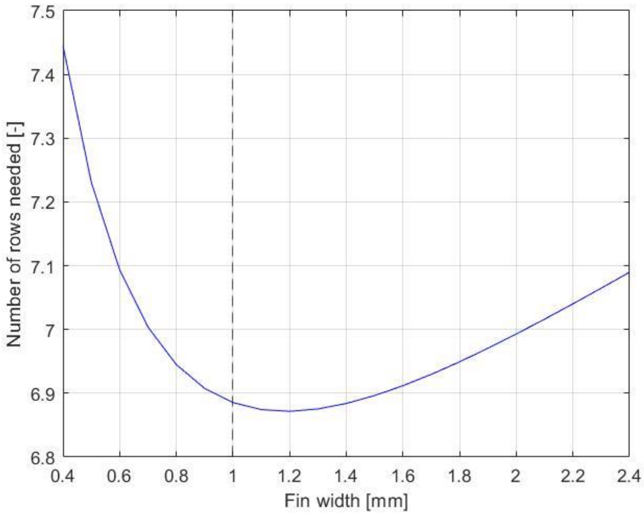

Figure 6.2.30 – Graph showing the number of rows needed for a varying fin width.

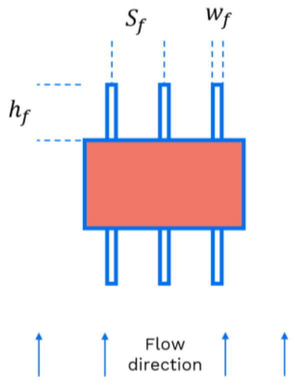

Figure 6.2.31 – A schematic overview of the finned tube lay-out.

There seems to be an optimum for the fin width at 1.2 mm, but there seems to be not much of a difference between 0.8 and 1.8 mm. The fin width also contributes to the weight and price of the finned tubular heating element, and a smaller fin width results in more fins per length, i.e. more heat transfer area per length. Therefore a smaller width of the fin has the preference and a width of 1.0 mm is chosen.

6.3. Final design

This chapter provides the results and the reasoning behind the results for the design of the ECAP, heating the air to a temperature of 300°C. According to the VDI method, that is used to calculate the heat transfer and pressure drop of the ECAP, a casing having a cross-sectional area of 0.16 m^2 is preferred to maintain a pressure drop lower than 200 Pa. This cross sectional area is the basis for the design specifications that are calculated in the steps after, such as the bare tube heat transfer area needed.

If the design should be able to heat up the air to a higher temperature, a larger cross sectional area is needed. With a larger cross-sectional area, extra rows of tubes can be installed. This results in a less compact design, but with a larger operating range.

The design specifications derived out of the calculations for the ECAP that can heat up the air to a temperature of 300°C are given in Table 6.3.1. A render of this tube bank together with the in- and outlet flanges are given in Figure 6.3.32 and Figure 6.3.33. For a combustion air preheater that can heat up the air to a temperature of 500°C, the design specifications are given in Appendix B.

Table 6.3.1 - The initial design specifications.

Inside width casing	0.396	m
Inside height casing	0.396	m
Outside diameter tube	8	mm
Pitch ratio longitudinal	2.598	-
Pitch ratio transverse	3	-
Fin spacing	5	mm
Fin height	5	mm
Fin width	1	mm

Temperature inlet	20	°C
Temperature outlet	300	°C
Temperature tubes	650	°C
Duty		kW
Air mass flow	0.691	kg/s
Inlet velocity bank	3.65	m/s
Outlet velocity bank	7.15	m/s

$\overline{Nu}_{Bundle}$	26.7	-
Heat flux	6.0	W/cm²
Average heat flux	5.1	W/cm²
Heat transfer coefficient	103	W/K·m²
Number of rows	7	-
Tube bank length	140	mm
Total length (with flanges)	468	mm
Pressure drop	182	Pa

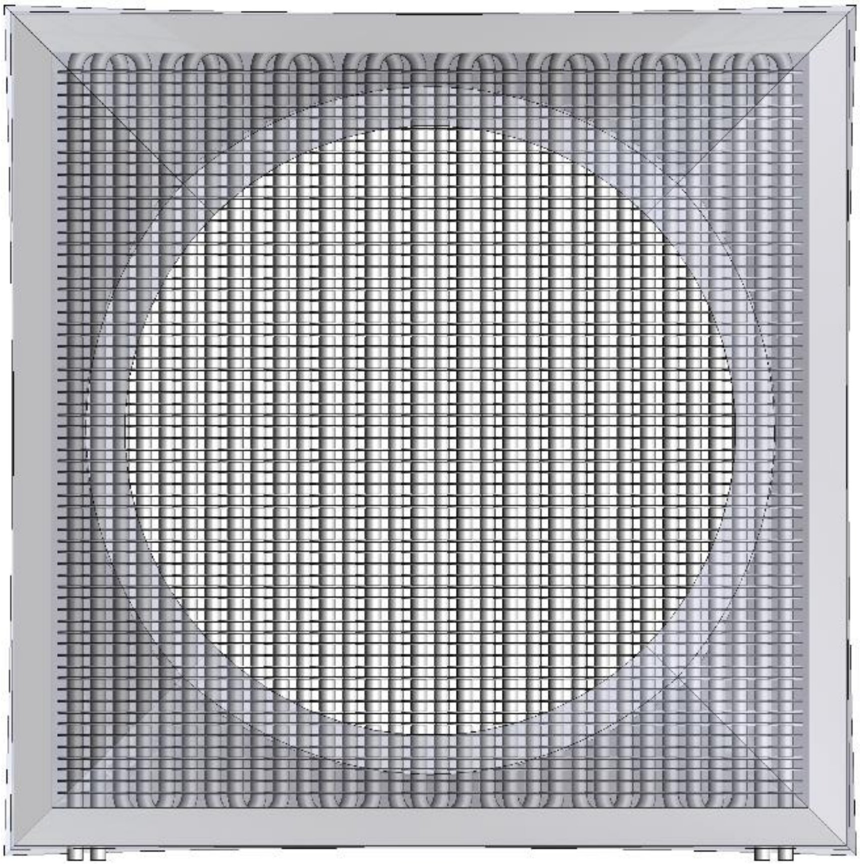

Figure 6.3.32 - A render of the tube bank top view.

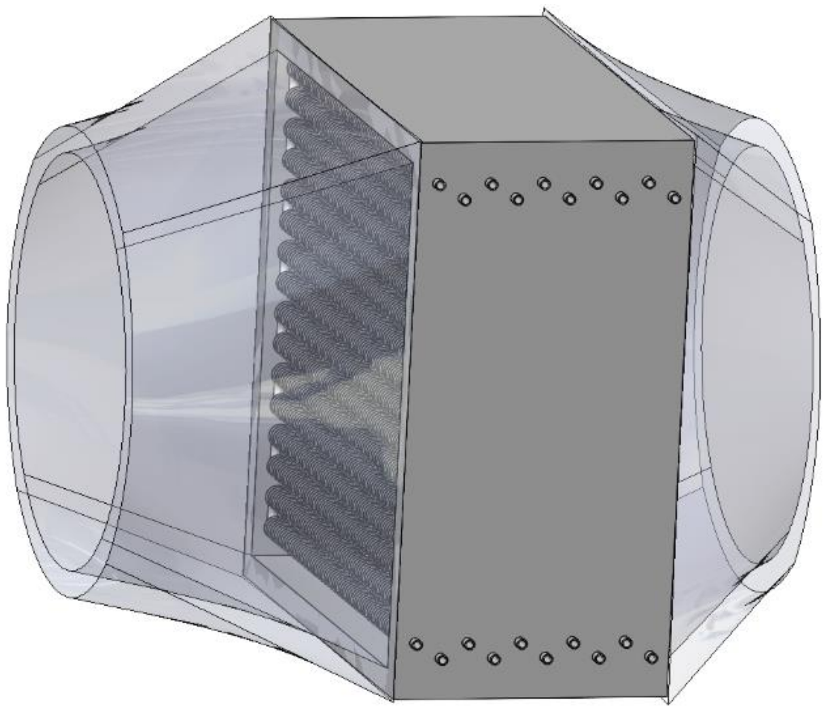

Figure 6.3.33 - A render of the tube bank together with its in- and outlet flanges.

6.4. CO_2 emissions reduction and cost savings

This paragraph will show and discuss the results originated out of calculations for the costs and CO_2 emissions based on multiple sources. These results are based on a constant amount of energy provided to the LSV® burner, meaning that amount of fuel used will decrease with increasing amount of electricity used. This is graphically shown in Figure 6.4.34. That is not the case during the experiments that were conducted. During the experiment the fuel input was kept constant, so the total energy input increased.

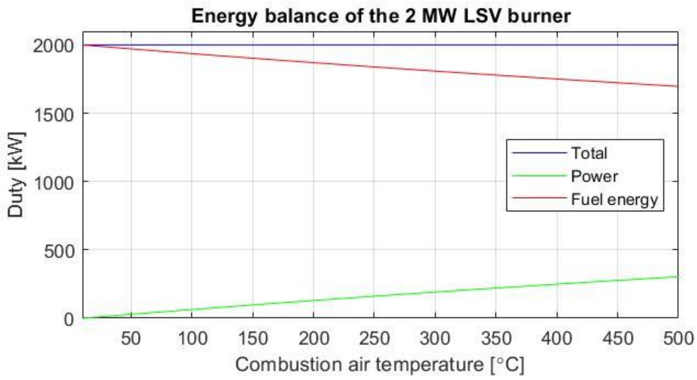

Figure 6.4.34 – Total heat released, combustion air preheat duty and fired heat versus combustion air temperature for the 2MW LSV® burner.

There are two scenarios that will be compared with the baseline condition of firing without electric combustion air preheating. One scenario uses the ECAP for 3000 hours per year, heating the combustion air to a temperature of 300°C, while the other scenario uses the ECAP for 3000 hours per year heating the combustion air to a temperature of 500°C. The amount of hours active cannot be increased, since for that amount of operating hours green certificates are available hence no CO_2 emissions for the electricity. This will slightly increase over the years, but is not taken into account in these results. For these two scenarios CO_2 emissions savings are graphically show in Figure 6.4.35.

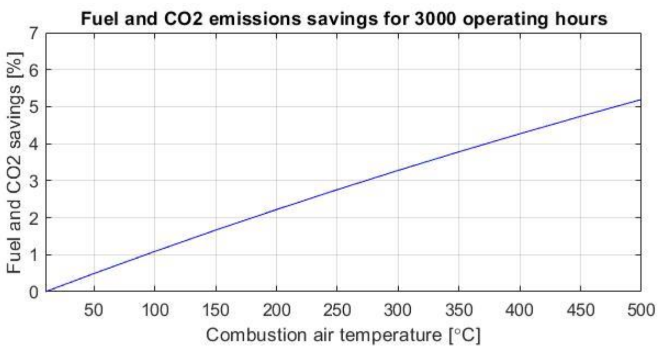

Figure 6.4.35 – Fuel and CO_2 emissions savings for varying combustion air temperature for the 2MW LSV® burner.

The forecast of the price for the emissions of a ton CO_2 equivalent is derived from the European Emissions Trade System (EU ETS) and the Dutch emissions taxes and a forecast is made by Technip as can be seen in Figure 2.1.4. The expected price for electricity for the industry during the coming decade for North-Western Europe is provided by [11], [12], [13]. It is kept at 20 euro per MWh for operation during the cheapest 3000 hours per year, since the exact price is difficult to forecast. The same can be said about the natural gas price, which is also kept constant. From this information is it possible to calculate the operating costs for different scenarios and the amount of CO_2 emissions for scope 1 and 2.

The CAPEX of the combustion air preheater is also calculated [18] using the Lange factor [88], [89]. For this report a fictional value for the CAPEX of 50.000 euro is used. The OPEX for the scenarios can be calculated using the prices for electricity, gas and CO_2 emissions. For simplification the prices for the electricity, gas and CO_2 emissions are chosen as given in Table 6.4.2 for the two scenarios compared to the baseline scenario. A profit curve has been made to estimate the pay-back time of the investment in an ECAP, see Figure 6.4.36.

Table 6.4.2 – The OPEX savings and CO_2 emissions savings for one 2MW LSV® burner. Calculated for the two scenarios in 2022 and 2030 using the parameters provided in the table.

	BL Scenario	**Scenario 1**	**Scenario 2**
APH temperature (°C)	-	300	500
Operating hours (hours)	-	3000	3000
Electricity price 3000 hrs (€/MWh)	-	20	20
Gas price (€/MWh)	20	20	20
CO_2 emissions 2022 (€/ton)	70	70	70
CO_2 emissions 2030 (€/ton)	140	140	140
OPEX savings 2022 (€/year)	-	7957	12612
OPEX savings 2030 (€/year)	-	18785	29775
CO_2 savings (ton/year)	-	114	180

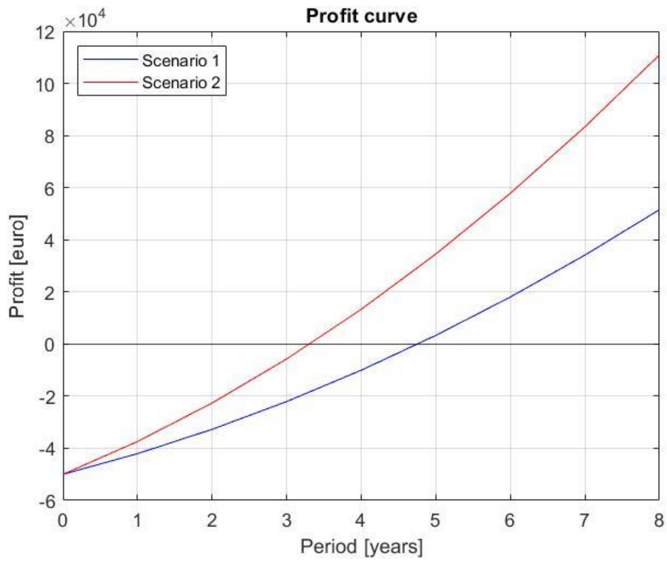

Figure 6.4.36 – A profit curve for the two scenarios for one 2MW LSV® burner.

7

Burner test results

The result of the measurements proposed in [Burner test methodology] are shown in the following paragraphs. The values obtained in the SU modus and LN modus are separated in the result for the heat flux profile and merged in the results for the NO_x emissions. 100% LN modus was not reached, due to the cold weather and low fired heater temperature. Normally a fired heater temperature of 750°C is needed to operate the LSV® burner in 100% LN modus. The results obtained for the LN modus are achieved operating in 75% LN modus. The tests were carried on December 10, 2020.

7.1. Heat flux profile

This paragraph will show and discuss the results originating from the temperature measurements of the 36 air-cooled radiative coils during the experiments. This will help to investigate the influence of the combustion air temperature on the burner and fired heater performance. Figure 7.1.37 shows the relative duty of each of the 36 air-cooled coils for different combustion air preheat temperatures for the LSV® burner firing in SU modus. Figure 7.1.38 shows the same for the 75% LN modus.

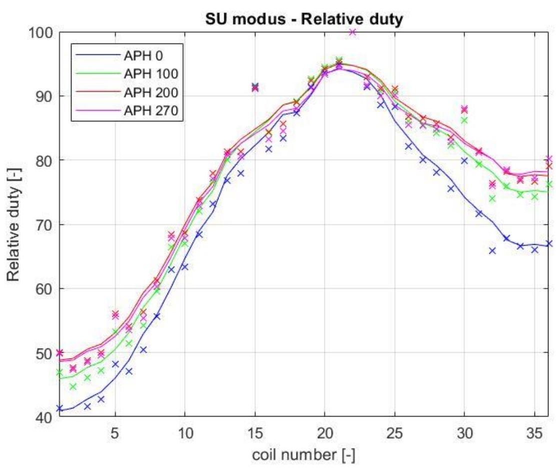

Figure 7.1.37 - Relative duty of the 36 air-cooled coils when firing the burner in SU modus.

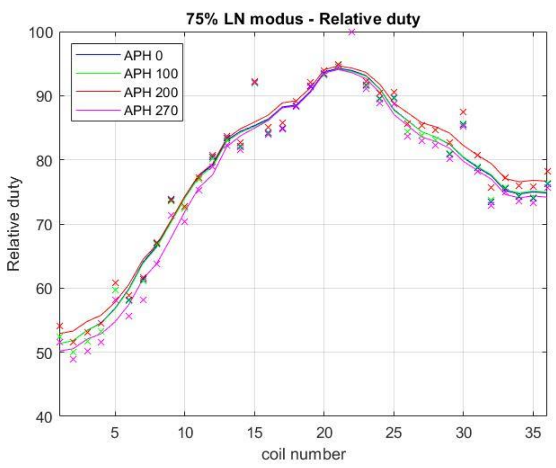

Figure 7.1.38 - Relative duty of the 36 air-cooled coils when firing the burner in 75% LN modus.

Both graphs in Figure 7.1.37 and Figure 7.1.38 show a peak duty between the 19th and 23rd coil that does not shift closer to or further away from the burner. That suggests that the area in the firebox with the highest heat flux does not move and the flame length does not change. Figure 7.1.37 also shows flatter curves of the duty with increasing combustion air temperature. That could be a result of the increasing combustion air temperature, which should result in an increase of firebox temperature while keeping a constant fuel flow rate. This will be discussed further below. Figure 7.1.38 shows the same shape of the curve, or at least not a significant change in curve shape. That would suggest that the combustion air preheat temperature in low NO_x modus has little to no influence on the heat flux profile.

To find a clarification for why the shape of the curve in Figure 7.1.37 changes, another graph is shown. Figure 7.1.39 shows the air outlet temperature for each of the 36 air-cooled radiative coils for different combustion air preheat temperatures for the LSV® burner firing in SU modus.

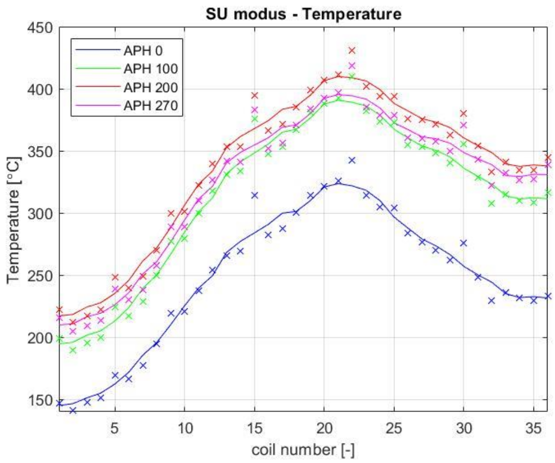

Figure 7.1.39 – Air outlet temperature of the 36 air-cooled coils when firing the burner in SU modus.

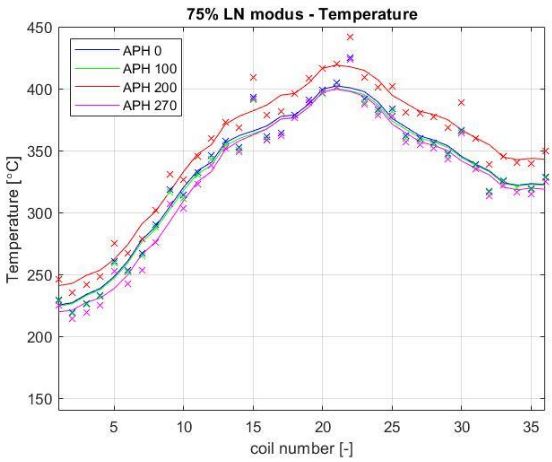

Figure 7.1.40 – Air outlet temperature of the 36 air-cooled coils when firing the burner in 75% LN modus.

The left graph in Figure 7.1.39 shows that an increase in combustion air temperature also results in an increase in outlet temperature of the air used for cooling of the coils. This suggests a higher heat flux in all areas from the flame to the coil which is a result of a slightly higher flame temperature, as could not be derived from Figure 7.1.37 because of the representation as 'relative' duty. This could be a result of the increased total energy input, by increasing the combustion air temperature while keeping a constant fuel flow rate. However, Figure 7.1.40 does not show the same trend as Figure 7.1.39. This could be due to the changing mass flow of the cooling air, which is adjusted between every run to keep the oxygen level at 2%. But the increased total energy due to the increased combustion air temperature is minimal, so It can be that the increase in heat flux is small and almost not measurable with the test performed during this study. It also takes around 15 minutes for the temperature to rise to a constant level again, which is longer than the actual time between the test runs.

Another parameter that may indicate that the increased temperature at the air outlet could be a result of the increased combustion air temperature is the firebox temperature. The firebox temperature at the burner side (front) and at the stack side (back) as illustrated in Figure 5.2.21 are given in Table 7.1.3. The test runs are carried out from left to right as mentioned in the table with test number. This table shows an almost steady temperature for the test numbers 3 to 8 with a small increase with increasing combustion air temperature. This would again indicate that the change in heat flux is small and that the combustion air preheating has little influence on the heat flux. A reason for the lower temperatures at test runs 1 and 2 could be that the firebox wasn't warmed up enough while doing the test runs. In other words, the firebox temperature did not yet reach steady state, or almost steady state, during the first two test runs.

Table 7.1.3 - The firebox temperature at the burner side (front) and at the stack side (back) as illustrated in Figure 5.2.21 for the different combustion air preheat temperatures in both firing modes.

	SU				**75% LN**			
Test nr.	1	2	3	4	8	7	6	5
T_{APH} [°C]	10	100	200	270	10	100	200	270
T_{front} [°C]	532	584	631	639	-	647	662	657
T_{back} [°C]	624	698	747	763	-	728	749	740

Outliers

Another thing worth mentioning are the outliers in the graphs shown in Figure 7.1.37 to Figure 7.1.40. Especially at coil number 15, 22, 30 and 32 the raw data points are not in line with the expected outcome. The most probable reason for this is a higher flow resistance, resulting in less air flowing through that coil. The cause of this increased flow resistance could be a thicker weld joint, a burr inside the coil, or a inaccuracy of the tube diameter. The air flow is distributed over all 36 coils having a diameter of 89 mm and a wall thickness of 3 mm, so a slightly difference in flow resistance of a coil results in a difference of air flowing through a coil. The air is heated to from 5°C to 400°C approximately, so a difference of 1% in air flow rate results in a difference of 4°C in air outlet temperature of the coils. The value of coil 15 seems to be approximately 30°C to high, which would suggest that the air flow rate through that coil is 7-8% lower. This could be caused by a diameter that's around 2% smaller, i.e. an inaccuracy of 1-2 mm in diameter, or other resistances due to the welding of the coils.

To clear this error, or at least minimize, a 5-point moving average is used. An average is taken out of the point value plus the two left and right of that value. This is the trendline in Figure 7.1.37, Figure 7.1.38, Figure 7.1.39 and Figure 7.1.40.

7.2. NO_x emissions

This paragraph will show and discuss the results originated from the flue gases concentration measurements using the ECOM J2KN-PRO gas analyzer during the experiments. This will help to investigate the influence of the combustion air temperature on the NO_x formation within the firebox. Figure 7.2.41 shows the amount of NO_x in ppmv for different combustion air preheat temperatures at both SU and 75% LN modus. Full LN modus was not reached as discussed earlier. A trendline of the form of an exponential as illustrated in Figure 3.2.15 can be observed in the experimental results. The error bars are derived from the accuracy of the measurement equipment.

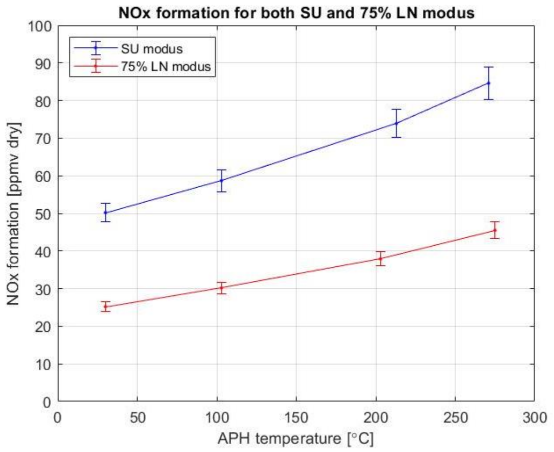

Figure 7.2.41 – The amount of NO_x formation for different combustion air preheat temperatures measured in the flue gases for both burner firing modes.

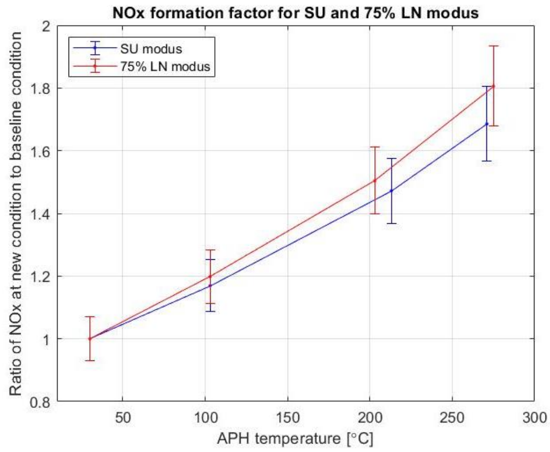

Figure 7.2.42 – Range of ratios given for the NO_x formation for both tested burner firing modes.

From the measured data, a polynomial or exponential fit can be derived to calculate the increase in NO_x formation for different combustion air preheat temperatures compared to the baseline condition. This can be done for both firing modus and they result in a range of ratios for the NO_x formation at the new condition to the baseline conditions. This is illustrated in Figure 7.2.42. The accuracy of the measurement equipment is again taken into account, which resulted in a wide range for the ratio per APH temperature. This graph is useful for comparison with the graph shown in figure Figure 3.2.15.

The correlation for NO_x emissions in hydrogen and ethylene fired heaters from Technip Energies would result in 25.4 ppmv NO_x emissions using a firebox temperature of 700°C, no preheating and bottom or top firing pf the LSV® burner in full LN modus. This is in line with the measured NO_x emissions of 52.2 ppmv during 75% LN modus without preheating.

8
CFD modelling

The previous chapter's design for the ECAP will be used for a numerical model analysis with CFD to get a better understanding of the airflow, heat flux, and pressure drop of the system. First, the difficulties and pitfalls of making and analyzing a CFD model will be discussed, followed by the geometry, mesh generation, model selection and the results.

A numerical model can provide a good alternative for experiments, saving time and costs. However, the results can only be of any value if the model has been developed according to certain guidelines. Above all, there should be a proper understanding of heat transfer, fluid mechanics and numerical equations used by the software package. The creator of the CFD model should at all times be aware of every simplification and assumption that has been made to understand the outcome and determine the quality of the results. A CFD model consists of three main components, a pre-processor, a solver and a post-processor. The pre-processing stage often requires the most time to ensure the quality of a CFD model.

The CFD model built during this thesis will be analyzed using FloEFD (version 2020.2). Compared to other CFD software packages like ANSYS Fluent, this is easy to use and requires less CFD training and knowledge. FloEFD was mainly developed to simulate and study turbulent flows since most fluids problems encountered in engineering practice are turbulent flows, but it is also capable of predicting laminar flows and the transition from laminar to turbulent flows.

As provided in section [3.4 FloEFD CFD Solver], does FloEFD solve the Navier stokes equations supplemented by steady state equations, empirical dependencies of fluid properties, and the so-called *k-ε model* to predict the turbulent flows. The methods used to describe the flow in near wall regions is also discussed in section [3.4 FloEFD CFD Solver].

All calculations have been simulated on a desktop from Technip Benelux with a FloEFD license. This desktop had the following hardware: Intel® Xeon® W-2145 CPU, 64 GB of RAM and a NVIDIA Quadro P4000 graphics card.

8.1. Geometry

Determining the system's geometry is the first step that has to be taken to develop a CFD model. It is almost impossible to make a detailed CFD analysis of the whole system at once because this requires a lot of computational resources. Consequently, the mesh should be a trade-off between the accuracy and the calculation time needed, where smaller grid cells are placed in critical regions in order to capture the relevant heat transfer and flow characteristics, and more coarse cells are used in less relevant regions. Therefore the geometry used during the CFD modelling is a slice cut of the whole system that represents the whole system.

This geometry will consist of a cross-sectional area of 12x3 mm with a piece of the tube bank that represents the whole tube bank geometry. This geometry is illustrated in Figure 8.1.43 to Figure 8.1.45 and inspired by other studies [56], [91]. The upper part of Figure 8.1.45 is a right plane view and the lower part of Figure 8.1.45 the front plane view.

Table 8.1.4 – The dimensions, ratio of the cross-sectional area of the whole ECAP (A_t) and CFD geometry (A_g) and the mass flow of the computational domain.

Width (x)	12	mm
Heigth (z)	3	mm
Length (y)	250	mm
Ratio A_t/A_g	4356	-
Mass flow	1.59 E-4	kg/s

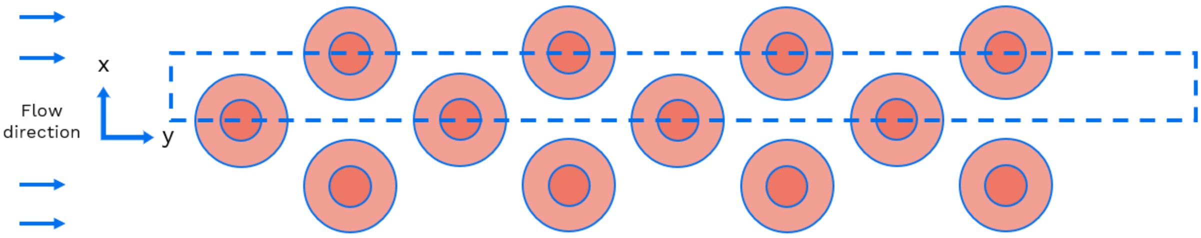

Figure 8.1.43 – Side view (x-y plane) of the used computational domain.

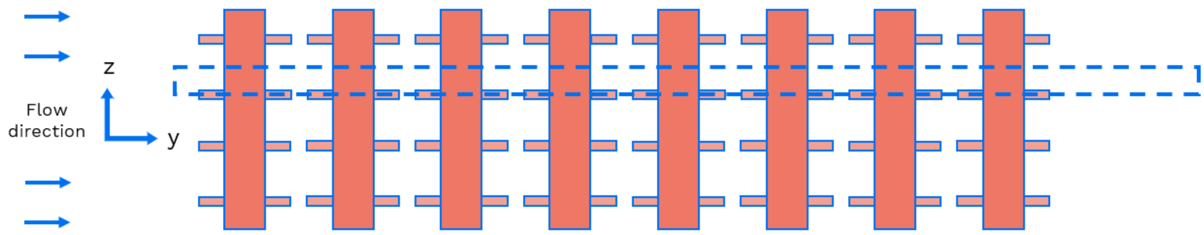

Figure 8.1.44 – Side view (z-y plane) of the used computational domain.

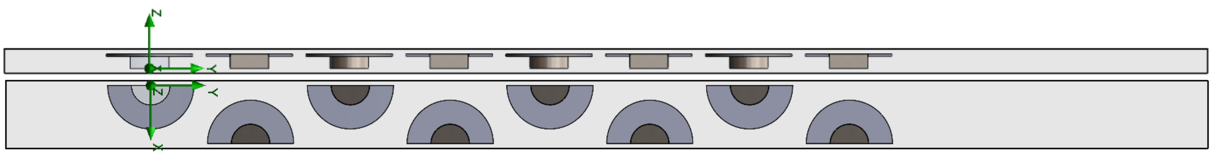

Figure 8.1.45 – Geometry of the used computational domain.

8.2. Mesh generation

The mesh generation is of great importance for the quality and calculation time required for the CFD model. The Favre-averaged Navier Stokes equations, energy conservation laws and fluid state are solved numerically on a mesh in the computational domain using the *finite volume method*. The computational domain is divided into smaller domains called cells, and a more refined mesh generally yields a more accurate result but is also more expensive in terms of calculation time. After sufficient refinement of the mesh a solution is obtained that no longer changes after even more grid refinements. This is called grid-convergence or grid independence.

Mesh refinement validation

A mesh grid is often non-uniform, which means that the grid is more refined in areas where large gradients in fluid or solid properties are encountered and more coarse in areas where little gradients in fluid or solid properties occur. Therefore the refinement level of the automated mesh generator is adjusted from 1 (coarse) to 7 (finest) while the outlet bulk temperature and pressure drop are observed. The meaning of these refinement levels is given in Appendix C. If these values are identical within the required accuracy for two subsequent mesh refinement levels, it can be concluded that the values of these two parameters do not depend on the size of the grid elements anymore and that grid independence has been reached. In general, when specific phenomena inside the computational domain are important, also for the model predictions related to those phenomena, a grid independence test has to be performed.

The only parameter required for the mesh generator of FloEFD is the minimum gap size, which is the smallest gap within the system. The minimum gap size is set at 2 mm for this specific CFD model. The automatic grid generator will take this into account when generating the mesh grid, while the mesh refinement can be adjusted from 1 to 7. Figure 8.2.46 provides the grid independence, i.e. grid convergence, for this specific CFD model. Appendix C provides the outcome of these refinements levels for this CFD model together with the meaning of these refinement levels. According to the grid convergence, refinement level 6 provides a sufficiently refined mesh grid for this geometry. The results for the generated mesh corresponding to mesh refinement level 6 for one heating element are shown in Figure 8.2.47.

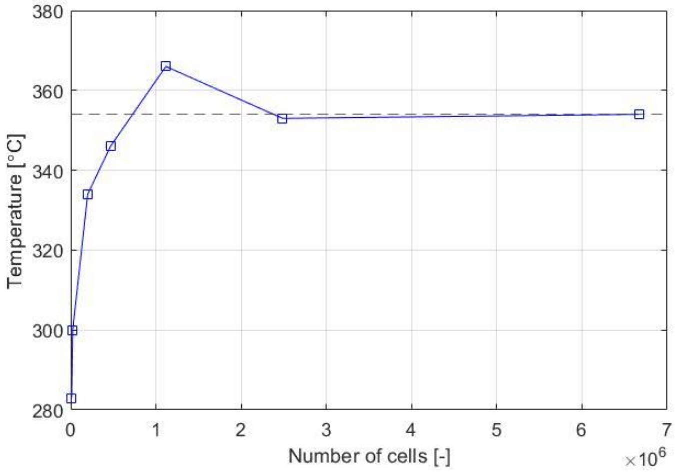

Figure 8.2.46 – Grid convergence of the computational mesh to a bulk temperature value of 353. Mesh refinement level 1 to 7 from left to right point box.

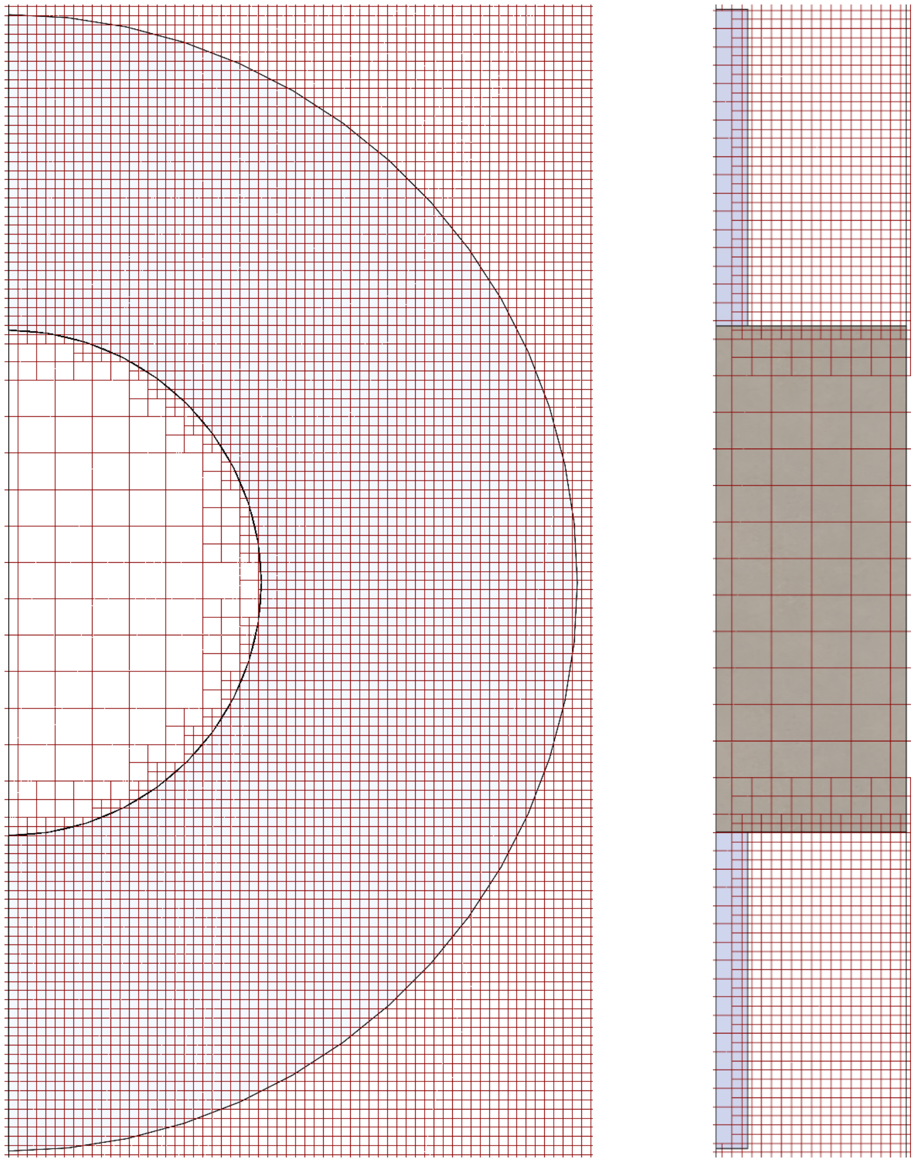

Figure 8.2.47 - Mesh grid for refinement level 6. Front view (L) and right view (R).

8.3. Boundary conditions

During the pre-processing stage, the initial ad boundary conditions are set, which are an essential part of the development of a CFD model. Within the FloEFD software program, several possible boundary conditions exist like internal flow, external flow, wall and periodic boundary conditions. For the present application, only the internal flow and wall boundary conditions are needed.

Internal flow boundary conditions can be manually specified at the model inlets and outlets, i.e. openings. They are classified into ‘pressure openings’, ‘flow openings’ and ‘fans’. A pressure opening which can be static, total or environment pressure is imposed when the flow direction and/or magnitude at the opening are not known. A flow opening is imposed when the dynamic flow properties are known at the opening. If the flow enters the model, the temperature, fluid composition and turbulence parameters must also be specified. A fan condition is used when a fan is installed at a model opening. The dependency of the volume flow rate on pressure drop is prescribed at the opening, which is commonly provided in the technical documentation of the fans. The variables that are not specified at the inlet are calculated from the solver equations.

Wall boundary conditions must be specified at solid walls of the model. They are classified into real, ideal and outer walls. A real wall corresponds to the well-known no-slip condition for velocity, and the ideal wall corresponds to the well-known slip condition. The walls are also considered impermeable, and the ideal wall condition can be used to model planes of flow symmetry. If conjugate heat transfer through the solid walls is not considered, the wall temperature or heat flux boundary condition can be imposed. When the conjugate heat transfer is considered, these do not have to be specified and they will be calculated during the solver stage. The surface roughness determines the friction of the air along the real walls.

The boundary conditions used here are:

- An internal flow - static pressure boundary condition at the outlet.
- An internal flow - flow boundary condition at the inlet.
- An ideal wall boundary condition at the casing walls. (zero surface roughness)
- A real wall boundary condition at the bare heating tube outer walls.
- A real wall boundary condition at the fins.

Table 8.3.5 – Values for certain boundary conditions.

Variable	**Value**	**Units**
Temperature air in	293.15	K
Mass flow air in	1.59 E-4	kg/s
Temperature bare tubes	923.15	K
Pressure air out	101345	Pa
Surface roughness	5	µm

8.4. Material properties

All materials properties of the air and the solids are specified in FloEFD input for the CFD modelling of the ECAP system. All solids, in this case the bare tubes and fins, are specified as stainless steel 321 with the material properties as given in Table 8.4.6. The properties of the combustion air are also given in that table. The outer walls are specified as insulator material, so no heat is transferred through these walls, meaning that the heat flux is zero.

Table 8.4.6 – The material properties for stainless steel 321 (left) and dry air (right) at atmospheric pressure and a temperature of 300 K.

Variable	**Value**	**Units**
Density	8100	Kg/m^3
Specific heat	510	J/kg*K
Thermal conductivity	15.1	W/m*K
Melting temperature	1683.15	K

Variable	**Value**	**Units**
Molar mass	28.96	Kg/kmol
Specific heat	1006	J/kg*K
Thermal conductivity	0.026	W/m*K
Dynamic viscosity	1.8 E-5	Pa*s

8.5. CFD results

This chapter provides the results of the CFD modelling using mesh refinement 6 with a minimum gap size set at 1 mm. The results are discussed in [9.2 CFD modelling].

Table 8.5.7 – Results from FloEFD for mesh refinement level 6.

Average temperature bare tubes (BC)	650	°C
Average temperature fins	586	°C
Average temperature heating elements	600	°C
Average heat flux bare tubes	5.28	W/cm^2
Average heat flux fins	4.43	W/cm^2
Average heat flux heating elements	4.61	W/cm^2
Average heat transfer rate bare tubes	13.3	W
Average heat transfer rate fins	41.2	W
Average heat transfer rate heating elements	54.4	W
Factor (total tube bank geometry vs CFD geometry)	4356	-
Bulk temperature air in (BC)	20	°C
Bulk temperature air out	353	°C
Average air velocity in (BC)	3.66	m/s
Average air velocity out	8.35	m/s
Pressure drop of tube bank	175	Pa

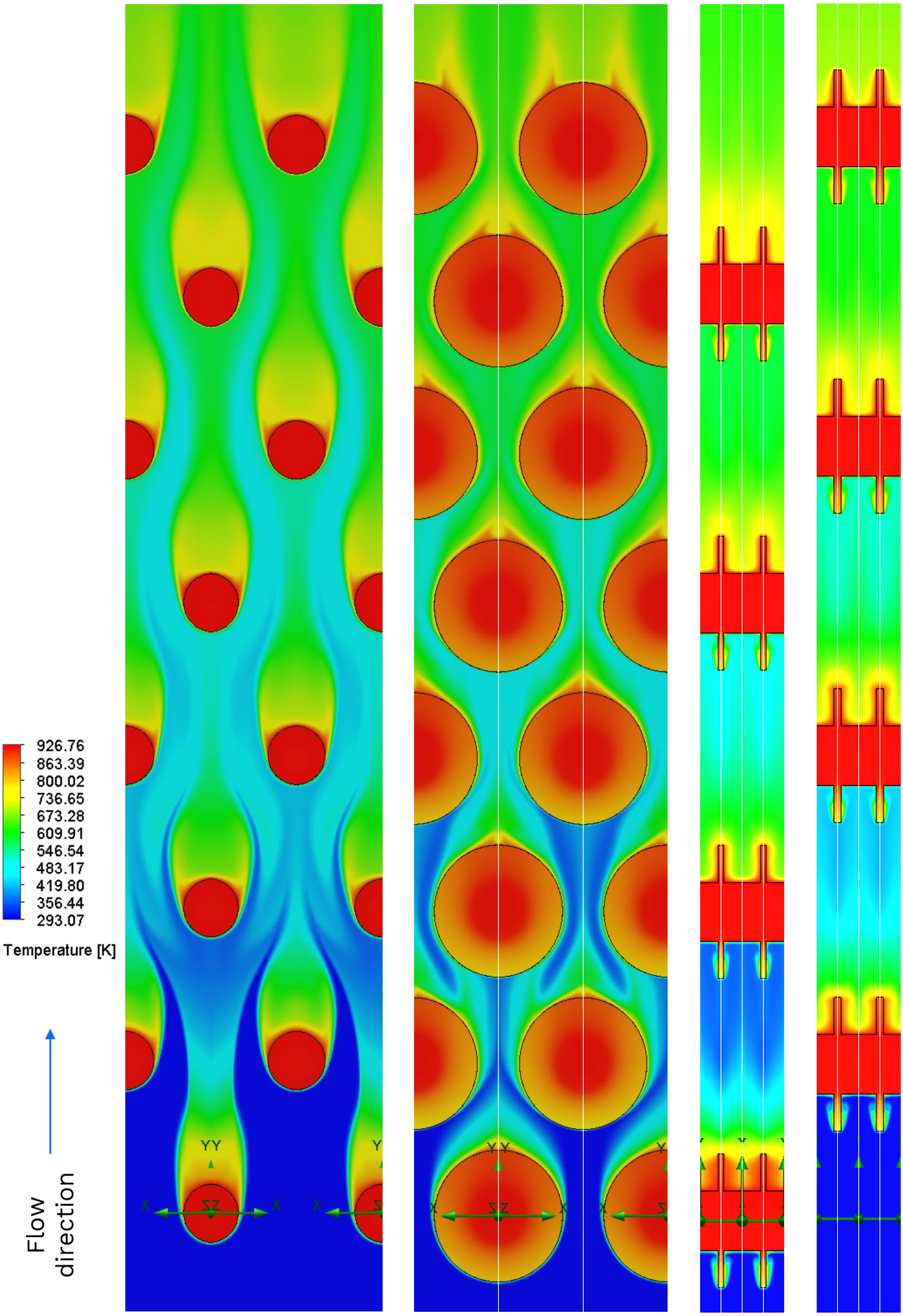

Figure 8.5.48 - Temperature isosurfaces from left to right, front plane view at 0 and 3 mm (z-direction), and right plane view at 0 and 12 mm (x-direction).

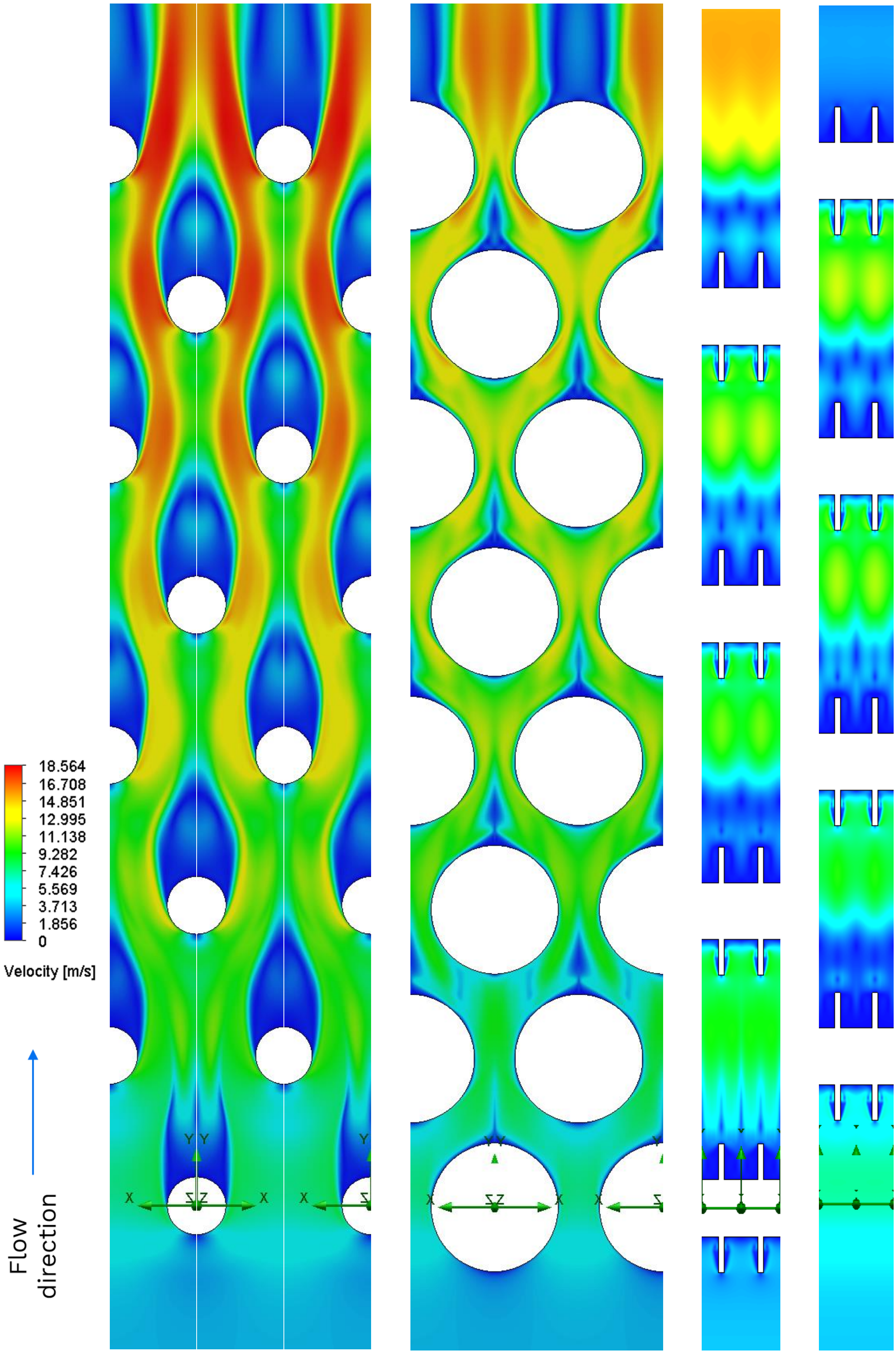

Figure 8.5.49 - Velocity isosurfaces from left to right, front plane view at 0 and 3 mm (z-direction), and right plane view at 0 and 12 mm (x-direction).

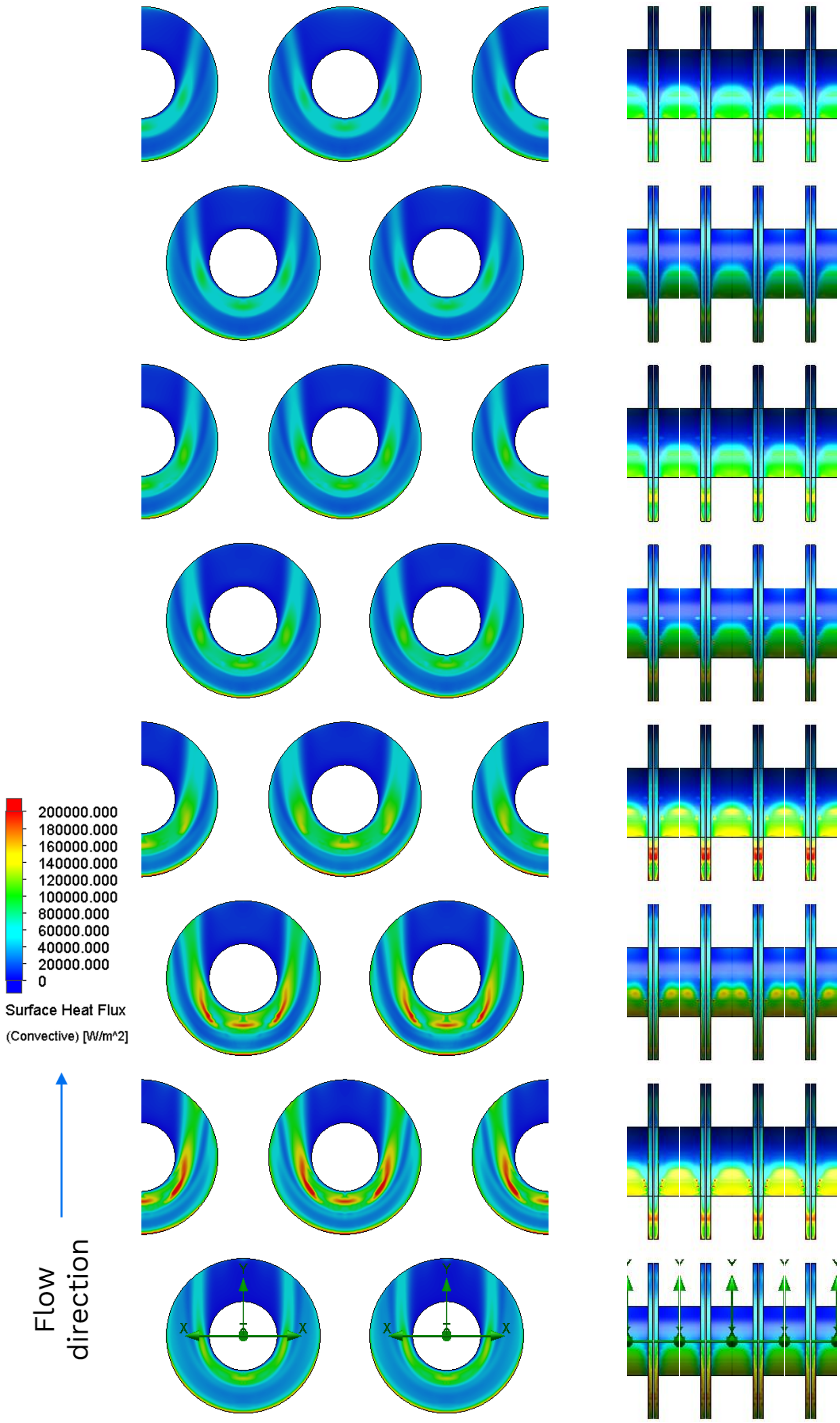

Figure 8.5.50 - Heat flux surface plots, front plane view (left) and right plane view (right).

9
Discussion

This chapter will discuss the results, as described in chapter 6-8, for each sub-project separately. In the next chapter the findings of the overall project will be discussed.

9.1. Equipment design

The design of the ECAP was obtained using the design procedure and the correlations. The outcome of the results of the equipment design is discussed here.

Equipment design

The results show that within the limitations and by meeting the criteria set at the beginning, the ECAP is able to heat up the air to a temperature of 300°C by using a finned tube bank of 400x400x200 (WxHxL) with a bare tube temperature of 650°C. Also higher temperatures up to 500°C could be achieved within these limitations. During the design, It is important to keep the velocity of the air within certain limits. Otherwise, the maximum pressure drop will be exceeded. The limiting factor for a more compact design is first of all the heating elements temperature since a higher temperature would result in more heat transfer per area. Other limiting factors are the tube diameter, the minimal gap spacing and the transverse pitch ratio. The tube pitch and transverse pitch ratio are limited by the manufacturing capabilities of these heating elements at suppliers.

For these finned tubular heating elements, round straight fins are used that are placed parallel to the flow to increase the heat transfer area. Maximizing the heat transfer area results also in a more compact design. It could be worth analysing the use of interconnecting rectangular plate fins between the tubes of one heating element, i.e. larger fins. This would results in a larger heat transfer area without exceeding the minimum gap spacing of 5 mm. The interconnecting plate fins could be attached per row. Another advantage of these rack-shaped heating elements is that they are easily replaceable, and extra rows of tubes can be added if more performance is needed.

The by-passing of the air at the outer side of the tube bank, between the tube bank and the casing, should be minimized or even prevented. By-passing of air results in less heating of the air, and performance will be lost. This can be prevented by reducing the gap between the outer tubes and the casing or by adding dummy tubes on the casing wall.

The results of the calculations done using the correlations for the heat transfer via convection are most probably an underestimation of the actual achievable heat transfer since radiation is not taken into account. The radiation from the heating elements to the casing can results in an increase of approximately 4% of the heat transfer rate. This heat is transferred from coil to casing by radiation and then from casing to air by convection.

CO_2 emissions reduction & cost savings

Using the ECAP with the LSV burner reduces the CO_2 emissions significantly. When operating for 3000 hours per year by using renewable electricity, 3.3% of CO_2 emissions can be reduced, i.e. 114 tons of CO_2 per burner per year, using combustion air temperature of 300°C. Increasing the combustion air temperature to 500°C results in an emissions reduction of 5.2%, i.e. 180 tons of CO_2 per burner per year. Not only does it reduce the CO_2 emissions, the implementation of the ECAP can also reduce the costs of the operation of the burner significantly over the years. On top of that, over time, the operating hours could increase to more than 3000 hours per year due to an increasing portion of renewable electricity resources installed, providing the possibility to increase the operating hours of the ECAP over the years, i.e. strengthening the business case.

9.2. CFD modelling

The chosen design of the ECAP was modelled using the CFD package FloEFD. The outcome of the results of the CFD modelling is discussed here.

The mesh grid refinement level of the CFD model is verified using the grid independence method. Refinement level 6 was sufficient enough to obtain a result with the preferred accuracy. That means that the mesh cells around the geometry were small enough to accurately calculate the convection from the heating element to the air and the airflow around the heating elements. The standard k-e turbulence model is accurate enough to predict the flow of air around finned tubular heating elements, and the geometry that Is used provides a good representation of the ECAP.

The result from CFD matches the results from the equipment design well. The rows from the equipment design were rounded off so that a discrete number of rows could be used. For the CFD model 8 numbers of rows were used, while the number of rows obtained from the correlations was slightly above 7. By changing the number of rows in the calculations to the exact number of 8, an air outlet temperature of 335°C is obtained. This is within the range of 353°C that was obtained using CFD modelling. The same can be said about the pressure drop since the 183 Pa from the calculations matches the 175 Pa from CFD modelling. It can be concluded that both the correlations and the CFD modelling can predict the heat transfer and pressure drop match within certain limits and can be used for predicting the heat transfer and pressure drop for this system.

9.3. Burner test results

From the burner test results, the influence of combustion air preheating on the burner and fired heater performance was analysed. The outcome of the results is discussed here.

Heat flux

The results show that heating up the air to a temperature of 300°C has little to no influence on the heat flux profile. A slightly higher heat flux can be achieved while keeping the fuel gas flow constant. Another option is to keep the total energy input, which is the combustion heat release plus the combustion air preheat, constant by decreasing the fuel gas flow with increasing combustion air temperature. In that case will the heat flux stay the same. Also, the peak heat flux does not shift closer or further away from the burner, according to the test results. Both outcomes are beneficial for the implementation of the ECAP since no significant interventions have to take place. This can be studied in more detail using CFD of the fired heater.

It could also be that the change in total energy input was too small to observe changes in the heat flux profile. To investigate this, a higher combustion air temperature could be tested, for instance, 600°C. The time between the test runs was also relatively short (10 min). To make sure that the measured data is taken during steady-state operation this could be increased. Both could result in a more accurate and clearer outcome. The results also show outliers in the data measured. These could be resolved by checking the cooling coils inside the test fired heater on faults in weld joints, a burr inside the coil, or an inaccuracy of the tube diameter. For now, this is resolved by using a moving average for the measured data.

NO_x formation

The NO_x emissions should be reduced as much as possible because it is responsible for the formation of ozone (GHG), the formation of smog and the general acidification of soil and water. Looking at the results, they show that the NO_x formation does increase with increasing combustion air temperature. Although no full Low-NO_x modus (LN modus) was reached due to a low fired heater temperature and a 75% LN modus was used, an expected trend of the NO_x formation as discussed in [3.2 Burner NO_x formation] was observed. The increase of the NO_x is mainly due to the increase of flame temperature caused by the increase in combustion air temperature. Again this can be studied in more detail using CFD of the fired heater.

10
Conclusions and Recommendations

Reducing the CO_2 emissions of the fired heaters that provide the required energy for industrial processes is one of the biggest challenges for the industry in the energy transition. Switching to renewable electricity for some high-temperature processes can be part of the solution. Fuel consumption and CO_2 emissions are reduced by using renewable electricity for combustion air preheating within the fired heaters.

The objective of this study is to design a cost-effective and compact electric combustion air preheater (ECAP) for the LSV® burner from Technip Energies. Analyzing the impact of such a design on the burner and fired heater performance, also based on experiments, shows the potential in reducing CO_2 emissions. This section summarizes the findings of the research questions and provides some recommendations for future research.

10.1. Conclusions

What is the design of a cost-effective and compact ECAP for the LSV® burner from Technip Energies?

The most suitable method to heat combustion air using electric power for this specific application with the limitations as discussed in the Basis of Design is by using finned tube heating elements. These tubes are less prone to fouling, have a good mechanical strength and are easy to install. Using fins on the bare tubes, provides the most compact design, and the tubes can be used at an operating temperature of 650°C. The design recommended and calculated using the VDI method for the heat transfer and pressure drop can heat up the combustion air to a temperature of 300°C. It is even possible to achieve higher temperatures by adjusting the design as given in the Appendix B. The maximum allowable pressure drop for this system was set at 200 Pa, which is not exceeded by the design recommended.

How will the ECAP influence the LSV® burner and fired heater *performance?*

The usage of combustion air preheating in combination with the LSV® burner is experimented with using the Technip test fired heater. The heat flux profile does not change significantly when increasing the combustion air temperature. The NO_x emissions do increase exponentially with increasing combustion air temperature. This is mainly due to the increasing flame temperature resulting in Thermal NO_x formation. NO_x emissions should be reduced, since they are responsible for the formation of smog and the general acidification of soil and water. Possible solutions are discussed in recommendations.

How much CO_2 emissions can be reduced and costs can be saved using the ECAP?

The amount of CO_2 emissions that can be reduced and costs that can be saved is substantial. A condition for saving CO_2 emissions is that renewable electricity is used. According to best current estimates savings on costs can only be achieved if the operating hours of the electric combustion air preheater are limited to 3000 hours per year. This could increase over time. While operating 3000 hours per year and heating up the air to a temperature of 300°C, a reduction of 114 tons of CO_2 per year, i.e. 3.2%, can be achieved for each burner. The implementation of the equipment is already making a profit after five years, and it can save 10.000 euros per year on OPEX, which will increase over time. By increasing the combustion air temperature to 500°C, the amount of CO_2 emissions that can be reduced is 180 tons per year, i.e. 5.2%. The breakeven point is already at four years, and more OPEX can be saved.

10.2. Recommendations

Based on the work done during this study, some recommendations for improvements and further research can be given. One recommendation would be toward the improvement of the performance of the heating elements. The heat transfer area could be increased by using interconnecting rectangular plates covering one heating element instead of the circular fins. This could result in a higher heat transfer rate per heating element to the air. The tubular heating elements could also be improved by using a smaller tube diameter, decreasing the transverse pitch ratio or using oval-shaped tubes.

Another recommendation would be towards improving the accuracy of the burner test and making adjustments to the test fired heater. This could result in a more clear change in heat flux profile and or better results for the prediction of NO_x emissions. The test results could be made more accurate by increasing the time between the test runs so that a steady-state temperature of the fired heater can be reached. A modification to the test fired heater would be using another method to heat up the combustion air so that higher temperatures could be obtained in the range of 500-600°C. The test fired heater was not able to reach higher combustion air temperatures due to the limiting temperature of the heating coils.

Not only the test fired heater design could be improved, also the burner design could be improved. When improving the design of the burner, the following NO_x control strategies should be taken into account: Increasing the mixing of the air and fuel by swirling and staged combustion, reducing the oxygen and nitrogen content in the flame zone by gas recirculation, decreasing the peak temperature and reducing the residence time at elevated temperatures. Also, using a catalyst for post-flame flue gas treatment is an option to decrease NO_x emissions. A document from the US Environmental Protection Agency (EPA) on the NO_x control during external combustion provides a solid foundation from which can be worked further on.

For further research, the electric combustion air preheater could also be tested using another fuel, like natural gas and hydrogen mixtures. Using hydrogen as a fuel is one of the solutions for the decarbonization of fired heaters. The combustion of hydrogen has other characteristics compared to the combustion of natural gas. Thermal NO_x becomes more relevant when increasing the amount of hydrogen in the fuel due to a higher flame temperature.

Appendix A

Fuel gas specifications

From supplier:

CH_4	93.1207	mol%
C_2H_6	4.5759	mol%
C_3H_8	0.8194	mol%
C_4	0.3416	mol%
C_5	0.0447	mol%
C_6	0.0237	mol%
CO_2	0.4883	mol%
H_2	0	mol%
He	0.05	mol%
N_2	0.5357	mol%
Total	100	mol%
Density ratio	0.5985	-
Density air	1.2922	kg/m^3
Density_fuel	0.7734	kg/m^3
Wobbe	538667	MJ/m3(n)
Hi	37.623	MJ/m3(n)
Hs	41.667	MJ/m3(n)

Derived using COMCON software and above information:

Fuel flow	1	kg/hr
excess air	0	%
T_comb.air	10	degC
T_fuel	10	degC
T_ambient	10	degC
Humidity	70	%

Density_fuel	0.771	kg/m^3
Density air	1.2922	kg/m^3
Density ratio	0.5967	-
M_air	28.965	g/mol
M_fuel	17.282	g/mol
M_fuel	17.284	g/mol

fuel-air ratio	16.8113	-
Hi	37.535	MJ/m3(n)
LHV	48.6831	MJ/kg
Hs	41.562	MJ/m3(n)
HHV	53.9071	MJ/kg

Capacity	2	MW
Fuel flow rate	0.041	kg/s
	147.895	kg/hr
Combustion air flow rate	**0.691**	**kg/s**
	2486.312	kg/hr

Appendix B

Other setups

Alternative 1

Width casing	0.444	m
Height casing	0.444	m
Diameter tubes	8	mm
Pitch ratio longitudinal	2.598	-
Pitch ratio transverse	3	-

Temperature inlet	20	°C
Temperature outlet	400	°C
Temperature tubes	600	°C
Air mass flow	0.691	kg/s
Inlet velocity bank	2.91	m/s
Outlet velocity bank	6.68	m/s

Fin spacing	5	mm
Fin height	5	mm
Fin width	1	mm

$\overline{Nu}_{Bundle}$	22.2	-
Heat flux	5.9	W/cm^2
Average heat flux	4.2	W/cm^2
Heat transfer coefficient	94	$W/K{\cdot}m^2$
Number of rows	9	-
Length of tube bank	192	mm
Length of total system	613	mm
Pressure drop of system	172	Pa

Alternative 2

Width casing	0.492	m
Height casing	0.492	m
Diameter tubes	8	mm
Pitch ratio longitudinal	2.598	-
Pitch ratio transverse	3	-

Temperature inlet	20	°C
Temperature outlet	500	°C
Temperature tubes	650	°C
Air mass flow	0.691	kg/s
Inlet velocity bank	2.37	m/s
Outlet velocity bank	6.25	m/s

Fin spacing	5	mm
Fin height	5	mm
Fin width	1	mm

$\overline{Nu}_{Bundle}$	18.8	-
Heat flux	5.5	W/cm^2
Average heat flux	3.4	W/cm^2
Heat transfer coefficient	97	$W/K{\cdot}m^2$
Number of rows	13	-
Length of tube bank	265	mm
Length of total system	778	mm
Pressure drop of system	166	Pa

Appendix C

CFD modelling

Mesh grid

The Level of initial mesh governs the mean number of cells (N_{mean}) per the model's middle size (H_{mean}) and the number of cells (N_{gap}) per the smallest flow passage/channel height, which specified by the Minimum gap size value (h_{gap}). First of all, the geometry resolution coefficient (K_{res}) is defined as the ratio of the model's middle size (H_{mean}) to the minimum gap size (h_{gap}). If it is smaller than 2.5, the number of cells per the model size (N_{mean}) and the number of cells per the minimum gap size (N_{gap}) are specified by using the table below. Note, that the real number of cells per a gap is restricted by the maximum allowed channel refinement level (L^*_{ch}).

Mesh refinement levels explained from [84].

<table>
<tr><th rowspan="3">Level of initial mesh</th><th colspan="3">N_{mean}</th><th rowspan="3">N_{gap}</th><th rowspan="3">L^*_{ch}</th></tr>
<tr><th rowspan="2">Internal</th><th colspan="2">External</th></tr>
<tr><th>Incompressible</th><th>compressible</th></tr>
<tr><td>1</td><td>5</td><td>2</td><td>3</td><td>2</td><td>0</td></tr>
<tr><td>2</td><td>7</td><td>3</td><td>5</td><td>3</td><td>1</td></tr>
<tr><td>3</td><td>10</td><td>5</td><td>7</td><td>5</td><td>2</td></tr>
<tr><td>4</td><td>14</td><td>7</td><td>10</td><td>7</td><td>2</td></tr>
<tr><td>5</td><td>20</td><td>10</td><td>14</td><td>10</td><td>2</td></tr>
<tr><td>6</td><td>28</td><td>14</td><td>20</td><td>14</td><td>4</td></tr>
<tr><td>7</td><td>40</td><td>20</td><td>28</td><td>20</td><td>4</td></tr>
</table>

Number of cells, outlet bulk temperature and pressure drop for different mesh refinement levels with a minimum gap size set at 2 mm.

Mesh refinement	1	2	3	4	5	6	7
Total number of cells	11612	23306	199585	466499	1116218	2485525	6667397
Number of fluid cells	3943	9114	72370	251043	749763	1930992	4963717
Number of solid cells	7669	14192	127215	215456	366455	554533	1703680
Number of contacting cells	3228	5940	48048	80698	175496	328998	690321
Avg cell size at fin surface [mm]	1.3	1.1	0.35	0.28	0.2	0.14	0.1
Outlet bulk temperature [°C]	283	300	334	346	366	353	354
Pressure drop [Pa]	109	124	137	152	166	175	183

Figures

Temperature

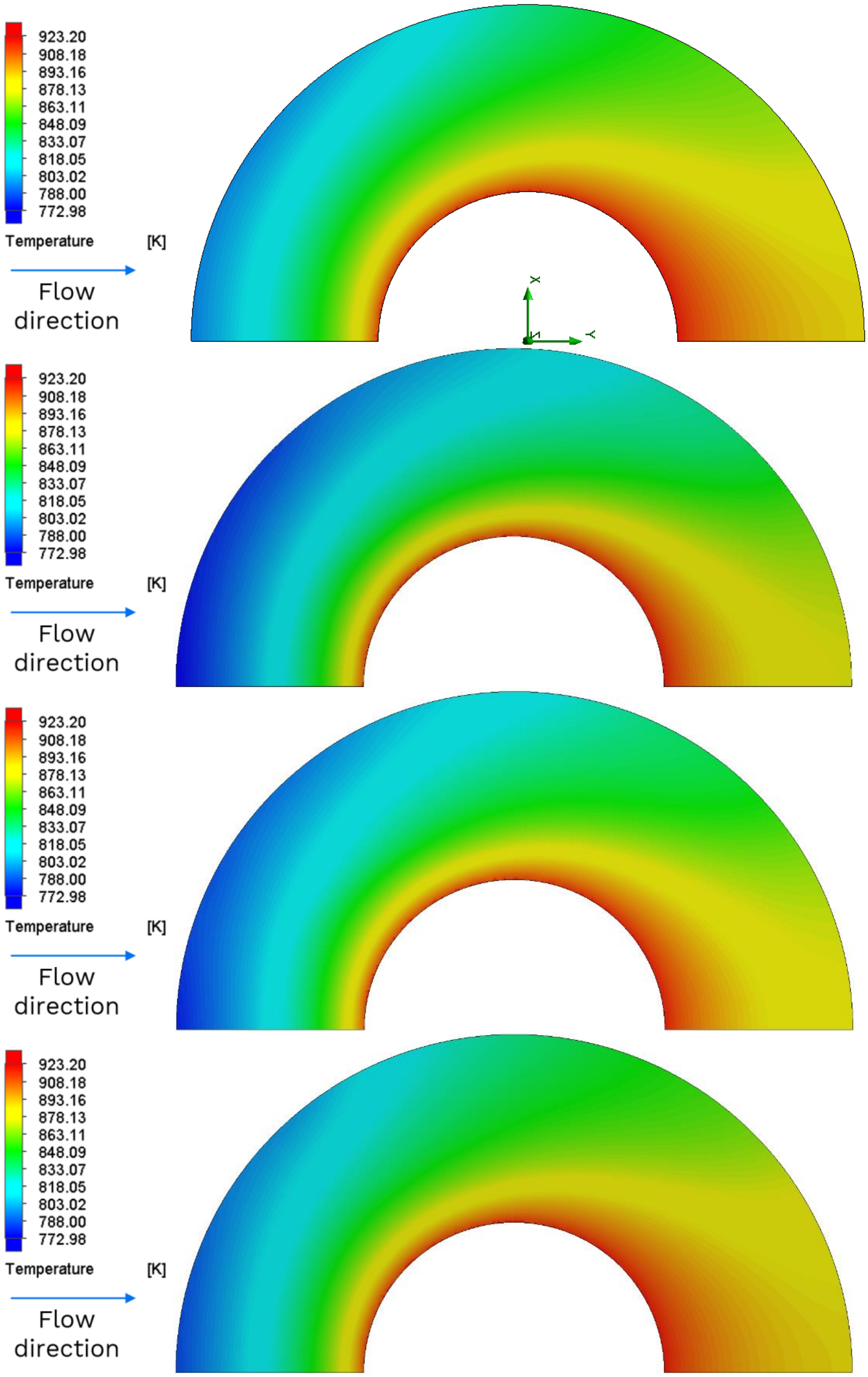

Temperature isosurfaces - Right plane view - From top to bottom row number 1 to 4.

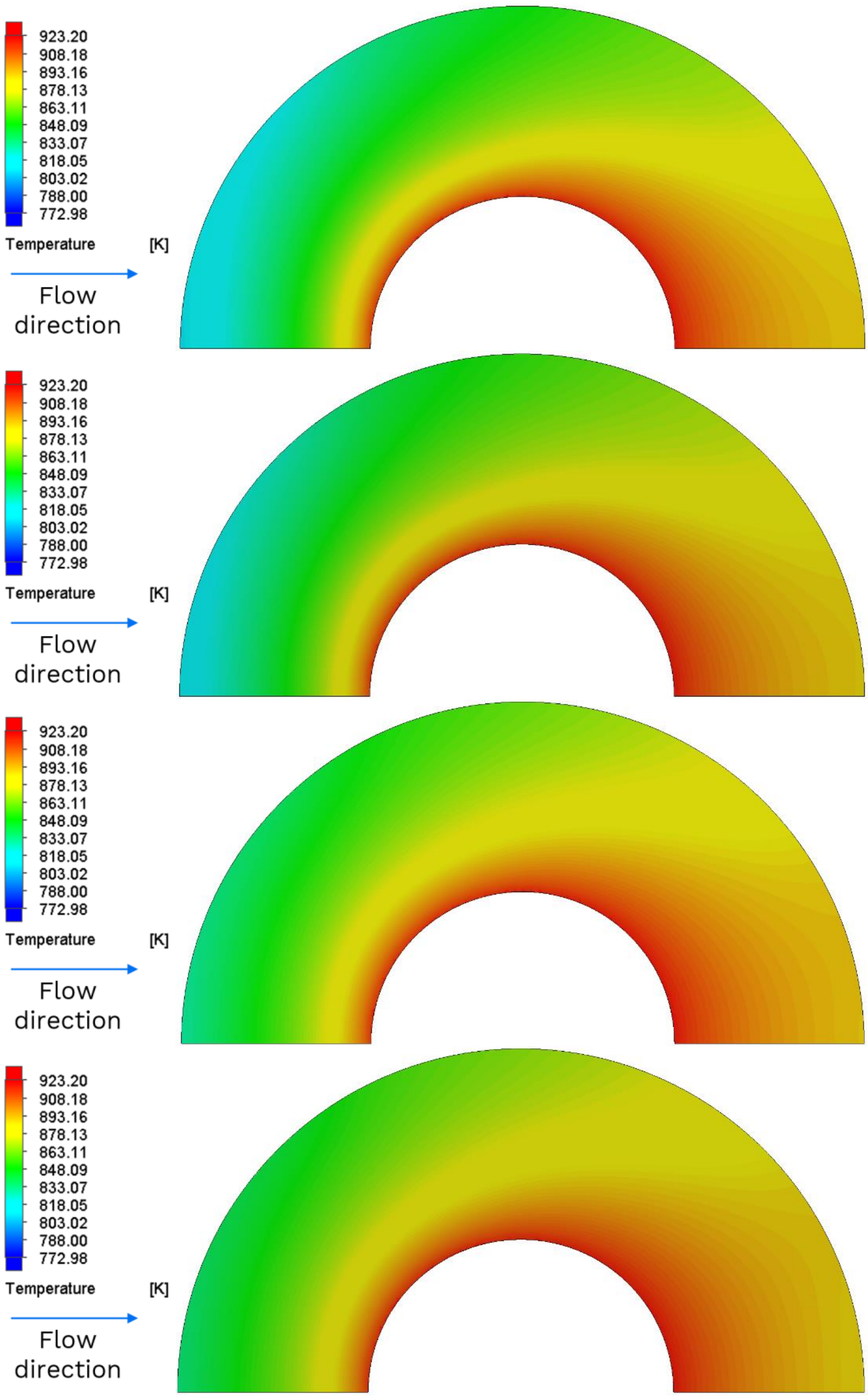

Temperature isosurfaces - Right plane view - From top to bottom row number 5 to 8.

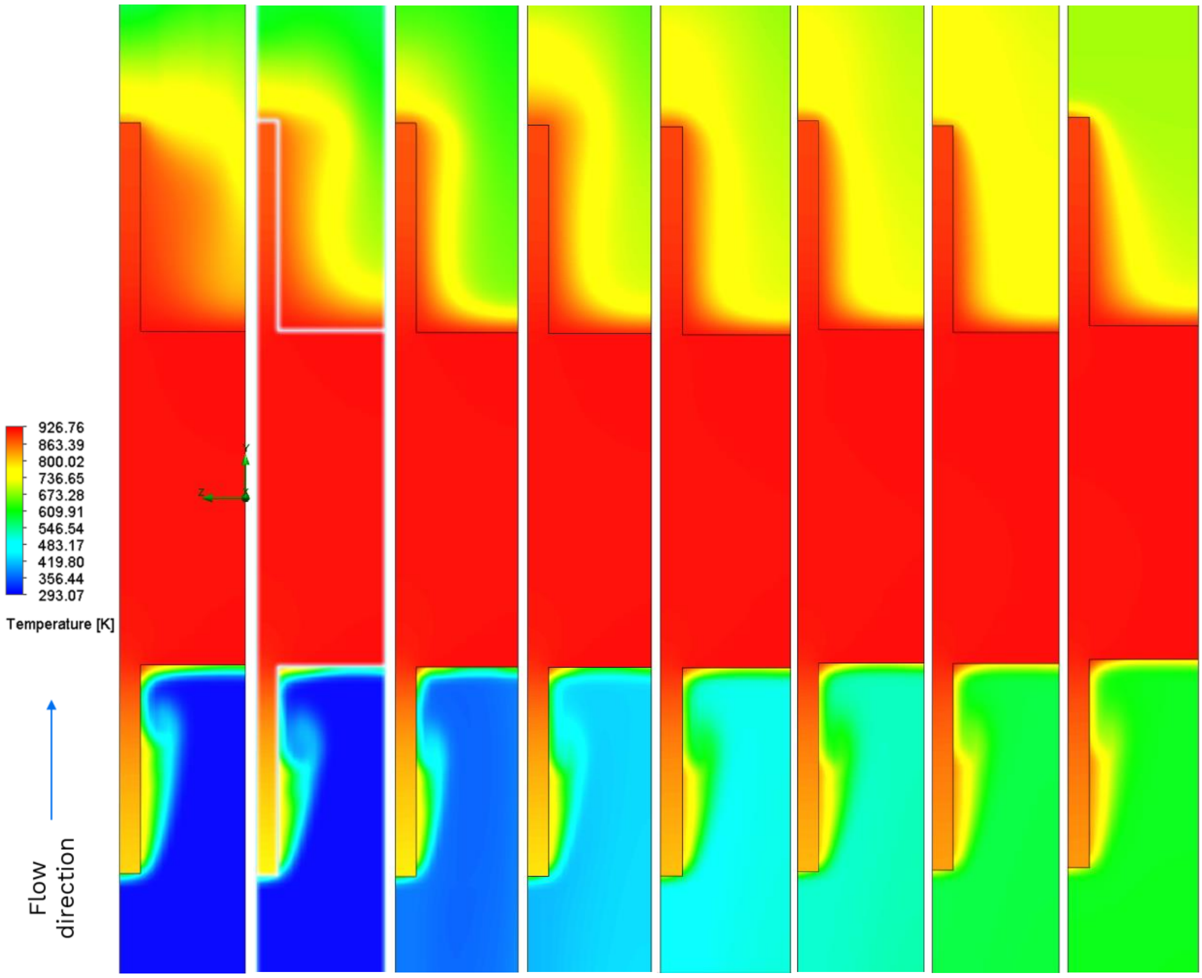

Temperature isosurfaces - Right plane view - From left to right number of row 1 to 8.

Velocity

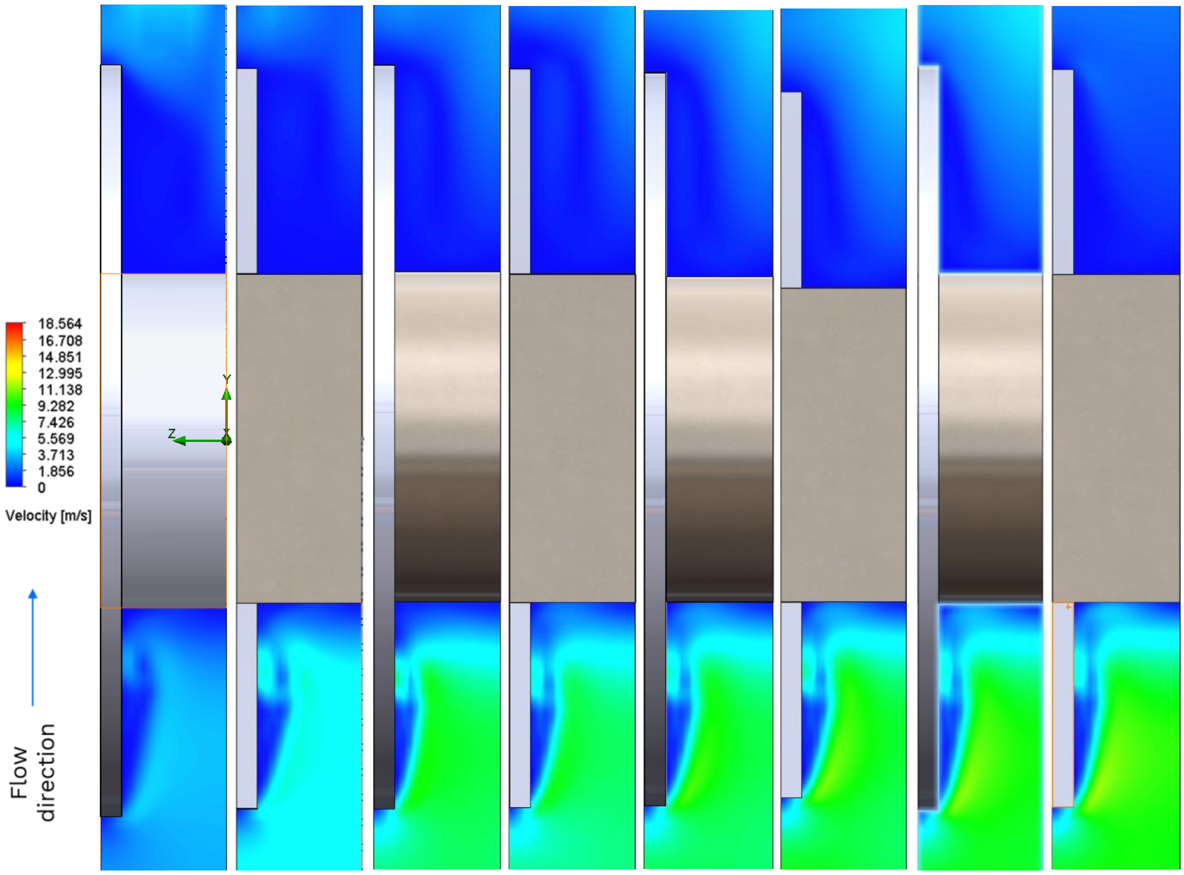

Velocity isosurfaces – Right plane view - From left to right number of row 1 to 8.

heat flux

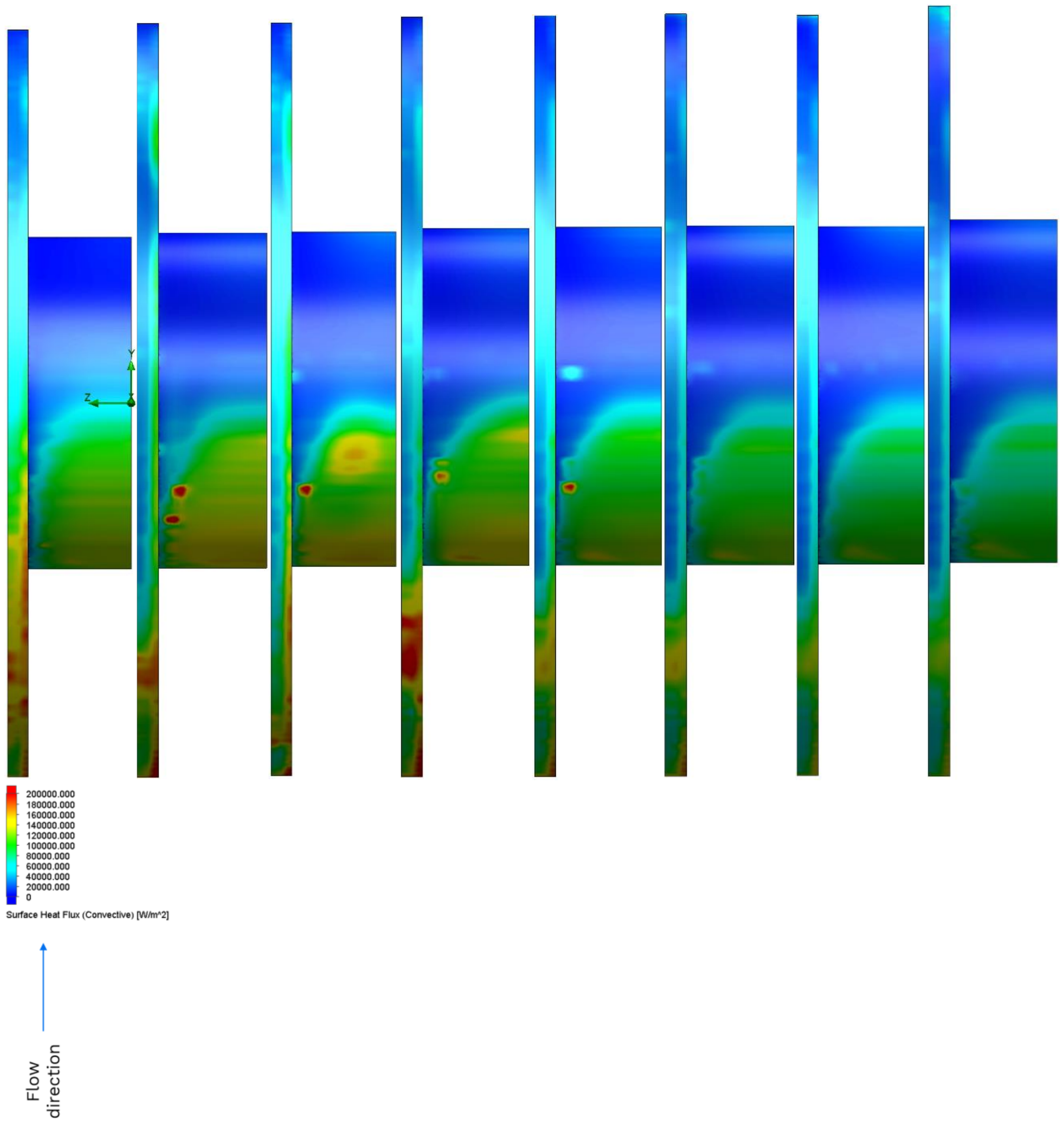

Heat flux isosurfaces – Right plane view - From left to right number of row 1 to 8.

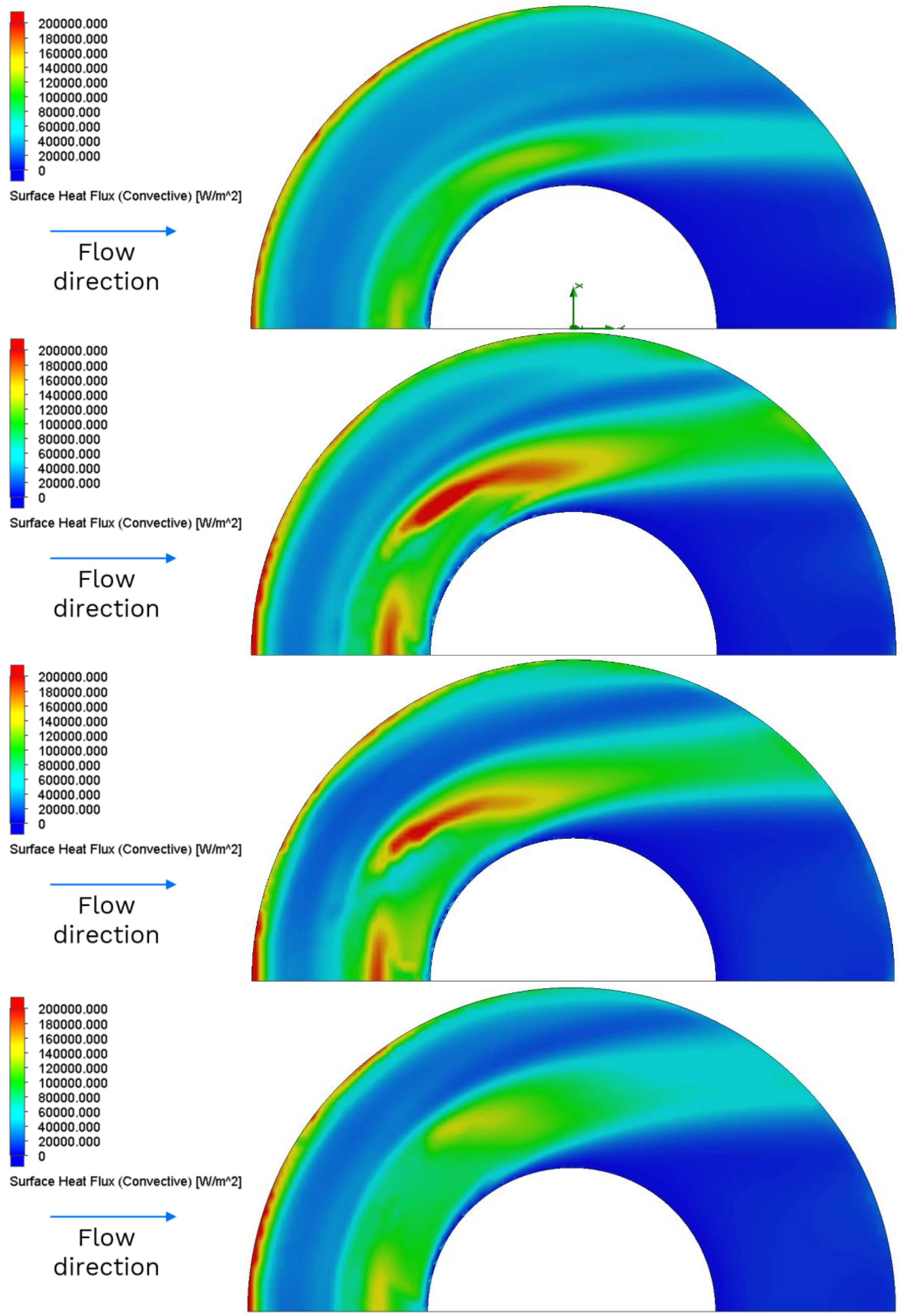

Heat flux isosurfaces - Right plane view - From top to bottom row number 1 to 4.

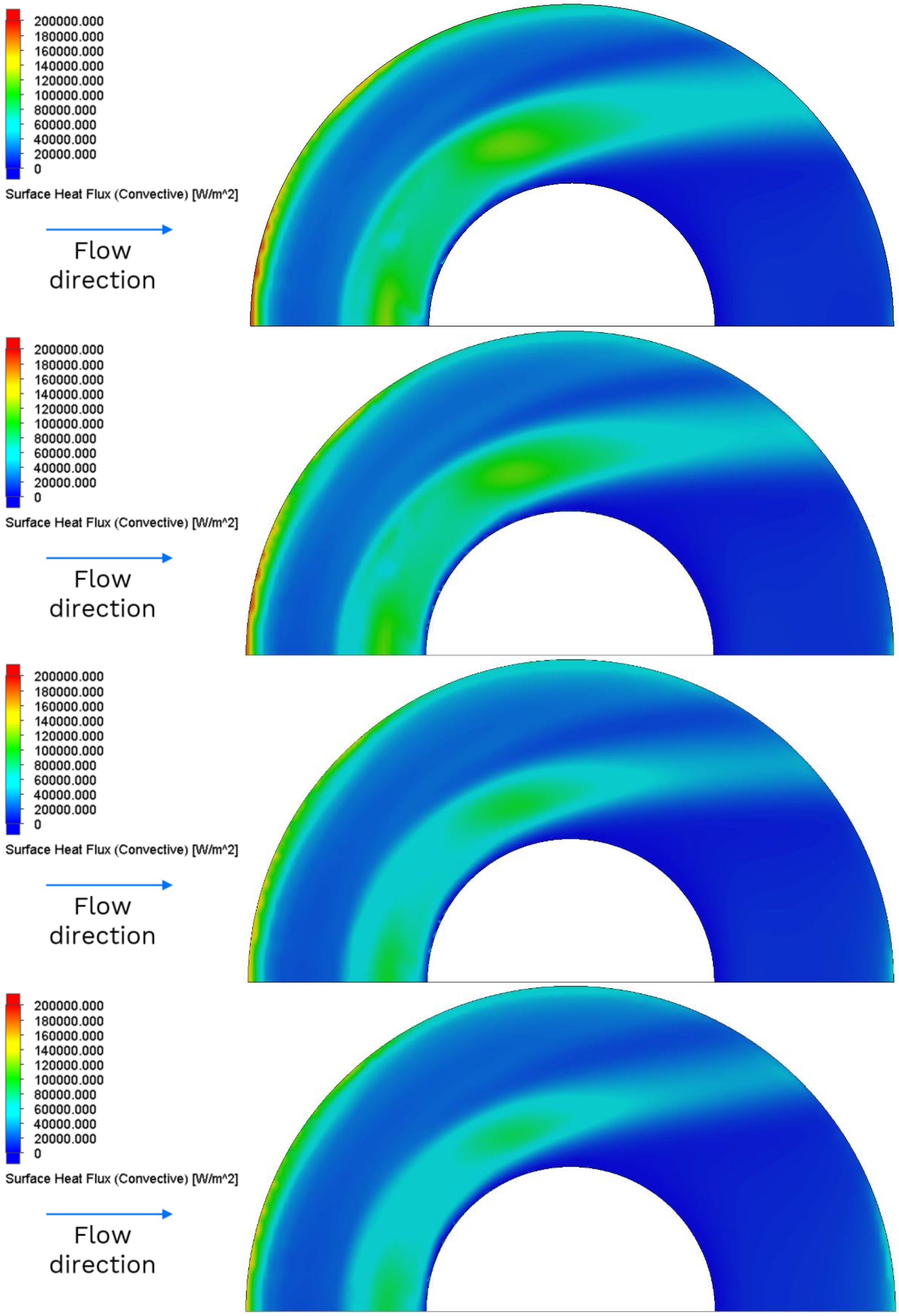

Heat flux isosurfaces - Right plane view - From top to bottom row number 5 to 8.

Bibliography

[1] UNFCCC, "The Paris Agreement," 2016.
[2] Rijksoverheid, "Climate Agreement," no. June, pp. 1–247, 2019, [Online]. Available: https://www.government.nl/documents/reports/2019/06/28/climate-agreement.
[3] Royal Dutch Shell, "Our climate ambition," 2020.
[4] BP, "Energy Outlook 2020," 2020.
[5] R. Den Haag, "Royal Dutch Shell must reduce CO2 emissions." https://www.rechtspraak.nl/Organisatie-en-contact/Organisatie/Rechtbanken/Rechtbank-Den-Haag/Nieuws/Paginas/Royal-Dutch-Shell-must-reduce-CO2-emissions.aspx (accessed Jun. 09, 2021).
[6] IEA, "World Energy Outlook 2020," 2020. Accessed: Dec. 23, 2020. [Online]. Available: www.iea.org/weo.
[7] IRENA, *Global Renewables Outlook: Energy transformation 2050*. 2020.
[8] DNV GL, "Energy Transition Outlook 2020 - A global and regional forecast to 2050," *Dnv Gl Energy Transit. Outlook*, p. 306, 2020, [Online]. Available: https://eto.dnvgl.com/2020/index.html.
[9] Bloomberg NFE, "New Energy Outlook 2018," no. October, 2018, [Online]. Available: https://bnef.turtl.co/story/neo2018?teaser=true.
[10] Ministerie van EZK, "Visie verduurzaming basisindustrie 2050," vol. 2, p., 2020, [Online]. Available: www.rijksoverheid.nl/ezk.
[11] N. Hoogervorst and PBL, "Kosten van klimaatneutrale elektriciteit in 2030 (PBL)," 2020.
[12] S. van Polen and PBL, "Ontwikkelingen in de Energierekening tot en met 2030. Achtergrondrapport bij de Klimaat- en Energieverkenning 2020 (PBL)," p. 27, 2020.
[13] W. Zappa, M. Junginger, and M. van den Broek, "Can liberalised electricity markets support decarbonised portfolios in line with the Paris Agreement? A case study of Central Western Europe," *Energy Policy*, vol. 149, no. September, p. 111987, 2021, doi: 10.1016/j.enpol.2020.111987.
[14] ENTSO-E, "Transmission Day-ahead Prices," 2020. www.entsoe.eu.
[15] TenneT, "Annual Market Update: Electricity markets insights," 2021.
[16] EU, "Energy prices and costs in Europe (European Comission)," 2020.
[17] Ember-Climate, "Daily EU-ETS carbon market price (euros)," 2020. www.ember-climate.org.
[18] Technip Energies, "Technip Energies Internal Communication," 2020.
[19] N. Muller and PwC, "Energy transition , carbon pricing & NL taxation," 2021.
[20] P. Mullinger and B. Jenkins, *Industrial and Process Furnaces: Principles, Design and Operation Chapter*. Elsevier, 2008.
[21] Wikipedia, "Aardgas." https://nl.wikipedia.org/wiki/Aardgas (accessed Jun. 09, 2021).
[22] C. Lowe, N. Brancaccio, D. Batten, C. Leung, and D. Waibel, "Technology assessment of hydrogen firing of process heaters," in *Energy Procedia*, Jan. 2011, vol. 4, pp. 1058–1065, doi: 10.1016/j.egypro.2011.01.155.
[23] T. Weydahl, J. Jamaluddin, M. Seljeskog, and R. Anantharaman, "Pursuing the pre-combustion CCS route in oil refineries - The impact on fired heaters," *Appl. Energy*, vol. 102, pp. 833–839, Feb. 2013, doi: 10.1016/j.apenergy.2012.08.044.

[24] M. Ditaranto, R. Anantharaman, and T. Weydahl, "Performance and NOx emissions of refinery fired heaters retrofitted to hydrogen combustion," in *Energy Procedia*, Jan. 2013, vol. 37, pp. 7214–7220, doi: 10.1016/j.egypro.2013.06.659.

[25] L. Wu, N. Kobayashi, Z. Li, H. Huang, and J. Li, "Emission and heat transfer characteristics of methane-hydrogen hybrid fuel laminar diffusion flame," *Int. J. Hydrogen Energy*, vol. 40, no. 30, pp. 9579–9589, Aug. 2015, doi: 10.1016/j.ijhydene.2015.05.096.

[26] M. Ayoub, C. Rottier, S. Carpentier, C. Villermaux, A. M. Boukhalfa, and D. Honoré, "An experimental study of mild flameless combustion of methane/hydrogen mixtures," *Int. J. Hydrogen Energy*, vol. 37, no. 8, pp. 6912–6921, Apr. 2012, doi: 10.1016/j.ijhydene.2012.01.018.

[27] C. E. Baukal, *Industrial burners handbook - Industrial combustion*. 2003.

[28] K. Vinayagam, "Minimizing flame impingements in fired heaters," *Chem. Eng.*, vol. 114, no. 5, pp. 70–73, May 2007.

[29] Wikipedia, "Global warming potential." https://en.wikipedia.org/wiki/Global_warming_potential (accessed Jun. 10, 2021).

[30] "Greenhouse gas - Energy Education." https://energyeducation.ca/encyclopedia/Greenhouse_gas (accessed Jun. 10, 2021).

[31] C. T. Bowman, "Control of combustion-generated nitrogen oxide emissions: Technology driven by regulation," *Symp. Combust.*, vol. 24, no. 1, pp. 859–878, Jan. 1992, doi: 10.1016/S0082-0784(06)80104-9.

[32] EU, "DIRECTIVE (EU) 2016/ 2284 OF THE EUROPEAN PARLIAMENT AND OF THE COUNCIL - on the reduction of national emissions of certain atmospheric pollutants, amending Directive 2003/ 35/ EC and repealing Directive 2001/ 81/ EC," 2016.

[33] Planbureau voor de Leefomgeving, "NOx-emissie (2020) - Balans van de Leefomgeving | PBL," 2018. https://themasites.pbl.nl/balans-leefomgeving/indicatoren/nl0013-nox-emissie-2020/ (accessed Jun. 14, 2021).

[34] Planbureau voor de Leefomgeving, "NOx-emissie (2030) - Balans van de Leefomgeving | PBL," 2018. https://themasites.pbl.nl/balans-leefomgeving/indicatoren/nl0127-nox-emissie-2030/ (accessed Jun. 14, 2021).

[35] M. Hasanuzzaman, N. A. Rahim, M. Hosenuzzaman, R. Saidur, I. M. Mahbubul, and M. M. Rashid, "Energy savings in the combustion based process heating in industrial sector," *Renewable and Sustainable Energy Reviews*, vol. 16, no. 7. Pergamon, pp. 4527–4536, Sep. 01, 2012, doi: 10.1016/j.rser.2012.05.027.

[36] R. Weber, A. K. Gupta, and S. Mochida, "High temperature air combustion (HiTAC): How it all started for applications in industrial furnaces and future prospects," *Appl. Energy*, vol. 278, no. May, p. 115551, 2020, doi: 10.1016/j.apenergy.2020.115551.

[37] R. Weber, J. P. Smart, and W. Vd Kamp, "On the (MILD) combustion of gaseous, liquid, and solid fuels in high temperature preheated air," *Proc. Combust. Inst.*, vol. 30 II, no. 2, pp. 2623–2629, Jan. 2005, doi: 10.1016/j.proci.2004.08.101.

[38] S. Lupi, *Fundamentals of Electroheat*. 2017.

[39] T. Hegbom, *Integrating Electrical Heating Elements in Product Design*. Taylor & Francis Inc, 1997.

[40] Indeeco, "Process Air Heater." [Online]. Available: https://www.abco.dk/air-heater.htm.

[41] Indeeco, "10 Tips for Selecting Open-Coil, Tubular or Finned-Tubular Elements." https://www.process-heating.com/articles/85968-10-tips-for-selecting-open-coil-tubular-or-finned-tubular-elements (accessed Jan. 07, 2021).

[42] S. W. Churchill and M. Bernstein, "A correlating equation for forced convection from gases and liquids to a circular cylinder in crossflow," *J. Heat Transfer*, vol. 99, no. 2, pp. 300–306, 1977, doi: 10.1115/1.3450685.
[43] B. H. Chang and A. F. Mills, "Effect of aspect ratio on forced convection heat transfer from cylinders," *Int. J. Heat Mass Transf.*, vol. 47, no. 6–7, pp. 1289–1296, Mar. 2004, doi: 10.1016/j.ijheatmasstransfer.2003.09.013.
[44] A. Žukauskas, "Heat Transfer from Tubes in Crossflow," *Adv. Heat Transf.*, vol. 8, no. C, pp. 93–160, Jan. 1972, doi: 10.1016/S0065-2717(08)70038-8.
[45] R. C. Xin and M. A. Ebadian, "Natural convection heat transfer from helicoidal pipes," *J. Thermophys. Heat Transf.*, vol. 10, no. 2, pp. 297–302, 1996, doi: 10.2514/3.787.
[46] M. E. Ali, "Laminar natural convection from constant heat flux helical coiled tubes," *Int. J. Heat Mass Transf.*, vol. 41, no. 14, pp. 2175–2182, 1998, doi: 10.1016/S0017-9310(97)00322-0.
[47] D. G. Prabhanjan, T. J. Rennie, and G. S. V. Raghavan, "Natural convection heat transfer from helical coiled tubes," *Int. J. Therm. Sci.*, vol. 43, no. 4, pp. 359–365, 2004, doi: 10.1016/j.ijthermalsci.2003.08.005.
[48] A. M. Bassily and G. M. Colver, "Modelling and performance analysis of an electric heater," *Int. J. Energy Res.*, vol. 28, no. 14, pp. 1269–1291, 2004, doi: 10.1002/er.1029.
[49] G. Comini, S. Savino, E. Bari, and A. Bison, "Forced convection heat transfer from banks of helical coiled resistance wires," *Int. J. Therm. Sci.*, vol. 47, no. 4, pp. 442–449, 2008, doi: 10.1016/j.ijthermalsci.2007.03.009.
[50] M. Moawed, "Experimental study of forced convection from helical coiled tubes with different parameters," *Energy Convers. Manag.*, vol. 52, no. 2, pp. 1150–1156, 2011, doi: 10.1016/j.enconman.2010.09.009.
[51] J. Wen, Y. Fu, X. Bao, Y. Liu, and G. Xu, "Flow resistance and convective heat transfer performances of airflow through helical-tube bundles," *Int. J. Heat Mass Transf.*, vol. 130, pp. 778–786, 2019, doi: 10.1016/j.ijheatmasstransfer.2018.10.129.
[52] Technip Energies, "Large Scale Vortex Burner Brochure," 2019.
[53] A. F. Mills and C. F. M. Coimbra, *Basic Heat and Mass Transfer*, Third Edit. Temporal Publishing, LLC - San Diego, CA 92130, 2015.
[54] R. Hilpert, "Heat transfer from cylinders," *Forsch. Geb. Ingenieuwwes*, 1933.
[55] V. Gnielinski, "Berechnung mittlerer Wärme- und Stoffübergangskoeffizienten an laminar und turbulent überströmten Einzelkörpern mit Hilfe einer einheitlichen Gleichung," *Forsch. im Ingenieurwes.*, vol. 41, no. 5, pp. 145–153, Sep. 1975, doi: 10.1007/BF02560793.
[56] M. S. Mon and U. Gross, "Numerical study of fin-spacing effects in annular-finned tube heat exchangers," *Int. J. Heat Mass Transf.*, vol. 47, no. 8–9, pp. 1953–1964, Apr. 2004, doi: 10.1016/j.ijheatmasstransfer.2003.09.034.
[57] VDI, "VDI Heat Atlas," 2010.
[58] HTFS, "HTFS Handbook," 1985.
[59] V. Gnielinski, "EQUATIONS FOR CALCULATING HEAT TRANSFER IN SINGLE TUBE ROWS AND BANKS OF TUBES IN TRANSVERSE FLOW.," *Int Chem Eng*, vol. 19, no. 3, pp. 380–391, 1979.
[60] VDI, *VDI Heat Atlas G7*. 2010.
[61] HTFS, "HTFS Handbook SM4," 1985.
[62] B. Şahin, A. Akkoca, N. A. Öztürk, and H. Akilli, "Investigations of flow characteristics in a plate fin and tube heat exchanger model composed of single cylinder," *Int. J. Heat Fluid Flow*, vol. 27, no. 3, pp. 522–530, Jun. 2006, doi: 10.1016/j.ijheatfluidflow.2005.11.005.

[63] G. Ceriello, G. Sorrentino, A. Cavaliere, M. de Joannon, and R. Ragucci, "Mini-Review: Heat Transfer Mechanisms in MILD Combustion Systems," *Front. Mech. Eng.*, vol. 7, no. May, pp. 1–8, 2021, doi: 10.3389/fmech.2021.505923.
[64] J. A. Wünning and J. G. Wünning, "Flameless oxidation to reduce thermal no-formation," *Prog. Energy Combust. Sci.*, vol. 23, no. 1, pp. 81–94, Jan. 1997, doi: 10.1016/s0360-1285(97)00006-3.
[65] G. G. Szegö, "Experimental and Numerical Investigation of a Parallel Jet MILD Combustion Burner System in a Laboratory-scale Furnace," 2010.
[66] Y. A. Zeldovich, "Oxidation of Nitrogen in Combustion," 1947.
[67] C. P. Fenimore, "Formation of nitric oxide in premixed hydrocarbon flames," *Symp. Combust.*, vol. 13, no. 1, pp. 373–380, 1971, doi: 10.1016/S0082-0784(71)80040-1.
[68] A. Frassoldati, E. Ranzi, C. Dipartimento, and I. Chimica, "Internal presentation on 'Kinetic and fluid dynamic modeling of NOx formation and reduction,'" 2004.
[69] A. H. Lefebvre and D. R. Ballal, *Gas Turbine Combustion: Alternative Fuels and Emissions*, Thrid Edit. 2010.
[70] D. Dewanji, A. G. Rao, M. Pourquie, and J. P. van Buijtenen, "Investigation of Flow Characteristics in Lean Direct Injection Combustors," *J. Propuls. Power*, vol. 28, no. 1, pp. 181–196, Jan. 2012, doi: 10.2514/1.B34264.
[71] J. B. Heywood, "Pollutant formation and control in spark-ignition engines," *Prog. Energy Combust. Sci.*, vol. 1, no. 4, pp. 135–164, Jan. 1976, doi: 10.1016/0360-1285(76)90012-5.
[72] G. J. Nathan, R. E. (Sam) Luxton, and J. P. Smart, "Reduced NOx emissions and enhanced large scale turbulence from a precessing jet burner," *Symp. Combust.*, vol. 24, no. 1, pp. 1399–1405, Jan. 1992, doi: 10.1016/S0082-0784(06)80163-3.
[73] J. J. Parham, G. J. Nathan, J. P. Smart, S. J. Hill, and B. G. Jenkins, "Relationship between heat flux and NOx emissions in gas-fired rotary kilns," *J. Inst. Energy*, vol. 73, no. 494, pp. 25–34, 2000.
[74] C. E. Baukal, *The john zink hamworthy combustion handbook, second edition: Volume 1 - fundamentals*. 2012.
[75] API, "Burners for Fired Heaters in General Refinery Services," 2014.
[76] L. Bebar, V. Kermes, P. Stehlik, J. Canek, and J. Oral, "Low NOx burners - Prediction of emissions concentration based on design, measurements and modelling," *Waste Manag.*, vol. 22, no. 4, pp. 443–451, Jul. 2002, doi: 10.1016/S0956-053X(02)00028-4.
[77] T. Hasegawa, S. Mochida, and A. K. Gupta, "Development of advanced industrial furnace using highly preheated combustion air," *J. Propuls. Power*, vol. 18, no. 2, pp. 233–239, 2002, doi: 10.2514/2.5943.
[78] L. Wu, N. Kobayashi, Z. Li, and H. Huang, "Experimental study on the effects of hydrogen addition on the emission and heat transfer characteristics of laminar methane diffusion flames with oxygen-enriched air," *Int. J. Hydrogen Energy*, vol. 41, no. 3, pp. 2023–2036, Jan. 2016, doi: 10.1016/j.ijhydene.2015.10.132.
[79] A. Frassoldati *et al.*, "Experimental and modelling study of low-NOx industrial burners," *MPT Metall. Plant Technol. Int.*, vol. 31, no. 6, pp. 44–46, 2008.
[80] M. Katsuki and T. Hasegawa, "The science and technology of combustion in highly preheated air," in *Symposium (International) on Combustion*, Jan. 1998, vol. 27, no. 2, pp. 3135–3146, doi: 10.1016/S0082-0784(98)80176-8.
[81] R. G. Kunz, D. D. Smith, and E. M. Adamo, "Predicting NOx from gas-fired furnaces," *Hydrocarb. Process.*, vol. 75, no. 11, 1996.

[82] T. Faravelli, L. Bua, A. Frassoldati, A. Antifora, L. Tognotti, and E. Ranzi, “A new procedure for predicting NOx emissions from furnaces,” *Comput. Aided Chem. Eng.*, vol. 8, no. C, pp. 859–864, 2000, doi: 10.1016/S1570-7946(00)80145-5.
[83] H. K. Versteeg and W. Malalasekera, *An Introduction to Computational Fluid Dynamics: The Finite Volume Method*. 1995.
[84] M. G. Corporation, “Technical Reference Software FloEFD,” 2014.
[85] Watlow, “Tubular Heaters.”
[86] Watlow, “Watlow heating elements catalog.”
[87] Vulcanic, “STANDARD PRODUCTS ELECTRICAL HEATING AND COOLING SOLUTIONS: All in One Solutions.”
[88] “Lang Factor Cost Estimating.” http://prjmgrcap.com/langfactorestimating.html (accessed May 31, 2021).
[89] M. F. van Amsterdam, “Factorial Techniques applied in Chemical Plant Cost Estimation : A Comparative Study based on Literature and Cases,” *Chem. Eng.*, p. 158, 2018.
[90] “REFPROP | NIST.” https://www.nist.gov/srd/refprop (accessed May 26, 2021).
[91] A. Approach, C. Section, and F. Heaters, “J. van Dijk.”